1996

Computational characterization of prospective n- and p-type dopants in cubic boron nitride.

David Clay Patton

University of Alabama at Birmingham

Recommended Citation

Patton, David Clay, "Computational characterization of prospective n- and p-type dopants in cubic boron nitride." (1996). *All ETDs from UAB*. 5951.
https://digitalcommons.library.uab.edu/etd-collection/5951

INFORMATION TO USERS

This manuscript has been reproduced from the microfilm master. UMI films the text directly from the original or copy submitted. Thus, some thesis and dissertation copies are in typewriter face, while others may be from any type of computer printer.

The quality of this reproduction is dependent upon the quality of the copy submitted. Broken or indistinct print, colored or poor quality illustrations and photographs, print bleedthrough, substandard margins, and improper alignment can adversely affect reproduction.

In the unlikely event that the author did not send UMI a complete manuscript and there are missing pages, these will be noted. Also, if unauthorized copyright material had to be removed, a note will indicate the deletion.

Oversize materials (e.g., maps, drawings, charts) are reproduced by sectioning the original, beginning at the upper left-hand corner and continuing from left to right in equal sections with small overlaps. Each original is also photographed in one exposure and is included in reduced form at the back of the book.

Photographs included in the original manuscript have been reproduced xerographically in this copy. Higher quality 6" x 9" black and white photographic prints are available for any photographs or illustrations appearing in this copy for an additional charge. Contact UMI directly to order.

UMI

A Bell & Howell Information Company
300 North Zeeb Road, Ann Arbor MI 48106-1346 USA
313/761-4700 800/521-0600

Reproduced with permission of the copyright owner. Further reproduction prohibited without permission.

COMPUTATIONAL CHARACTERIZATION OF PROSPECTIVE N- AND P-TYPE DOPANTS IN CUBIC BORON NITRIDE

by

DAVID CLAY PATTON

A DISSERTATION

Submitted in partial fulfillment of the requirements for the degree of
Doctor of Philosophy in the Department of Physics in
the Graduate School, The University of
Alabama at Birmingham

BIRMINGHAM, ALABAMA

1996

UMI Number: 9700025

UMI Microform 9700025

UMI
300 North Zeeb Road
Ann Arbor, MI 48103

ABSTRACT OF DISSERTATION
GRADUATE SCHOOL, UNIVERSITY OF ALABAMA AT BIRMINGHAM

Degree Doctor of Philosophy Major Subject Physics

Name of Candidate David Clay Patton

Title Computational Characterization of Prospective n- and p-type Dopants in Cubic Boron Nitride

Wide band-gap semiconductors are of interest to materials scientists because of their potential electronic applications. One promising material is cubic boron nitride, the second hardest material known. Experimentally, cubic boron nitride has been doped to both *n*- and *p*-type conductivity. Introducing beryllium into cubic boron nitride has generated material that exhibits *p*-type behavior. Silicon has produced both *p*-type and *n*-type material when incorporated into cubic boron nitride. In this work, we have studied the electronic structure of beryllium and silicon substitutional for boron in cubic boron nitride. We have employed a density functional theory based linear combination of atomic orbitals (LCAO) cluster method to explore the electronic structure. A general method of embedding clusters with the LCAO code is developed and implemented. One of the important features of this embedding approach is that it allows for lattice relaxations within the cluster. In order to reproduce the bonding environment of the crystal, atoms in the cluster must be assigned the proper number of electrons necessary to produce the required sp^3 hybrid orbitals. It was found that this electron filling requirement and embedding were not complementary. Therefore, embedding was shown to be of less importance in cubic boron nitride. Utilizing the

LCAO cluster codes, the beryllium was found to produce an acceptor level 0.236 eV above the next highest occupied level. Silicon was found to produce a donor level 0.116 eV below the lowest unoccupied level. Both beryllium and silicon induced the clusters nearest neighbor nitrogen shells to relax outward from the bulk geometry. A large part of the objective of this study was to calculate properties of these substitutional defects in cubic boron nitride that could be measured experimentally. Thus, calculations of vibrational spectra, Fermi contact terms, oscillator strengths, and vibrational spectra are presented for the pure cubic boron nitride clusters and the defect clusters.

Abstract Approved by: **Committee Chairman** __________

Program Director __________

Date 7/1/96 **Dean of Graduate School** __________

DEDICATION

To my family, particularly my parents, for providing me with an invigorating environment of learning during my childhood and for supporting my educational goals, and to Holly for her love, support, and optimistic spirit.

ACKNOWLEDGEMENTS

I would like to thank my advisor, Dr. Joseph G. Harrison, for his continuous guidance, advice, and encouragement throughout my graduate research and preparation of this work. I greatly appreciate his "open door" policy that he exhibits with all of his students and that during my visits to his office I was always rewarded with his great chemical insight into physical problems. I also wish to express my gratitude to Drs. Ryoichi Kawai, Yogesh K. Vohra, and M.E. Zvanut of the UAB physics department for serving on my committee. I was fortunate enough to have enrolled in some of the more specialized classes on solid state physics that they offered. My research has undoubtedly been greatly improved from the knowledge gained in such courses. Dr. Ian W. Knowles of the UAB mathematics department and Dr. Tracy Hamilton of the UAB chemistry department have served on my committee, for which I am grateful. I was priviledged to have audited Dr. Hamilton's quantum chemistry course during my graduate studies.

I would like to acknowledge support from the U.S. Department of Education's GAANN program and the U.S. Department of Energy Alabama EPSCoR Traineeship program. It was within the EPSCoR Traineeship that the idea of studying a very applied problem was first formulated. In addition, the EPSCoR Traineeship allowed me to spend three summers working at Oak Ridge National Laboratory in the Theory group of the Materials Science section of the Metals and Ceramics Division. I was fortunate to be able to work closely with Dr. Gayle S. Painter of ORNL and Dr. Frank W. Averill of Judson College. I am thankful for their advice on this work during my time at ORNL and for allowing me access to their workstations. I am especially thankful to Dr. Painter for serving on my committee.

I wish to thank Dr. Mark R. Pederson of the Naval Research Laboratory for providing us with a copy of his LCAO cluster codes, which we have modified to fit our needs. I am also indebted to Dr. Pederson for his ideas about parallelization of the code.

I would like to acknowledge a generous grant from the Alabama Supercomputer Center that allowed us to perform this study in a timely manner. Through the use of the Maui High Performance Computing Center, this research was sponsored in part by the Phillips Laboratory, Air Force Materiel Command, USAF, under cooperative agreement number F29601-93-2-0001. The views and conclusions contained in this document are those of the author and should not be interpreted as necessarily representing the official policies or endorsements, either expressed or implied, of Phillips Laboratory, the U.S. Government, The University of New Mexico, or the Maui High Performance Computing Center.

TABLE OF CONTENTS

CHAPTER

TABLE OF CONTENTS (Continued)

Page

CHAPTER

APPENDIX

LIST OF TABLES

LIST OF TABLES (Continued)

LIST OF FIGURES

LIST OF FIGURES (Continued)

LIST OF FIGURES (Continued)

LIST OF FIGURES (Continued)

CHAPTER I

INTRODUCTION

In the last few years, significant progress has been achieved in the crystal growth of wide energy band-gap semiconductors (E_g>2.3 eV). This has resulted in an increased interest in using these materials for electronic and optoelectronic devices. Based on the physical properties of these materials, the fabrication of novel devices with operating characteristics greatly superior to those made from either silicon or gallium arsenide should be possible. Potential applications envisioned include electronic devices capable of operation at elevated temperatures (>600° C), high power, high frequency, and short wavelength optoelectronic devices such as solar blind ultraviolet light detectors, blue light emitting diodes, or ultraviolet laser diodes.

Devices with high quality operating characteristics require not only the necessary physical properties, but the means to produce them as well. In addition to crystal growth, methods of selective doping, metal contact formation, device isolation, and material etching must be established in order to produce devices. A realistic evaluation of the prospects of a material for device implementation must, therefore, address the available processing technology as well as the physical properties of the semiconductor.

The major semiconducting materials that are currently under development for devices requiring wide energy band-gaps are diamond, silicon carbide, boron nitride, aluminum nitride, and gallium nitride. All of these semiconductors have tetragonal sp^3 chemical bonds. The chemical bonding of these materials is partially ionic, with the notable exception of diamond, which is completely covalent. As a general trend, the energy band-gap increases as the chemical bonding becomes more ionic. This is illustrated in Table I. Associated with the increasing ionic character of these materials is the difficulty in obtaining both p-type and n-type conductivity. Unlike silicon, in which the conductivity type can be converted with the addition of the appropriate impurity (e.g., arsenic to convert p-type silicon to n-type), in general compensation will occur but conversion will not for wide band-gap semiconductors. That is, the charge carrier concentration is reduced but the majority charge carrier polarity does not change. This trend has also been observed in ionic semiconductors with small energy band-gaps such as cadmium telluride.[1] This behavior is not well understood, but is believed to be associated with the formation of point defects. Simultaneous with the introduction of impurities into the material, vacancies, antisite defects, or interstitials may form which compensate the effects of the impurity.[1,2,3] Although we will not be addressing these compensation effects, there has been some work by Gubanov *et al.*[4] in which vacancies were studied as p- and n-type doping agents.

These materials exist as semiconductors in variations of two basic structures: cubic and wurtzite. Two cubic structures are possible, the diamond structure for elemental semiconductors (diamond in this case) and the zincblende structure for compound semiconductors (cubic boron nitride). Gallium nitride and aluminum nitride are most commonly observed in the wurtzite structure, although evidence of cubic structures exists. Silicon carbide exists in several forms containing various amounts of both wurtzite and cubic structures. Carbon and boron nitride commonly occur in cubic, wurtzite, and hexagonal (graphitic) structures. The graphitic structures

TABLE I. Selected physical properties of wide band-gap semiconductors. Values are taken from Edgar.[1]

	Material	Band-gap (eV) at 300 K	Percent ionicity	Band transitions	Commonly observed conductivity types
IV	Diamond	5.45	0%	Indirect	p
	Silicon carbide				
	β-(3C)	2.3	12%	Indirect	n,p
	α-(6H)	2.9	12%	Indirect	n,p
III-V	β-boron nitride	6.4	26%	Indirect	n,p
	Gallium nitride	3.4	35%	Direct	n
	Aluminum nitride	6.3	47%	Direct	n

contain sp^2 bonds that make them useful for their mechanical properties, but neither (in its hexagonal form) is under consideration for electronic devices. BN is also known to exist in rhombohedral,[5] simple cubic,[6] and turbostratic[7] phases. Fig. 1, Fig. 2, Fig. 3, and Fig. 4 show the diamond, zincblende, wurtzite, and graphite structures, respectively.

The properties of cubic boron nitride are similar to those of carbon,[8] and the success of diamond CVD has renewed interest in cubic boron nitride as well. Cubic boron nitride has the largest energy band-gap of all the semiconductors mentioned above, approximately 6.4 eV.[26] The ionicity of cubic boron nitride has been reported in the range of 26% to 38%.[1,9] With this large ionicity, crystal field effects may play an important part in determining the size of the energy band-gap and the location of dopant levels relative to the band edges, and must be investigated in calculations.

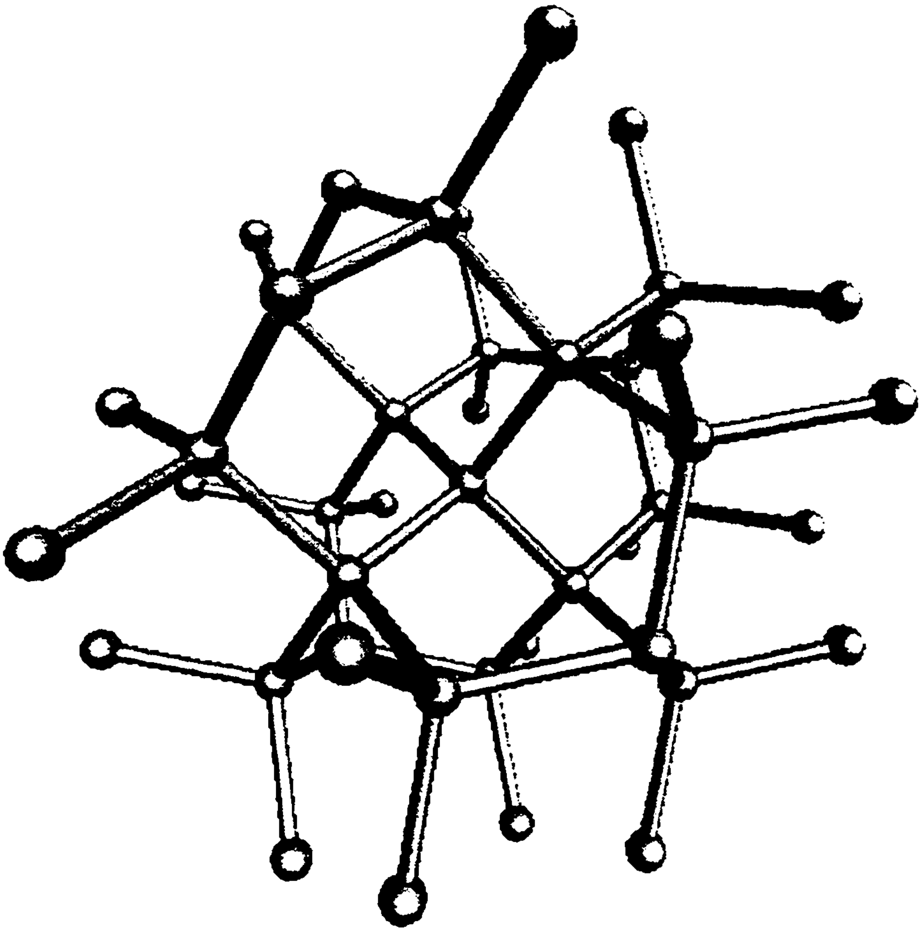

FIG. 1. A cluster of carbon atoms in the diamond structure. Note the tetrahedral bonding at each of the interior atom sites.

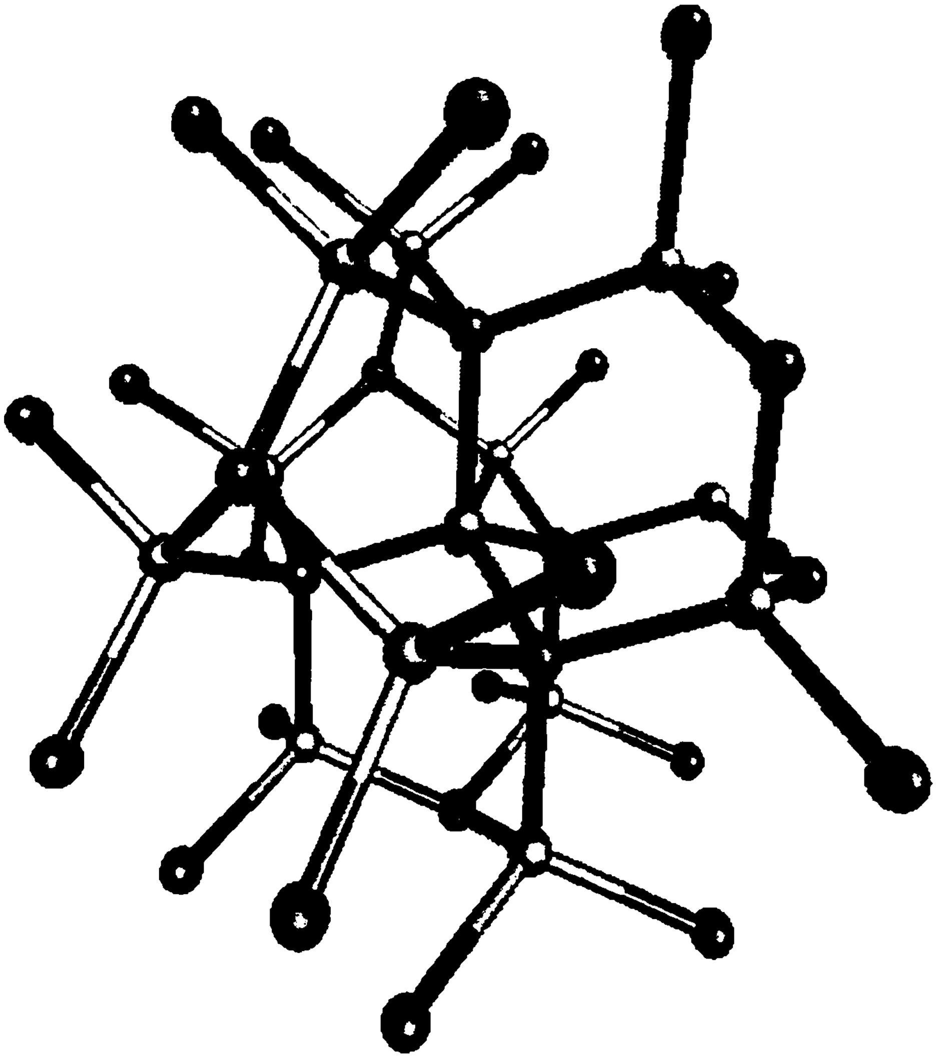

FIG. 2. A cluster of boron nitride in the zincblende structure. The cluster is centered on a boron site (lighter color) that clearly shows the tetrahedral bonding.

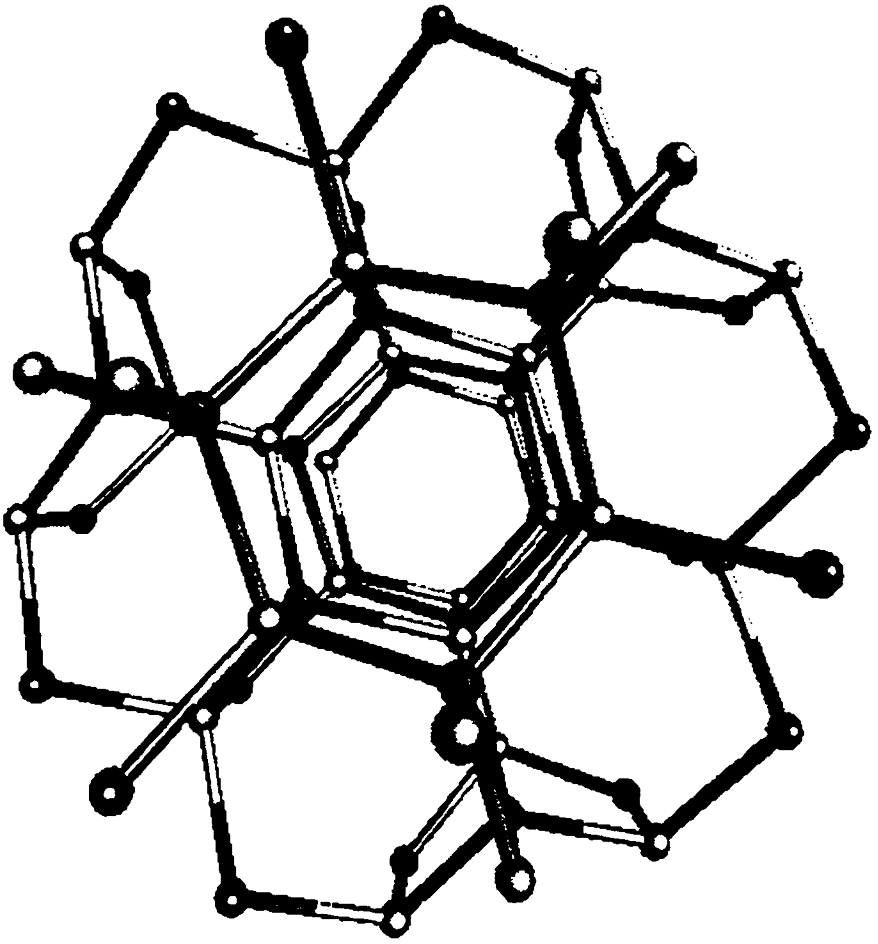

FIG. 3. A cluster of boron nitride in the wurtzite structure. Again the bonding is tetrahedral.

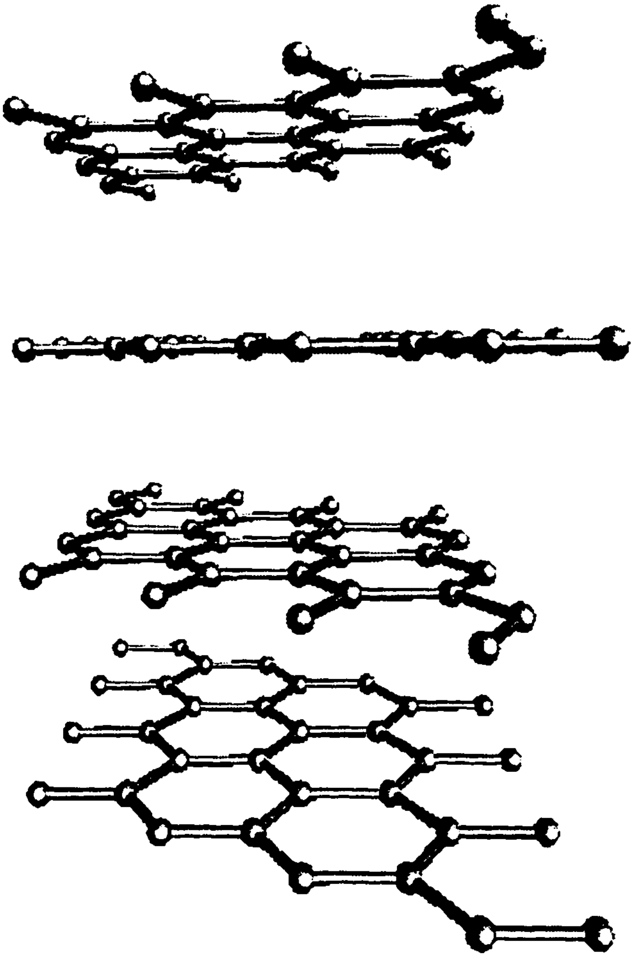

FIG. 4. The graphite crystal structure. Trigonal bonding is evident.

Other properties of cubic boron nitride such as hardness, chemical resistance, and thermal conductivity are similar to that of diamond.

The principal advantages of cubic boron nitride are its very large energy bandgap and its ability to be doped to produce both *n*- and *p*-type conductivity. One major disadvantage of cubic boron nitride is the extreme conditions required to produce it. A large variety of experimental techniques have been used to synthesize cubic boron nitride, predominantly as thin films: chemical[10] and physical vapor deposition[11,12,13] (CVD and PVD, respectively), plasma enhanced CVD,[14,15,16] pulsed excimer laser ablation,[17] radio-frequency sputtering,[18] ion-assisted laser deposition,[19,20] neutralized nitrogen ion bombardment,[21] Ar ion-beam-enhanced deposition,[22] and others. The progress which has been made in the low pressure deposition of diamond offers some hope that cubic boron nitride can be produced by a similar technique. While the results of thin film deposition remain promising, the only clearly successful method for producing cubic boron nitride for semiconductor devices is the high pressure, temperature difference method developed by Mishima *et al.*[23] Cubic boron nitride can be made *n*-type with the addition of silicon, sulfur, KCN, melamine, 2-methyl pyrazine, and carbon; or *p*-type with the addition of beryllium.[24,25] The ionization energy for these impurities is low enough that activation occurs near room temperature. Diodes have been fabricated which are rectifying up to 650° C, and which emit a broad spectrum of ultraviolet and visible light.[23]

The advantages of one semiconductor over another cannot be readily evaluated from functioning devices when the device fabrication technology for each is at different levels of development. Therefore, it is very important that the properties of these materials be thoroughly investigated theoretically and that calculations give some insight into the interpretation of available experimental measurements. With this as our objective, we have carried out a computational characterization of prospective *n*- and *p*-type dopants in cubic boron nitride.

From a theoretical standpoint, cubic boron nitride is a very complex material to study. Although it is very similar to diamond, it has one substantial difference, that cubic boron nitride is a partially ionic material. Cubic boron nitride is a typical III-V binary compound with strong covalent bonds, leading to its similarity to diamond. However, there is a significant charge surplus at the nitrogen sites and a charge deficiency associated with the boron sites producing some ionic bonding that makes cubic boron nitride an intriguing wide band-gap material. As a consequence of ionic charges, long range Coulomb forces come into play. The covalency and ionic effects of cubic boron nitride play important roles when substitutional defects are introduced into cubic boron nitride as dopants. Unlike silicon, where dopant energy levels reside much less than half an eV into the band-gap, suitable dopants in cubic boron nitride may be deeper in the gap. Because of the high temperature operating range of these materials, activation energies greater than those in silicon are allowed and have been seen for silicon and beryllium doped material.[23] Hence the dopants may share similarities with defects in ionic insulators as well as dopants in standard semiconducting materials.

In this work, we use various first-principles, *ab-initio*, and semi-empirical methods to characterize prototypical dopants in cubic boron nitride. The dopants are each modelled as a substitutional defect at the center of a large cluster of cubic boron nitride. Beryllium is chosen as an acceptor. Silicon is studied as a donor. Crystal field effects are studied with a new embedding procedure. Since limited work has been performed on pure cubic boron nitride and almost no previous studies by other authors have been undertaken to characterize the substitutional defects studied in this work, we have chosen to concentrate our efforts in three common areas of measurement. The three areas are the electronic structure, vibrational modes, and optical spectra. The electronic structure including defect-induced lattice relaxations is calculated within the local spin density approximation of density functional theory via a linear combinations of atomic orbitals method. Vibrational characterization of the defects is performed with the use of the semi-empirical MOPAC6 package. Optical characterization is done by using the output from the GAMESS code to perform calculations of the photoemission spectra, and oscillator strengths are investigated with the ICON-EDiT package.

The formulae and capabilities of each of the above methods is explained in Chapter II. In addition, Chapter II contains a discussion of the suitability of using cluster methods to study defects in solids. Chapter III is devoted to the effect of the crystal field on cluster calculations. Various methods of calculating the crystal field are proposed, and then their effectiveness for cubic boron nitride clusters is evaluated with regard to accuracy and computational efficiency. In Chapter IV, the calculated electronic structure of proto-typical dopants in cubic boron nitride is discussed. Additional aspects such as vibrational and optical spectra are examined in Chapter V. Finally, Chapter VI contains concluding remarks. Unless otherwise noted, atomic units (in which $e^2 = h/2\pi = m = 1$) are used throughout this work.

CHAPTER II

ELECTRONIC STRUCTURE METHODS

In this work, we use various first-principles, *ab-initio*, and semi-empirical methods to characterize prototypical dopants in cubic boron nitride. Each dopant is modelled as a substitutional defect at the center of a large cluster of cubic boron nitride. The electronic structure including defect-induced lattice relaxations is calculated with a linear combination of atomic orbitals method. Part of the optical characterization is performed with the *ab-initio* GAMESS code and vibrational characterization of the defects is performed with the use of the semi-empirical MOPAC6 package. A discussion of the use of clusters to model solids and descriptions of each of the above mentioned electronic structure codes follows.

A. Modeling of defects by cluster methods

The use of cluster methods for solid state studies can be traced back to the work of Hans Bethe on the crystal field splitting of the energy levels of impurity ions in insulators.[26] More recently, it has been realized that the applicability of such an approach is far broader. Cluster calculations are being applied to a remarkable diversity of physical problems. These include the hyperfine properties of insulators and semiconductors, point defects in solids, reaction energetics and adsorbate structure on surfaces, cluster assembled materials, magnetic properties of solids, etc.[27] These different studies can usually be categorized as belonging to one of two types, involving either (i) rather small clusters with the embedding medium treated approximately, or (ii) larger clusters of increasing size extrapolated to approximate the infinite crystal. Where crystal field effects are not prominent, the first type of study may be utilized without any embedding medium. In the present study of dopants in cubic boron nitride, the first type of cluster method is used extensively. Clusters with and without embedding fields are considered. The second type of cluster method is used briefly to analyze the convergence of the energy band-gap in cubic boron nitride.

The cluster approach has a straightforward intuitive appeal in investigating localized defects in solids, in that the preponderance of computational effort is spent only on the region of interest and not on the essentially unperturbed regions of the host crystal. From a practical point of view, the cluster method allows for the investigation of structural properties associated with the defect and the importance of geometrical relaxation in determining the electronic properties associated with the defect. In addition, the method provides a direct and systematic means for determining the convergence of calculated properties with respect to cluster size.

When a cluster is used to model a crystal, the surface of the cluster has electronic states associated with it that may perturb the electronic structure in the interior of the cluster. This makes analysis of substitutional defects at the cluster center very difficult and questionable. The primary cause of this perturbation of the cluster's electronic structure is that bonds at the cluster's surface have been broken. These dangling-bond states tend to penetrate into the cluster, and in many systems the electronic levels associated with these dangling bonds fall into the band-gap of the cluster. When studying dopants in wide band-gap semiconductors, it is very important not to have dangling bond states falling into the band-gap and interacting with the defect levels in the band-gap. The dangling-bonds are of much more concern when studying partially covalent materials as opposed to ionic materials where dangling bonds can be dealt with effectively by embedding methods.

To correct the problem of dangling bonds at the surface of a cluster, two tasks must be accomplished. First, the states associated with the bonds at the surface should be localized to the surface and not penetrate significantly into the cluster interior. Second, the energy levels of the dangling-bond states should be well away from the band-gap of the cluster, so that there will be no interaction with dopant defect levels in the band-gap. One of the most successful methods for accomplishing both of the tasks described above is the saturation of the dangling bonds with hydrogen atoms. The importance of the "tying off" of the dangling bonds with hydrogen atoms has been discussed previously by Tomanek and Schluter.[28] They made it clear that the surface bonds must be properly treated because small clusters of atoms, without terminating hydrogen atoms, do not condense in the structure of the bulk material. Hydrogen-saturated clusters have been used extensively before to explore electronic and structural properties of solids.[29,30,31,32,33,34,35] Because saturation of dangling bonds with hydrogen atoms has been applied to defects in diamond[36] and III-V semiconductors[37] with good results, we have chosen to utilize this method in our study.

In modeling III-V compounds such as cubic boron nitride with clusters, it is important to achieve the same bonding as is present in the crystalline form. Because cubic boron nitride is isoelectronic with diamond, we want to achieve the same type of sp^3 hybrid orbitals that lead to tetrahedral bonding. In the isolated carbon atom, the electronic configuration of its six electrons is $1s^2 2s^2 2p^2$. Another configuration may be more stable in a bonding environment. From the valence bond theory,[38] the two core electrons in the $1s$ orbital are not involved in bonding. That leaves the bonding up to the four valence electrons in the 2*s* and 2*p* states. This arrangement would lead to the prediction of three nonequivalent bonds involving 2*s* states from one atom overlapping 2*s* states on a neighboring atom, 2*s* states from one atom overlapping its neighbor's 2*p* states, and 2*p* states overlapping neighboring 2*p* states. However, experimentally the bonds are seen to be equivalent in bond length and bond strength. For the atomic 2*s* and 2*p* orbital to become equivalent so as to form a single type of valence bond, they must hybridize to form *sp* hybrid orbitals. In graphite, the electronic environment favors sp^2 hybrid orbitals to be formed by one 2*s* orbital and two 2*p* orbitals. This leads to the trigonal bonding structure seen in graphite. In diamond one of the 2*s* orbitals hybridizes with three 2*p* states. This allows the formation of sp^3 hybrid orbitals. The number of hybrid orbitals is always equal to the number of atomic orbitals hybridized. Thus, the hybridization of one *s* orbital and three *p* orbitalso gives four sp^3 hybrids that bond tetrahedrally. Cubic boron nitride also is bonded tetrahedrally. In order for this to occur, sp^3 bonding must take place. This means that there must be a valence electronic configuration of $2s^2 2p^2$, like diamond. In order to achieve this configuration, boron and nitrogen must be filled with six electrons apiece. So in our clusters of cubic boron nitride, we have assigned six electrons to boron and six electrons to nitrogen. Previously, this type of electron filling has been used successfully in the study of defects in other III-V semiconductors.[37]

B. First-principles LCAO method

In this study, a finite cluster of atoms is embedded in a crystal field to simulate the infinite system. To calculate the ground state density for these systems, a Gaussian-orbital-based, linear combination of atomic orbitals (LCAO) approach is adopted, in which the one electron equations are solved self-consistently in a fixed basis set consisting of contracted Gaussian orbitals obtained from calculations for the relevant free atoms. When needed, additional single Gaussian orbitals centered at the various nuclei may be used to augment the variational freedom of the basis.[39] These basis functions are centered only on the atom sites of the finite cluster. The foundation of this LCAO cluster method is density functional theory and the local density approximation (LDA), which are discussed in Appendix A. A recently developed variational mesh formalism is utilized for the numerical integration of all Hamiltonian matrix elements.[40] This variational mesh approach is optimal for the type of embedding technique described in the next chapter. In order to determine defect-induced lattice relaxations, the forces are calculated as the proper total energy derivatives including the necessary basis-set corrections.[41,42] In order to find the minimum total energy geometry, these forces are then used within the conjugate gradient method.[43]

C. GAMESS

The General Atomic and Molecular Electronic Structure System (GAMESS) is an *ab-initio* package put together from several existing quantum chemistry programs, particularly HONDO. The latest version of GAMESS is maintained by Mike Schmidt of Ames Laboratory at Iowa State University and is described by Schmidt *et al.*[44] GAMESS performs a wide range of quantum chemical computations. One can calculate restricted Hartree-Fock (RHF), unrestricted Hartree-Fock (UHF), restricted open shell Hartree-Fock (ROHF), generalized valence bond (GVB), multi-configurational SCF (MCSCF), and configuration interaction (CI) molecular SCF wavefunctions. The wavefunctions can then be used to calculate energy gradients for geometry optimization, find energy surface saddle points, or trace reaction paths. Additional properties such as normal modes, vibrational frequencies, IR intensities, radiative transition probabilities, dipole moments, spin densities, Mulliken populations, and polarizabilities can also be calculated. We have used GAMESS for vibrational analysis of cubic boron nitride clusters with substitutional defects. GAMESS calculates the vibrational frequencies and IR intensities for each mode. This is accomplished by computing the energy second derivatives (the Hessian matrix) numerically and performing harmonic vibrational analysis.

D. MOPAC6

MOPAC6 is a general-purpose semi-empirical molecular orbital package for the study of chemical structures and reactions. The semi-empirical Hamiltonians[45] MNDO, MINDO/3, AM1 and PM3 are used in the electronic part of the calculation to obtain molecular orbitals, the heat of formation, and its derivative with respect to molecular geometry. Using these results MOPAC6 is capable of performing single (RHF, UHF, and CI) SCF calculations, geometry optimizations, force constant analysis, reaction coordinate calculations, and many other property calculations. We have used MOPAC6 for vibrational analysis of cubic boron nitride clusters with substitutional defects.

CHAPTER III

CRYSTAL FIELD EFFECTS

As discussed in the previous chapter, modelling a crystal with a simple cluster consisting of the constituent atoms of the bulk material does not always result in the same electronic and structural properties as that of the bulk material. Deficiencies of the cluster model must be accounted for in order to achieve the same environment as that found in the bulk. Surface bonds must be saturated with hydrogens and electron filling must produce similar bonding. In ionic systems, one more deficiency of the cluster model must be addressed. The long range crystal field effects from the Madelung potential must be properly treated. An effective method of accounting for crystal field effects is to embed the cluster in some form of embedding potential. Embedding potentials have long been used for simulating the crystalline environment experienced by clusters and even atoms[46] in ionic solids.

In Appendix A, the Kohn-Sham equations are discussed. In Eq. (A.9), the external potential is needed. For a cluster this can be written as

$$V_{ext}(\boldsymbol{r}) = -\sum_{\nu} \frac{Z_{\nu}}{|\boldsymbol{r} - \boldsymbol{R}_{\nu}|} + V_{host}(\boldsymbol{r}) \tag{3.1}$$

where V_{ext} is the sum of the electron-nucleus attraction within the cluster, with Z_{ν} the charge on the νth nucleus, centered at R_{ν} and the electron interaction with the rest of the host crystal represented by the potential V_{host}. This potential, V_{host}, is the embedding potential applied to the cluster and must be calculated at mesh points utilized in the integration of the Hamiltonian matrix. Several methods can be used to calculate this embedding potential. Each will be explained and then analyzed for its computational efficiency and accuracy.

A. The Watson sphere method

One of the first uses of an embedding potential to simulate the environment of a solid was by Watson.[46] He studied the O^{-} ion in oxide crystals. He embedded the ions in stabilizing potential wells of positive charge. To calculate the embedding potential, he placed a shell (the Watson sphere) of uniform positive charge around the O^{-} ion. The radius of the shell was equal to the ionic radius of the O^{-} ion. He chose as his positive charge magnitude +1 and +2. His choice of +1 was based on the following argument: consider the potential energy that one electron sees due to the nuclear charge of +8 and the other nine electrons. At the nucleus the potential energy has gone to $-\infty$, and as the electron moves out radially, the potential energy increases, goes through a maximum, and then drops off slowly due to the net charge of -1 of the rest of the ion. A shell of charge +1 at the maximum would destroy the repulsion for large radii, while leaving the correct potential for the interior. Argument for using a stabilizing well of +2 charge was made because the net charge produced by the remainder of the crystal would be just that. Watson successfully used this method in an analytical Hartree-Fock calculation. The method then became known as the Watson sphere method.

The Watson sphere method has been applied to clusters by placing a large sphere of uniformly distributed surface charge around the cluster. Fazzio *et al.*[47] applied this to the calculation of the electronic structure of IV and III-V covalent semiconductors in which they used an outside sphere radius of 9.74 a.u. Although they restricted themselves to 17-atom clusters, their results encouraged us to attempt to utilize the Watson Sphere method for clusters of cubic boron nitride. However, the Watson sphere method did not prove to be a satisfactory technique for embedding cubic boron nitride clusters. Although it is a computationally efficient method, ambiguities in assigning the charge of the sphere and the radius of the sphere make it difficult to utilize. We chose a charge and radius that reproduced the Madelung constant at the center of the cluster. However, we believe that this does not represent the potential accurately at the cluster edges and that it completely eliminates any nonspherical structure in the potential from the lattice geometry.

B. Direct summation

Another way of accounting for the potential of the host crystal is to replace all the ions in the bulk crystal with point ions of charge +q and -q, with the magnitude of q depending on the particular system being studied. For example, the NaCl crystal is composed of Na^+ and Cl^- ions, so the value of q is 1. Then, the point ions at the positions of atoms in the cluster are removed. This procedure produces an infinite distribution of point ions which results in an embedding potential that accounts for the crystal field effects. The difficult task in this embedding procedure is to calculate this embedding potential in an accurate and rapid manner.

This embedding potential of the point-ions is given by

$$V_{host}(r) = \sum_{\nu=1}^{\infty} \frac{\pm q}{|r-R_\nu|} - \sum_{\nu=1}^{m} \frac{\pm q}{|r-R_\nu|} \quad . \tag{3.2}$$

where m is the number of ions in the cluster and $\mathbf{R}_\nu$ are the lattice points. The first sum in Eq. (3.2) is conditionally convergent. Suppose $\sum_{n=1}^{\infty} a_n$ is also a conditionally convergent series. A conditionally convergent series is one in which the series, $\sum_{n=1}^{\infty} a_n$, converges and the series of absolute values, $\sum_{n=1}^{\infty} |a_n|$, diverges. Conditional convergence can be tested by the alternating series test. To satisfy the alternating series test, the series must 1) be alternating, 2) $|a_{n+1}| \le |a_n|$ for all n, and 3) $\lim_{n \to \infty} a_n = 0$.

Thus, direct summation of the terms in Eq. (3.2) will converge. Unfortunately, it converges very slowly and thus more powerful techniques than direct summation must be used to speed up the convergence of the lattice summation calculation.

C. The Frank method

Series such as the one encountered in the first term of Eq. (3.2) were first encountered in the calculation of the self potential of a crystal lattice. The self potential is the electrostatic potential at the negative atom site for the infinite distribution of point ions at all lattice sites except at the site where the potential is being evaluated. This self potential can be written in terms of a constant that is independent of the ionic charges.[48] The constant is known as the Madelung constant and is unique for each crystal structure. The conditional convergence of the series which expresses the self potentials prevents their evaluation by straightforward lattice summation; however, appropriate rearrangements of the terms of the series allows the calculation of the Madelung constant for special crystal structures by truncated direct summation. Madelung[49] calculated the Madelung constant for NaCl by transforming the electrostatic potential of a neutralized, linear, or planar Bravais lattice of unit point charges, at a point outside of the lattice, into a rapidly converging series over the reciprocal lattice. His method is accurate but is limited by its complexity and computational inefficiency. Thus, it is not suitable to embedded cluster calculations. It is thought[50] to be of use for the evaluation of the lattice sums encountered in surface problems.

Evjen[51] devised a way of cleverly rearranging terms in the series to transform the conditionally convergent self potentials of a structure into rapidly converging series. Evjen evaluated the Madelung constant by splitting the crystal into concentric neutral blocks. The relevant point of the method is that the contribution to the electrostatic self potential at a lattice site, due to a neutral shell of ions surrounding the site, consists of positive and negative terms that nearly cancel for shells somewhat removed from the site. The value that one finds for the electrostatic self potential at a given site by summing over a block depends only on the ions included in the block. The Evjen method is not so straightforward and is limited to the NaCl and CsCl structures.

The difficulties encountered in the application of the Evjen method are avoided in the method of evaluation of the Madelung constant by direct summation proposed by Frank.[52] Frank evaluates the Madelung constant of the NaCl structure by dividing the crystal into Wigner-Seitz cubes (polyhedrons whose faces bisect orthogonally the lines joining an ion with its neighbors) of side r and adding to the corners of each cube fictitious fractional charges that neutralize the ionic charge in the center. Since the corners of neighboring cubes touch each other, the charge distribution of the crystal remains effectively unaltered. The zeroth approximation for the NaCl Madelung constant, α, is then given by the potential generated at the negative ion site in the center of a Wigner-Seitz cube by the eight charges of magnitude 1/8 located at its corners:

$$\alpha\,(NaCl) \equiv \frac{8\left(\frac{1}{8}\right)}{\left(\frac{\sqrt{3}}{2}\right)} = 1.155 \cdot \tag{3.3}$$

In this approximation one does not consider the contribution of any neighbor of the negative ion. As a first approximation, one may consider the contributions of all the Wigner-Seitz cubes that touch the cell centered on the negative ion. In this way, one introduces the contributions of the first, second, and third neighbors and of their neutralizing charges. The cubes to be considered form a cube of side $3r$, and the only fractional charges which produce a net effect are those on its corners. One finds:

$$\alpha\,(NaCl) \equiv 6 - \frac{12}{\sqrt{2}} + \frac{8}{\sqrt{3}} - \frac{8\left(\frac{1}{8}\right)}{\left(\frac{\sqrt{3}}{2}\right)} = 1.749\ . \tag{3.4}$$

The Frank method has the attractive qualities of a simple physical interpretation and easy application to summation for off-lattice points. The Madelung potential is shown in Fig. 5 for the NaCl structure along the [100] direction. We have applied the Frank method to the study of point defects in rocksalt structures, including alkali halides, CaO,[53] and MgO. Although Frank implied that his method is applicable to many other cubic structures, we have not been able to implement his technique within zincblende structures.

D. Ewald methods

The electrostatic potential of an infinite ionic crystal can be obtained quite generally by superposing the electrostatic potentials of the component Bravais lattices. Each Bravais lattice is considered to be neutralized by a uniform charge distribution; in order to avoid a divergence in its potential, the neutralizing distributions cancel out in the superposition because of the neutrality of the unit cell of the crystal. This superposition of electrostatic potentials is utilized in the Ewald-type methods. Mathematical descriptions of the method have been given by Born and Huang[54] and by Leibfried.[55] A more physical description of the method has been reported by Kittel.[48] The Ewald method[56] transforms the potential of a Bravais lattice of unit point charges, neutralized by a uniform charge distribution, into an expression consisting of two rapidly convergent series. This is accomplished by splitting the charge distribution under consideration into two components, as illustrated in Fig. 6 for a one-dimensional lattice. The first Ewald component of the charge distribution is a Bravais lattice of Gaussian functions normalized to +1 and neutralized by a uniform,

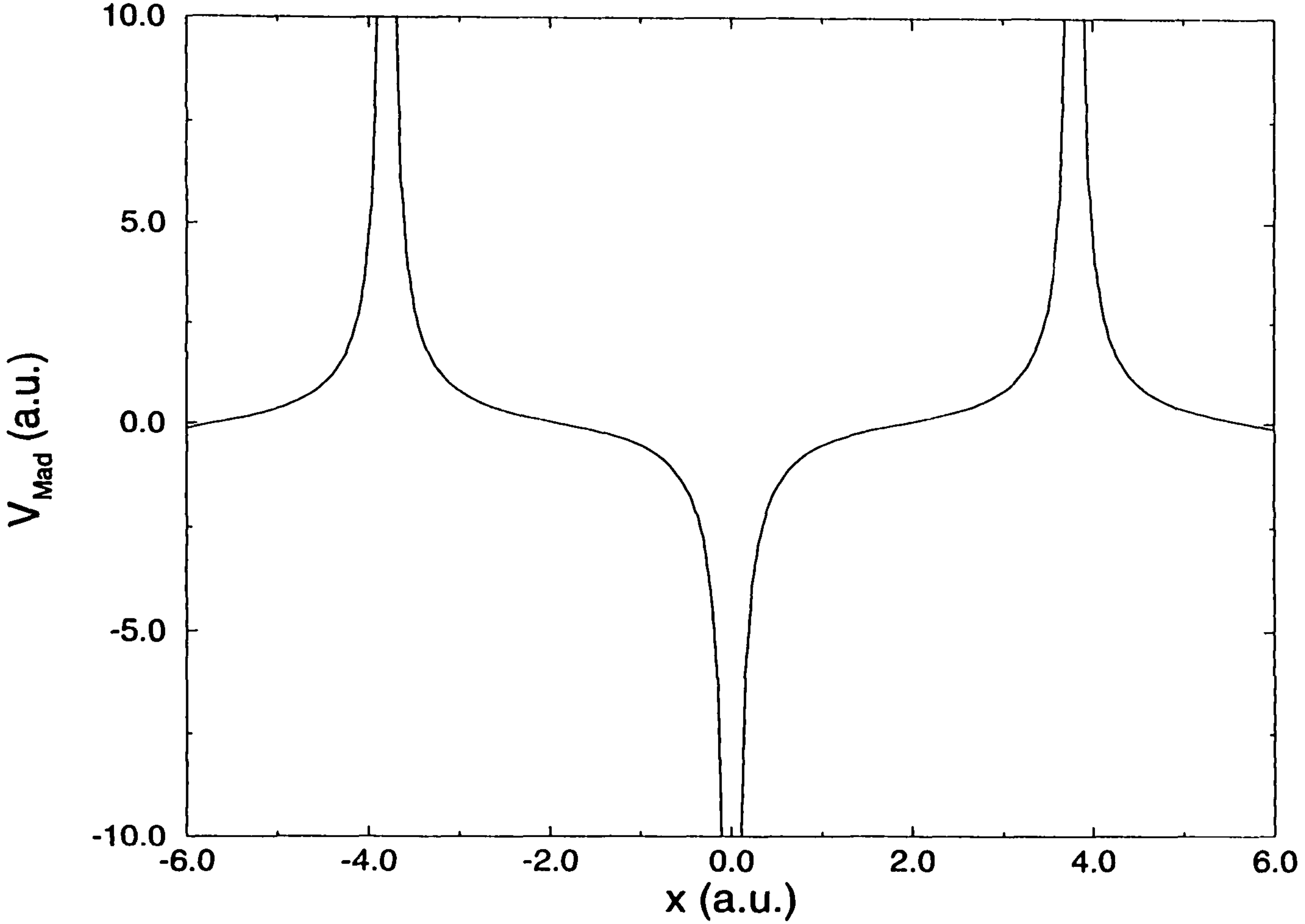

FIG. 5. The crystal potential for the rocksalt crystal structure. The horizontal axis represents the value of x along the [100] direction in the crystal.

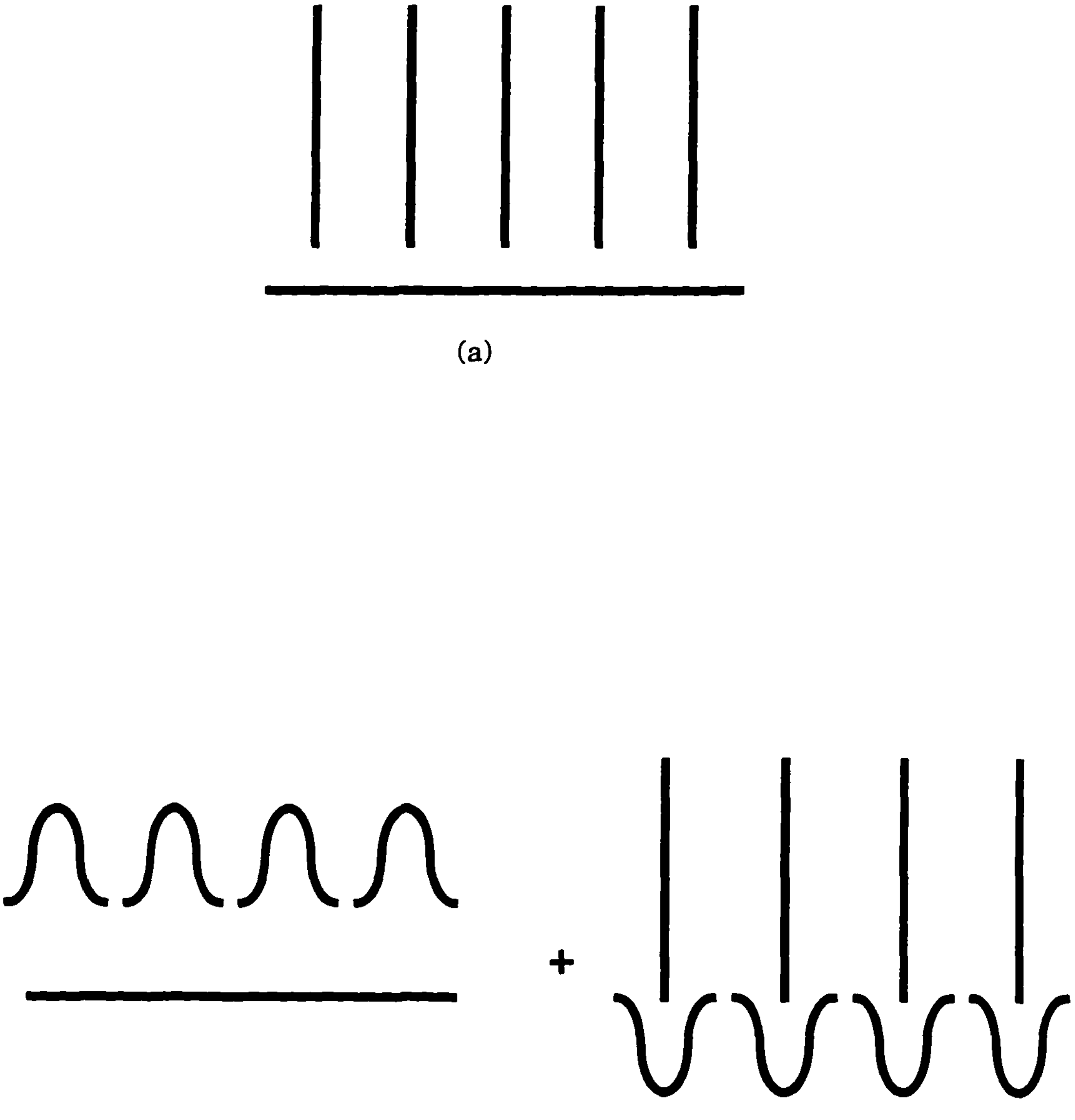

(a)

(b)

FIG. 6. (a) Charge distribution of a neutralized one-dimensional Bravais lattice. The vertical lines represent the unit point charges at the lattice sites, and the horizontal line represents the neutralizing uniform distribution of charge. (b) The Ewald components of the charge distribution (a). Each bell-shaped distribution represents a Gaussian centered on a lattice site and normalized to unity.

negative charge distribution; the second Ewald component is a Bravais lattice of unit point charges and neutralizing Gaussian functions. In the final expression of the required potential, the Fourier representation of the potential generated by the first component is combined with the potential of the second component, and an appropriate value of the half-width of the Gaussian function can thus be chosen so that both series converge rapidly. Physically, the rapid convergence of the two series arises from the fact that the first Ewald component of the charge distribution is smooth, while in the second component the neutralizing charges are piled up around the point charges of the ions.

The first Ewald component of the charge density at the point **r** is

$$\rho_1(r) = \frac{1}{(\eta\sqrt{\pi})^3}\sum_{l} e^{\left[\frac{-(r-r_l)^2}{\eta^2}\right]} - \frac{1}{\Delta} \tag{3.5}$$

where η is the half-width of the Gaussian function, Δ is the volume of the unit cell, and $\mathbf{r}_l$ are the lattice points. Expanding $\rho_1(\mathbf{r})$ into a Fourier series of complex exponentials with the periodicity of the lattice,

$$\rho_1(r) = \frac{1}{\Delta}\sum_{h} e^{\left(-\pi^2\eta^2 k_h^2 + 2\pi i k_h \bullet r\right)} \tag{3.6}$$

where the constant term corresponding to $\mathbf{k}_h=0$ is omitted in order for the charge distribution to remain neutral. In Eq. (3.6), we have capitalized on the fact that the Fourier coefficient corresponding to the reciprocal lattice vector $k_h \neq 0$ is given by

$$\frac{1}{\Delta}\int_{cell} \frac{\sum_{l} e^{\left[\frac{-(r-r_l)^2}{\eta^2} - 2\pi i k_h \bullet r\right]}}{(\eta\sqrt{\pi})^3}\,dr = \frac{1}{\Delta}\int_{space} \frac{e^{\left(-\frac{r^2}{\eta^2} - 2\pi i k_h \bullet r\right)}}{(\eta\sqrt{\pi})^3}\,dr$$

$$= \frac{1}{\Delta} e^{\left(-\pi^2\eta^2 k_h^2\right)} . \tag{3.7}$$

Expressing the potential associated with $\rho_1(\mathbf{r})$ by a Fourier series gives

$$\phi_1(r) = \sum_h V(k_h)\, e^{2\pi i k_h \bullet r} \tag{3.8}$$

where we have used the convention of writing the 2π as part of the Fourier series instead of including it into the reciprocal lattice vector. The coefficients of the Fourier series, $V(\mathbf{k}_h)$, for the potential generated by $\rho_1(\mathbf{r})$, corresponding to $k_h \neq 0$, are evaluated using Eq. (3.6) in Poisson's equation[57]

$$\nabla^2\phi_1(r) = -4\pi\rho_1(r) . \tag{3.9}$$

From Eq. (3.8), it is evident that

$$\begin{aligned} \nabla^2\phi_1(r) &= \nabla^2 \sum_h V(k_h)\, e^{2\pi i k_h \bullet r} \\ &= \sum_h V(k_h)\, \nabla^2\left(e^{2\pi i k_h \bullet r}\right) \\ &= \sum_h V(k_h)\left(-4\pi^2 k_h^2\right)\left(e^{2\pi i k_h \bullet r}\right) \end{aligned} \tag{3.10}$$

Therefore, Poisson's equation and Eq. (3.6) and Eq. (3.10) give the Fourier coefficients for the potential as

$$V(k_h) = \frac{1}{\Delta\pi k_h^2} e^{-\pi^2\eta^2 k_h^2} . \tag{3.11}$$

The potential $\phi_1(\mathbf{r})$ is given by

$$\phi_1(r) = \frac{1}{\pi\Delta}\sum_h \frac{e^{\left(-\pi^2\eta^2 k_h^2 + 2\pi i k_h \bullet r\right)}}{k_h^2} \tag{3.12}$$

where the constant term is omitted by choosing the average potential as zero, as the zero of reference for the potential in an infinite three-dimensional crystal is arbitrary.[58] On the other hand, the second Ewald component of the charge density is

$$\rho_2(r) = \sum_l \left\{ \delta(r - r_l) - \frac{e^{-\frac{(r-r_l)^2}{\eta^2}}}{(\eta\sqrt{\pi})^3} \right\} \tag{3.13}$$

where the point charge densities are represented by delta functions. The corresponding potential is found by using Gauss' theorem[57] to evaluate the electric field at the point $\mathbf{r}$ due to a Gaussian charge distribution centered at $\mathbf{r}_l$, and then integrating by parts:

$$\phi_2(r) = \sum_l \frac{1 - erf\left(\frac{|r - r_l|}{\eta}\right)}{|r - r_l|} - \frac{\pi\eta^2}{\Delta}\ . \tag{3.14}$$

The error function[59] has been used in Eq. (3.14) and is defined by

$$erf(x) = \frac{2}{\sqrt{\pi}}\int_0^x e^{-t^2}dt \tag{3.15}$$

where $\dfrac{erf\left(\frac{|r-r_l|}{\eta}\right)}{|r-r_l|}$ is the potential at the point $\mathbf{r}$ of a Gaussian charge distribution of half-width η, centered at $\mathbf{r}_l$, and normalized to +1. The constant term $-\pi\eta^2/\Delta$ is introduced in Eq. (3.14) so that the average potential is zero. The omission of this term would leave an expression of the potential which diverges in the limit of infinite η.

The potential $\phi(\mathbf{r})$ of the neutralized Bravais lattice of unit point charges is the sum of $\phi_1(\mathbf{r})$ and $\phi_2(\mathbf{r})$:

$$\phi(r) = \sum_h \frac{e^{\left(-\pi^2\eta^2 k_h^2 + 2\pi i k_h \bullet r\right)}}{\pi \Delta k_h^2} + \sum_l \frac{1 - erf\left(\frac{|r - r_l|}{\eta}\right)}{|r - r_l|} - \frac{\pi\eta^2}{\Delta} . \qquad (3.16)$$

The potential $\phi(\mathbf{r})$ is independent of the half-width η of the Gaussian function. The component $\phi_2(\mathbf{r})$ vanishes in the limit $\eta \to 0$, and converges rapidly for small η's, whereas, the component $\phi_1(\mathbf{r})$ vanishes in the limit $\eta \to \infty$ and converges rapidly for large η's. A proper choice of η ensures rapid convergence for both components.The Bravais symmetry ensures that the potential is known everywhere once it is known inside the unit cell. The mapping of the potential inside the unit cell can be further simplified by expanding it into lattice harmonics as discussed by de Wette and Nijboer.[60,61,62] It is important to note that the Ewald method is applicable to any point **r** in space. However, the Ewald method is most efficient for crystals that exhibit inversion symmetry because of the complex expression in $\phi_1(\mathbf{r})$.

E. Hund's relations

From the Ewald method, the rotation and reflection symmetry imply that the potential need not be computed at all points inside the unit cell. Other consequences of symmetry, which have been pointed out by Hund,[63] allow one to derive linear relationships between values of the potential at crystallographically nonequivalent points of the unit cell. So to evaluate the crystal potential of a series of structures based on the same Bravais lattice by the Ewald method, it is convenient to express the electrostatic potentials of the structures in terms of the electrostatic potential $\phi(\mathbf{r})$ of the appropriate Bravais lattice of unit point charges, neutralized by a uniform distribution of charge. The ensuing expressions are considerably simplified by the use of the rotation and reflection symmetry of the Bravais lattice, and by linear relationships between values of $\phi(r)$ at different points of the unit cell that are a rather subtle consequence of symmetry. Tosi[50] has illustrated these relationships for the particular case of a neutralized simple cubic lattice. The potential at the point (xa, ya, za) of the unit cell of a simple cubic lattice of lattice parameter a can be regarded as the sum of the potentials arising from the eight simple cubic lattices of side $2a$ that can be thought to compose the given lattice (Fig. 7). The coordinates of the point (x, y, z) when referred to the latter lattices are (x/2, y/2, z/2), [(x-1)/2, y/2, z/2], (x/2, (y-1)/2, z/2), (x/2, y/2, (z-1)/2), [(x-1)/2, (y-1)/2, z/2], [(x-1)/2, y/2, (z-1)/2], (x/2, (y-1)/2, (z-1)/2), and [(x-1)/2, (y-1)/2, (z-1)/2]. Also, the electrostatic potential arising from a simple cubic lattice of side $2a$, at the point of coordinates (ξ, η, ζ) measured in units $2a$, is equal to one half of the electrostatic potential arising from a simple cubic lattice of side a, at the point of coordinates (ξ, η, ζ) measured in units a. Thus, the Hund identity follows:

$$\begin{aligned}\phi(x, y, z) = (1/2)[&\phi(x/2, y/2, z/2) + \phi((x-1)/2, y/2, z/2)\\ &+ \phi(x/2, (y-1)/2, z/2) + \phi(x/2, y/2, (z-1)/2)\\ &+ \phi((x-1)/2, (y-1)/2, z/2) + \phi((x-1)/2, y/2, (z-1)/2)\\ &+ \phi(x/2, (y-1)/2, (z-1)/2) + \phi((x-1)/2, (y-1)/2, (z-1)/2)]\,. \qquad (3.17)\end{aligned}$$

For special values of (x, y, z), the terms of the right-hand side group together because of the cubic symmetry. So one has, for instance,

$$\phi(1/2, 1/2, 1/2) = 4\phi(1/4, 1/4, 1/4)\,. \qquad (3.18)$$

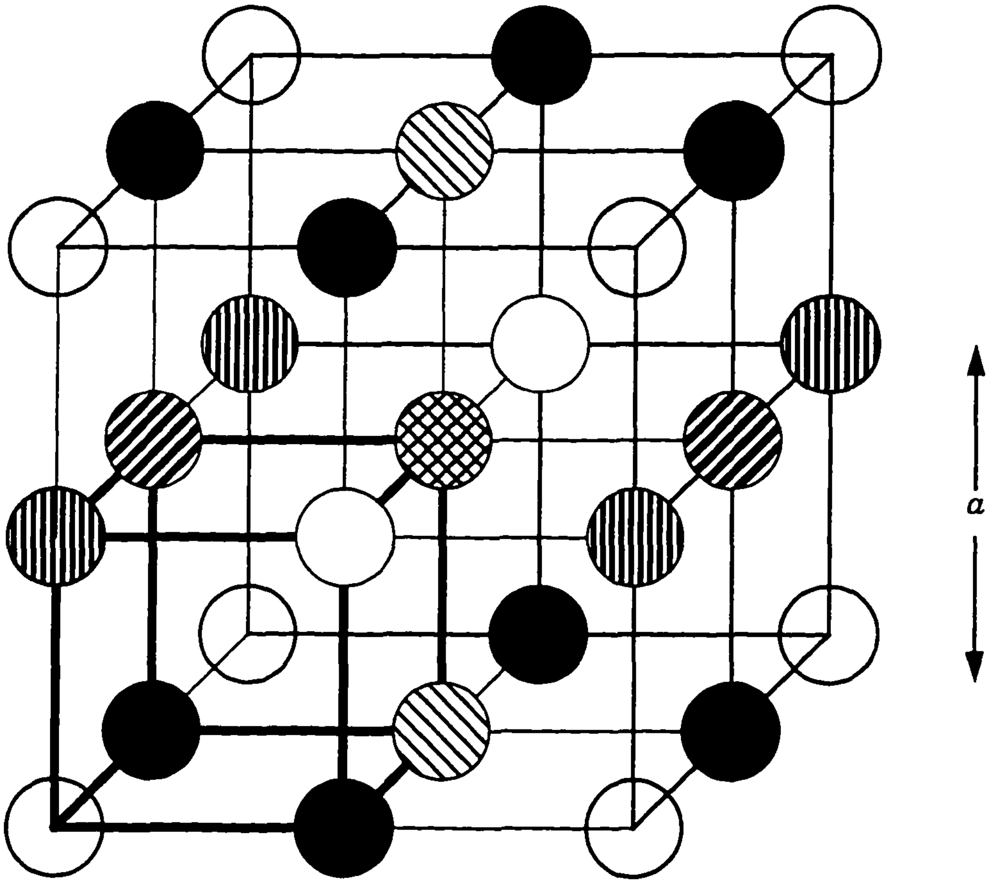

FIG. 7. Shown are sections of the eight simple cubic lattices of side $2a$ composing a simple cubic lattice of side a. Circles of the same pattern represent corners of one of the larger simple cubic lattices. The smaller simple cubic lattice of side a is shown with darkened edges.

The generalization of the identity Eq. (3.17) for a simple cubic lattice is

$$\phi(x, y, z) = \frac{1}{m} \sum_{n_1=0}^{m-1} \sum_{n_2=0}^{m-1} \sum_{n_3=0}^{m-1} \phi\left(\frac{x-n_1}{m}, \frac{y-n_2}{m}, \frac{z-n_3}{m}\right) \tag{3.19}$$

where m is an arbitrary positive integer. Similar identities can be derived for the other Bravais lattices.

To evaluate the crystal potential of other cubic structures, we express first, following Hund,[63] the electrostatic potential $\varphi(x, y, z)$ at the point (xa, ya, za) in the unit cell of each structure through the electrostatic potential $\phi(x, y, z)$ at the point (xa, ya, za) in the unit cell of a neutralized simple cubic lattice of positive unit point charges. The relevant equations, taking positive ions at the origin, are as follows:

$$\varphi_{CsCl}(x, y, z) = \phi(x, y, z) - \phi(x-1/2, y-1/2, z-1/2) \tag{3.20}$$

$$\begin{aligned}\varphi_{NaCl}(x, y, z) = {} & \phi(x, y, z) + \phi(x-1/2, y-1/2, z) + \phi(x-1/2, y, z-1/2) \\ & + \phi(x, y-1/2, z-1/2) - \phi(x-1/2, y, z) - \phi(x, y-1/2, z) \\ & - \phi(x, y, z-1/2) - \phi(x-1/2, y-1/2, z-1/2)\end{aligned} \tag{3.21}$$

$$\begin{aligned}\varphi_{ZnS}(x, y, z) = {} & \phi(x, y, z) + \phi(x-1/2, y-1/2, z) + \phi(x-1/2, y, z-1/2) \\ & + \phi(x, y-1/2, z-1/2) - \phi(x-1/4, y-1/4, z-1/4) \\ & - \phi(x+1/4, y+1/4, z-1/4) - \phi(x+1/4, y-1/4, z+1/4) \\ & - \phi(x-1/4, y+1/4, z+1/4)\end{aligned} \tag{3.22}$$

$$\begin{aligned}\varphi_{CaF2}(x, y, z) = {} & 2\phi(x, y, z) + 2\phi(x-1/2, y-1/2, z) + 2\phi(x-1/2, y, z-1/2) \\ & + 2\phi(x, y-1/2, z-1/2) - 2\phi(2x-1/2, 2y-1/2, 2z-1/2)\end{aligned} \tag{3.23}$$

$$\begin{aligned}\varphi_{Cu2O}(x, y, z) = {} & \phi(x, y, z) + \phi(x-1/2, y-1/2, z) + \phi(x-1/2, y, z-1/2) \\ & + \phi(x, y-1/2, z-1/2) - 2\phi(x-1/4, y-1/4, z-1/4) \\ & - 2\phi(x+1/4, y+1/4, z+1/4).\end{aligned} \tag{3.24}$$

The values of the electrostatic potential $\phi(x, y, z)$ in the neutralized simple cubic lattice can quickly be determined by using the Ewald Method described in Eq. (3.16).

We have utilized Hund's relations in our calculation of the embedding potential for the zincblende lattice. Even with the Hund relations, calculation of the embedding potential can be a time consuming step in the LCAO cluster codes. A method utilized to parallelize the computation of the embedding potential and other aspects of the code is discussed in Appendix B. Fig. 8 shows the calculated potential along the [111] direction in the zincblende lattice of cubic boron nitride.

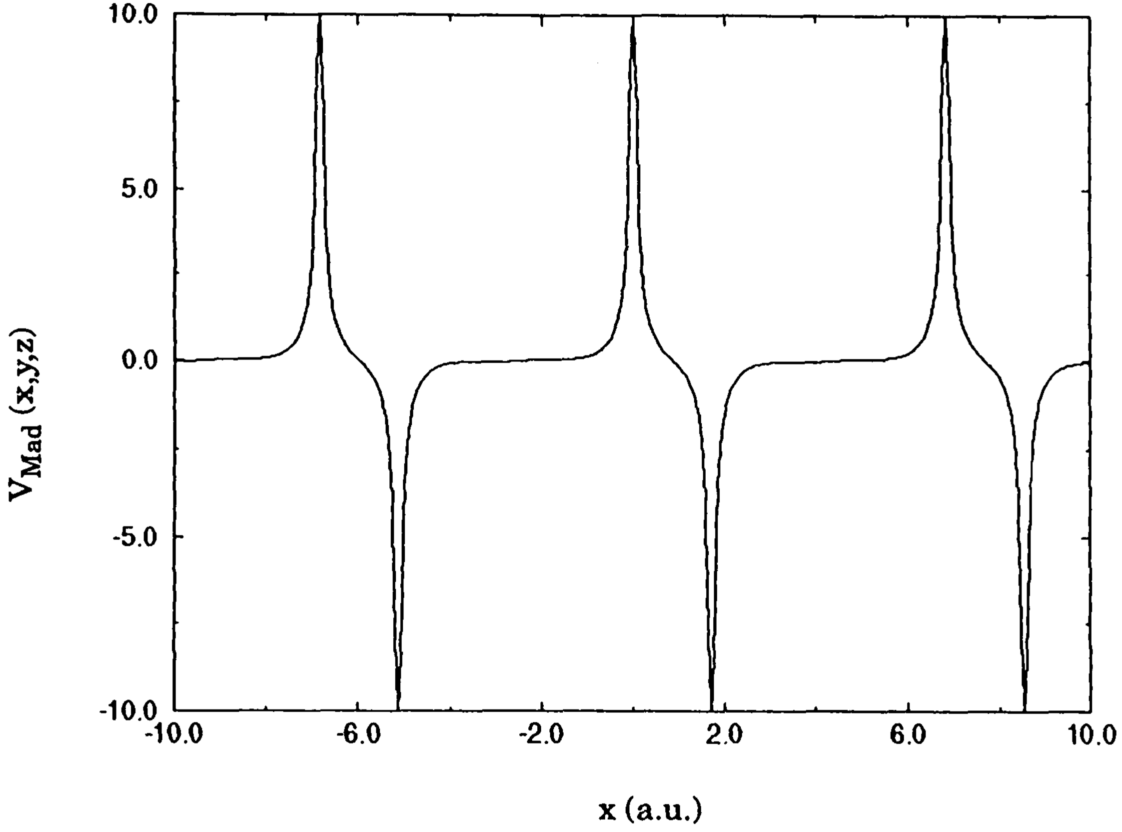

FIG. 8. The Madelung potential along the [111] direction in the zincblende lattice with a lattice constant of 6.381 a.u.

CHAPTER IV

ELECTRONIC STRUCTURE

The electronic structure of substitutional defects in cubic boron nitride clusters is one of the most important factors when considering them for application as *p*- and *n*-type dopants. In this section, calculations of electronic structure have been performed with the LCAO cluster codes discussed in Chapter II. These codes allow us to study both the electronic structure and defect-induced structural changes in the geometry of the clusters. The Gaussian exponents utilized in the basis sets by the LCAO cluster codes are tabulated in Table II for each atom. The contraction coefficients used in the basis sets are given for boron in Table III, for nitrogen in Table IV, for hydrogen in Table V, for beryllium in Table VI, and for silicon in Table VII.

When discussing the electronic structure of a system, we will often refer to the orbital eigenvalues and the density of states. The density of states is a representation of the distribution of electronic states in the energy space of a cluster. It counts the number of eigenstates per unit energy in the neighborhood of a particular value of the energy, E. The number of states per unit energy, *n*, can be defined as

$$n(E) = \sum_i \delta(E - \varepsilon_i) \tag{4.1}$$

where δ is the Dirac δ-function; ε_i are the energy eigenvalues of the eigenstates. In a finite system, like a cluster, the eigenvalues ε_i are discrete values. In such a case, *n*(E) represents a collection of peaks with infinite height and zero width, that occur at

TABLE II. The Gaussian exponents utilized in the basis sets of each type of atom by the LCAO cluster codes.

boron	nitrogen	hydrogen	beryllium	silicon
12149.300	22817.870	4.50038000	30176.700	26309.320
1820.8320	3025.6340	0.68127700	4506.1660	3948.5770
414.31530	619.78940	0.15137400	1014.1360	898.90420
117.30380	163.45230		278.28180	254.28510
38.201460	50.611880		88.495770	82.282210
13.634590	17.322670		31.283730	29.060560
5.1687100	6.3093750		11.792250	10.464420
1.9908150	2.2959410		4.7910830	3.8216270
0.6111868	0.8193595		2.3845370	1.3842760
0.2703730	0.2703301		1.0054450	0.3604883
0.1106789	0.0689153		0.2346328	0.1296625

TABLE III. The contraction coefficients used in the basis set of boron.

1*s*	2*s*	3*s*	2*p*	3*p*	3*d*
-0.1674017	-0.0400882	0.02926312	0.00256518	0.06260111	-0.7567586
-0.3127616	-0.0764672	0.04803730	0.09326686	-0.1620154	0.52512365
-0.5354137	-0.1277466	0.09951308	0.04916389	0.07361840	-0.3649833
-0.8419727	-0.2117628	0.12260241	0.20944614	-0.2958450	0.23762368
-1.1694869	-0.2869014	0.24450503	0.17119896	0.01932949	-0.1892042
-1.3153617	-0.3779177	0.18606974	0.34057926	-0.4326083	0.10226920
-1.0098085	-0.3472018	0.37078419	0.30349964	-0.0738066	-0.1083695
-0.3644600	-0.2045949	0.00099176	0.45719599	-0.5158119	0.01006534
-0.0193191	0.07061905	0.21710219	0.27600085	-0.0904049	-0.0668382
0.00239808	0.17113233	-0.6681091	0.10586289	-0.2728575	0.00524532
-0.0002753	0.04770641	0.30413606	0.02686159	0.13364819	-0.0345775

TABLE IV. The contraction coefficients used in the basis set of nitrogen.

1*s*	2*s*	3*s*	2*p*	3*p*	3*d*
-0.3037010	-0.0684307	0.02795965	0.07202304	-0.0022142	1.1370759
-0.6175038	-0.1394753	0.05231287	0.14250821	0.14676219	-0.8149142
-1.1016681	-0.2499578	0.10597267	0.26042821	0.07217341	0.55249744
-1.7372396	-0.4026192	0.14485802	0.42344393	0.34401360	-0.3720020
2.3222688	-0.5614600	0.25572885	0.63162833	0.25850779	0.26649291
-2.2951702	-0.6498658	0.20820184	0.81738725	0.59995737	-0.1684474
-1.1966076	-0.5156101	0.27949556	0.88955074	0.40347806	0.12494093
-0.1494537	-0.0519568	-0.0829863	0.76063183	0.56373916	-0.0579163
-0.0051458	0.27940394	0.00897375	0.40607549	0.15095094	0.04774843
0.00106878	0.15675202	-0.2724280	0.11014638	0.15049060	-0.0162063
-0.0000933	0.01092425	0.13837470	0.01505351	-0.0568691	0.01584676

TABLE V. The contraction coefficients used in the basis set of hydrogen.

1*s*
-0.1149800
-0.1404700
-0.0717950

each value of ε_i. In the infinite crystal, the states are distributed continuously and *n*(E) will be smooth. Thus, for discrete systems, it is customary to approximate a continuum by broadening the states with a normalized Gaussian function. This can be used to compute a function, g(E), which resembles the density of states of the crystal:

$$g(E) = \frac{1}{\Delta\sqrt{\pi}}\sum_i e^{-\left(\frac{E-\varepsilon_i}{\Delta}\right)^2} \qquad (4.2)$$

where Δ is the width of the Gaussian, an arbitrary parameter, typically about 0.3 eV.

TABLE VI. The contraction coefficients used in the basis set of beryllium.

1*s*	2*s*	2*p*
0.060239859	-0.015829928	0.0095508105
0.112080350	-0.034199826	-0.040905984
0.199891040	-0.049085202	0.0022026304
0.329422940	-0.106703600	-0.083652078
0.510622810	-0.116636370	-0.032194760
0.708859320	-0.257018290	-0.158686680
0.864539270	-0.174608690	-0.089614578
0.672072300	-0.407866350	-0.222062140
0.424274640	0.0158795020	-0.083799459
0.180930620	-0.281588530	-0.247119500
0.002905185	0.2928018800	-0.205633220

TABLE VII. The contraction coefficients used in the basis set of silicon.

1*s*	2*s*	3*s*	2*p*	3*p*	3*d*
-1.5605588	-0.4124863	0.12503216	1.1162462	-0.2639801	1.7100516
-2.8926404	-0.7675674	0.23392260	2.2208593	-0.6336407	-1.1103398
-4.8054133	-1.2981299	0.39347497	3.6290259	-0.9060273	0.92854392
-6.8143627	-1.9333681	0.59574033	5.8699334	-1.6261393	-0.3690238
-7.2246796	-2.3855570	0.73252107	7.8557310	-2.0208422	0.66294036
-3.9839243	-1.9636530	0.63104756	9.1916449	-2.5797449	0.09111600
-0.5826035	-0.1806871	0.05362494	7.5889551	-2.0298523	0.53900405
0.01736378	1.0696760	-0.4369356	3.5054752	-1.1442464	0.17353138
-0.0038183	0.50525555	-0.3666617	0.70834443	-0.0911417	0.27351764
0.00051062	0.01342618	0.15897169	0.01571973	0.18154593	0.06794445
-0.0000874	-0.0008969	0.11231594	-0.0008263	0.06986845	0.03669848

As was discussed in Chapter II, to correctly study defects in solids with cluster methods, the electronic structure due to the host cluster must accurately reproduce that of the crystal in the region where the defect resides. One of the most important concerns when using cluster methods that must be addressed is that of dangling bonds at the cluster surface. We have chosen to saturate these dangling bonds with hydrogen atoms. This has a dramatic effect on the electronic structure of the cluster. In particular the band gap of the hydrogen saturated cluster is free of dangling-bond states, as is shown in Fig. 9 for an unembedded 29-atom cubic boron nitride cluster. A bond distance of 1.1 a.u. for the boron-hydrogen bonds and 1.1 a.u. for the nitrogen-hydrogen bonds has been utilized for all hydrogen saturated clusters. This bond distance was found to consistently work well for saturating dangling bonds in many different sized clusters.

Another concern when using cluster methods is how large a cluster is necessary to simulate the electronic environment of the host crystal. In Table VIII, the eigenvalues of the highest occupied molecular orbital (HOMO), lowest unoccupied molecular orbital (LUMO), and band gap (LUMO-HOMO) are given for clusters of varying size. These clusters were not embedded and were not allowed to relax from the bulk geometry. Clusters centered around boron atoms have the number of borons in the cluster name listed first (e.g., BN_4H_{12}). Nitrogen centered clusters have the number of nitrogens in the name listed first (e.g., $N_{13}B_{16}H_{36}$). In Table IX, the highest occupied level, lowest unoccupied level, and band-gaps are given for some of these same clusters when they are embedded using the method discussed in Chapter III. The clusters range in size from 5 atoms to 35 atoms (hydrogen atoms are not included in the descriptions of the cluster size). They are built up by adding shells of symmetrically equivalent atoms. First a shell of 4 atoms is added to a single atom at the center of

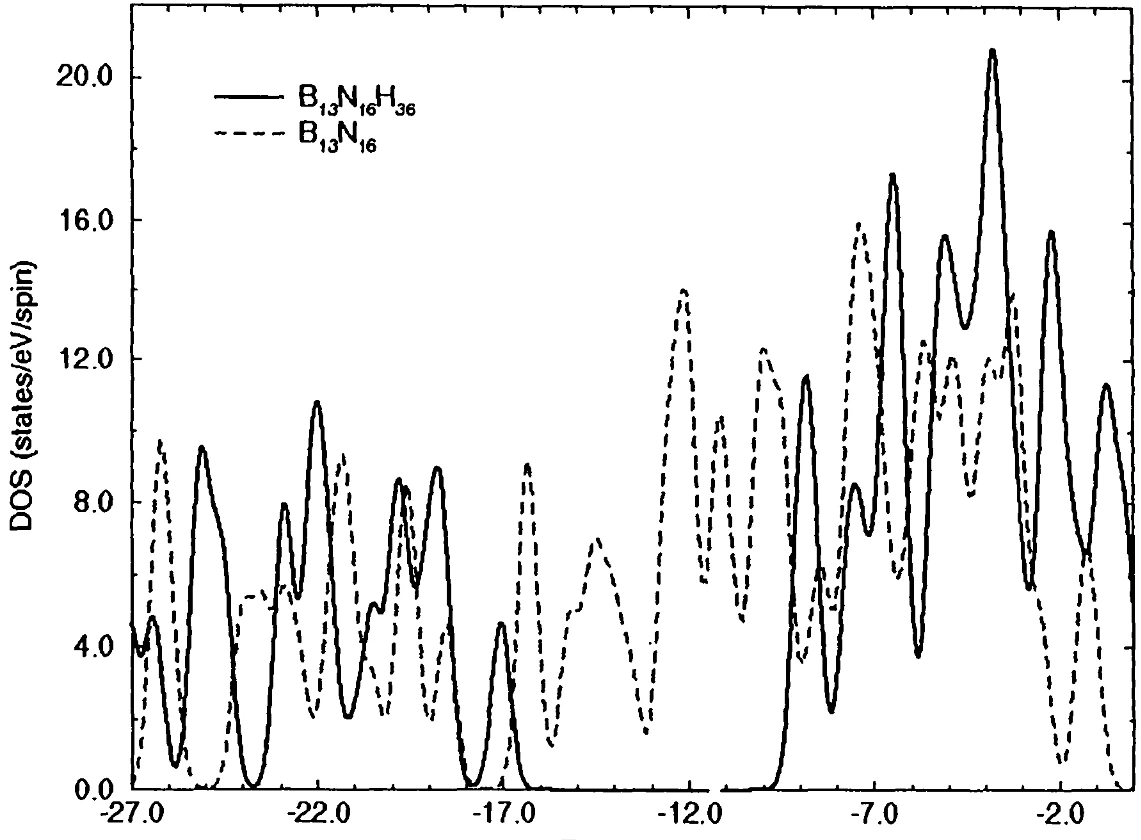

FIG. 9. Density of states of cubic boron nitride with and without hydrogen saturated dangling bonds. The highest occupied molecular orbital (HOMO) level of the $B_{13}N_{16}H_{36}$ cluster is at -17.07 eV and the HOMO level of the $B_{13}N_{16}$ cluster is at -11.23 eV.

TABLE VIII. The lowest unoccupied molecular orbital (LUMO) eigenvalue, the highest occupied molecular orbital (HOMO) eigenvalue, and the (LUMO-HOMO) band-gap are given for clusters of cBN ranging from 5 to 35 atoms. All clusters were calculated without embedding.

cluster	LUMO (a.u.)	HOMO (a.u.)	band-gap (eV)
BN_4H_{12}	-0.543838	-1.09475	14.99
NB_4H_{12}	0.422065	0.336161	2.34
$B_{13}N_4H_{36}$	0.874489	0.863318	0.30
$N_{13}B_4H_{36}$	-1.40814	-1.84262	11.82
$B_{13}N_{16}H_{36}$	-0.331047	-0.625202	8.00
$N_{13}B_{16}H_{36}$	0.324376	0.190736	3.64
$B_{19}N_{16}H_{36}$	0.308179	0.180016	3.49
$N_{19}B_{16}H_{36}$	-0.332101	-0.629324	7.84

TABLE IX. The lowest unoccupied molecular orbital (LUMO) eigenvalue, the highest occupied molecular orbital (HOMO) eigenvalue, and the (LUMO-HOMO) band-gap are given for clusters of cubic boron nitride ranging from 5 to 29 atoms. All clusters were calculated with embedding.

cluster	LUMO (a.u.)	HOMO (a.u.)	band-gap (eV)
BN_4H_{12}	-0.822677	-1.38832	15.39
NB_4H_{12}	0.535839	0.491011	1.22
$B_{13}N_4H_{36}$	1.14478	1.14193	0.08
$N_{13}B_4H_{36}$	-1.97437	-2.40832	11.80
$B_{13}N_{16}H_{36}$	-0.488105	-0.755022	7.26
$N_{13}B_{16}H_{36}$	0.490534	0.481862	0.24

the cluster forming a 5-atom cluster. Then a shell of 12 more atoms is added forming a cluster of 17 atoms. Next the cluster grows to 29 atoms and then to 35 atoms.

From Table VIII, it is evident that the band-gap is strongly dependent on whether the cluster contains more boron atoms or more nitrogen atoms. The clusters with more borons have smaller band-gaps than those with more nitrogen atoms. This is a direct result of our method of electron filling discussed in Chapter II. Because the borons are populated with six electrons, they contribute a charge of -1 to the overall charge of the cluster. The nitrogens are also populated with six electrons and thus give the cluster a positive charge. In the crystalline form, cubic boron nitride is stoichiometrically a binary compound with equivalent amounts of boron and nitrogen atoms. Using a cluster method, it is not always possible to form a cluster with the same stoichiometry as the crystal. However, as the cluster becomes larger, the non-equivalent numbers of borons and nitrogens become less important and the band-gap begins to converge. The relation of the band-gap to cluster size is shown for clusters containing three more borons than nitrogens and those containing three more nitrogen than borons is shown in Fig. 10. In order to investigate the convergence of the band-gap with cluster size and eliminate the effects of non-stoichiometric compositions, we looked at the average of equivalently sized nitrogen centered and boron centered clusters. Fig. 11 shows the convergence of the band-gap. Studies[33] of the convergence of the band-gap in diamond with cluster size have shown good agreement with the bulk value by 29 atoms. Our results suggest similar behavior in cubic boron nitride in which the band-gap appears to be converging to about 5.55 eV. This value compares nicely to the true value of 6.4 eV since the LDA generally underestimates band-gaps. The band-gap, 5.55eV, to which we have extrapolated represents a 13% underestimation of the band-gap.

We want to choose clusters that tend to come close to the crystalline stoichiometry. In the case of cubic boron nitride, the 29 atom and 35 atom clusters are the best choices. We chose to study the 29 atom cluster, $B_{13}N_{16}H_{36}$, because it was computationally feasible and the electronic structure of the gap was closer to that of the crystal. Furthermore, the gap is large enough to easily study defect states in the gap and the highest occupied and lowest unoccupied levels coincide well with that of LDA

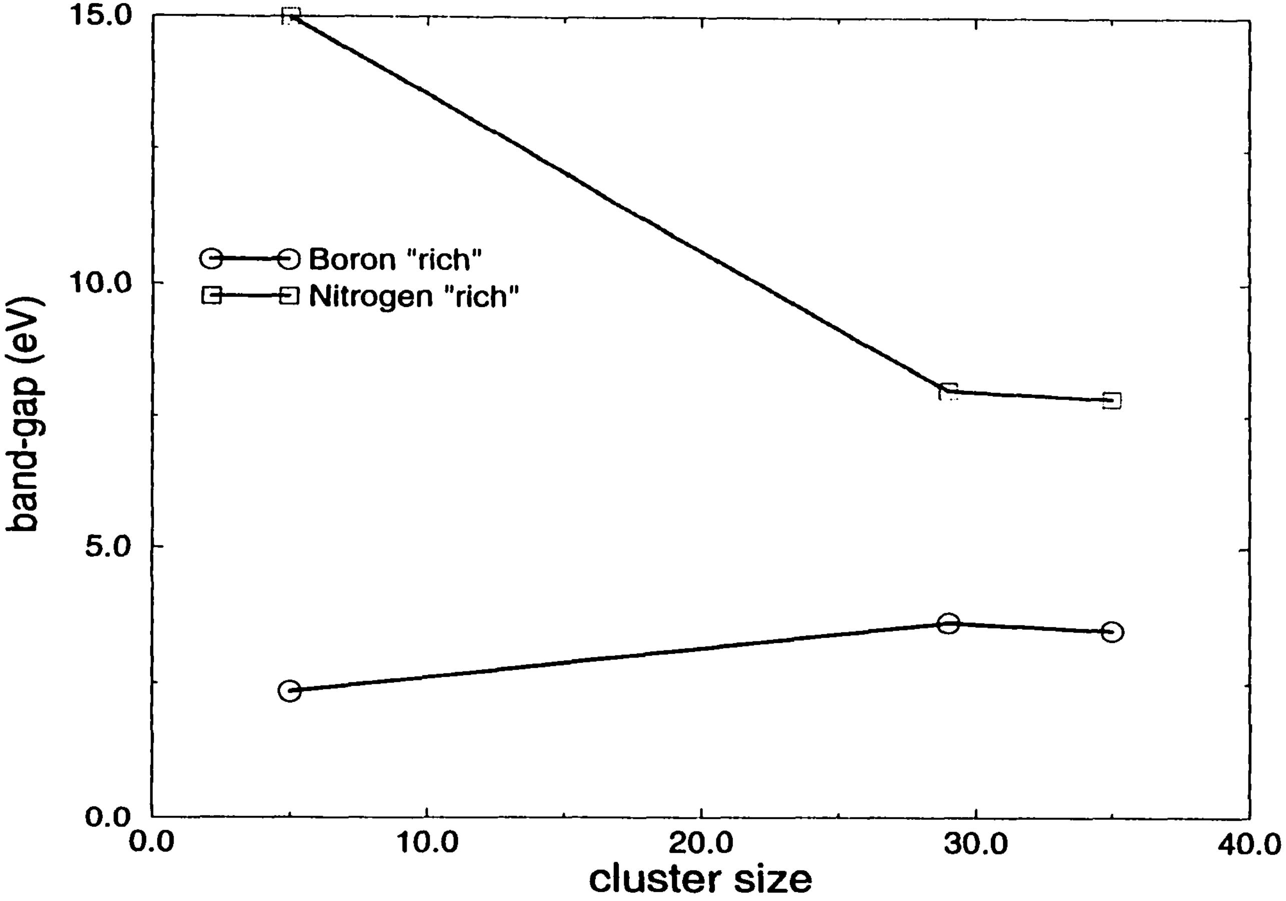

FIG. 10. Convergence of the band-gap for clusters of cBN with non-stoichiometric compositions. Boron "rich" clusters contain three more B atoms than N atoms. Nitrogen "rich" clusters contain three excess N atoms. The cluster sizes given along the horizontal axis do not count the hydrogen atoms.

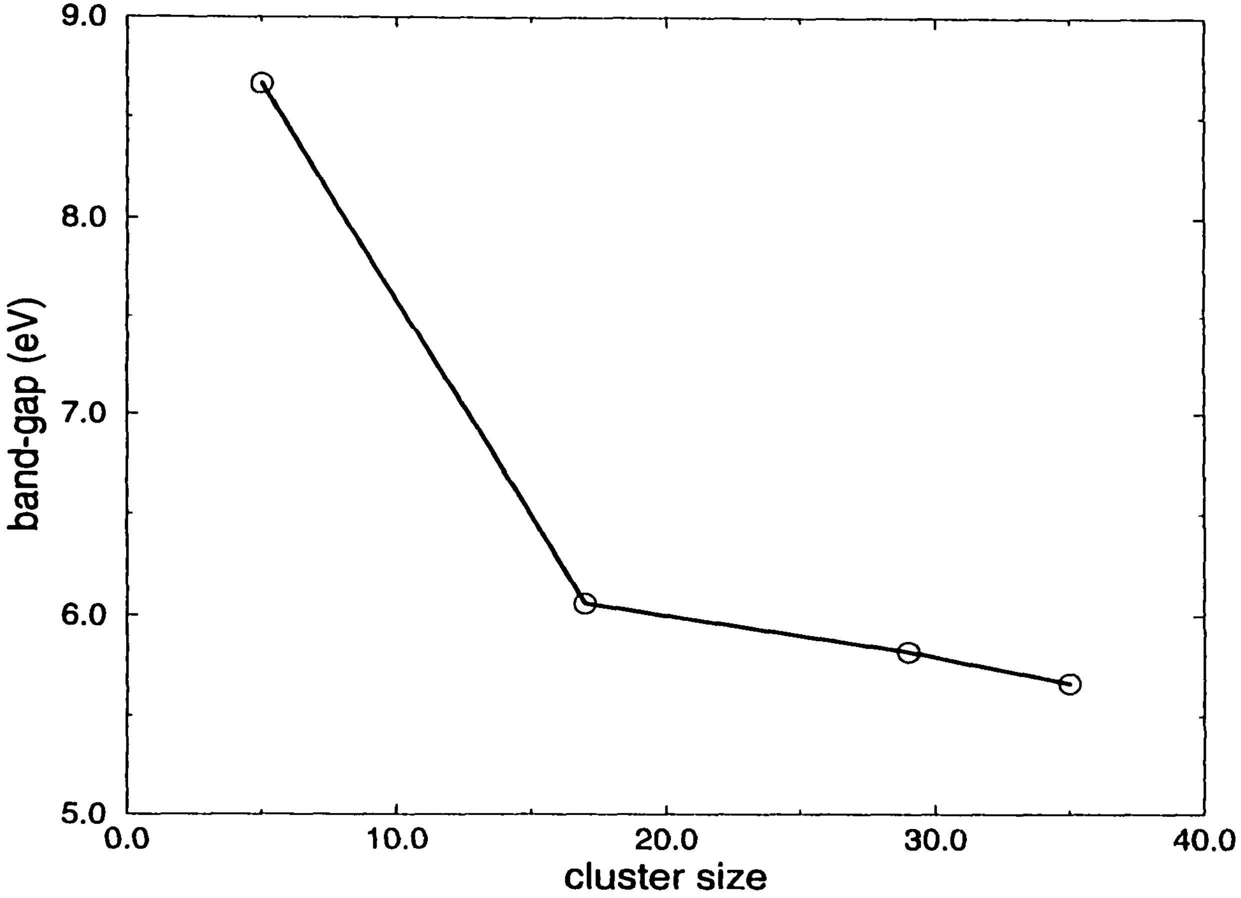

FIG. 11. Convergence of the band-gap with cluster size. Values marked with circles are at 5 atoms, 17 atoms, 29 atoms, and 35 atoms (hydrogen atoms used to saturate dangling bonds are not counted).

band structure calculations.[64] Fig. 12 is a comparison of the electronic density along the B-N bond calculated by the cluster method versus a summation of atomic densities. This electronic charge density plot is almost identical to that given in the band structure calculation of Dovesi *et al.*[65] Fig. 13, shows the charge density difference between the superposition of atomic densities and the cluster density. This charge density difference demonstrates an accumulation of extra charge on the electronegative nitrogen site and a deficiency of charge at the boron site indicative of ionic bonding. In addition, there is a buildup of charge in the interstitial region indicating covalent bond formation. This is in good agreement with the band structure calculations.[64]

Now that a sufficiently large cluster has been chosen to study, the importance of embedding will be evaluated. The embedding model used in the calculated results given in Table IX was done with an ionic charge of +.35 for the boron sites and -.35 for the nitrogen sites. This ionicity value was taken from the *first-principles* LDA band structure calculations of Zunger and Freeman.[64] It is evident from the results for embedded clusters that the embedding potential produces an almost uniform shift in the eigenvalues of the cluster. Fig. 14 shows a plot of this embedding potential for the $B_{19}N_{16}H_{36}$ cluster. This shows that the effect of embedding in cubic boron nitride is basically to put the cluster into a potential well. Furthermore, the shift in the eigenvalues does not always bring them closer to the crystalline results of band structure calculations.[65,64] The cause of this is the way in which we populate the clusters to assure proper sp^3 hybrid bonding. As is discussed in several band structure calculations,[64,66] the top of the valence band is primarily composed of nitrogen 2*p* states and the bottom of the conduction band is primarily boron 2*p*-like. In Table X, we show the results of both atoms and ions embedded and not embedded. The ions are populated

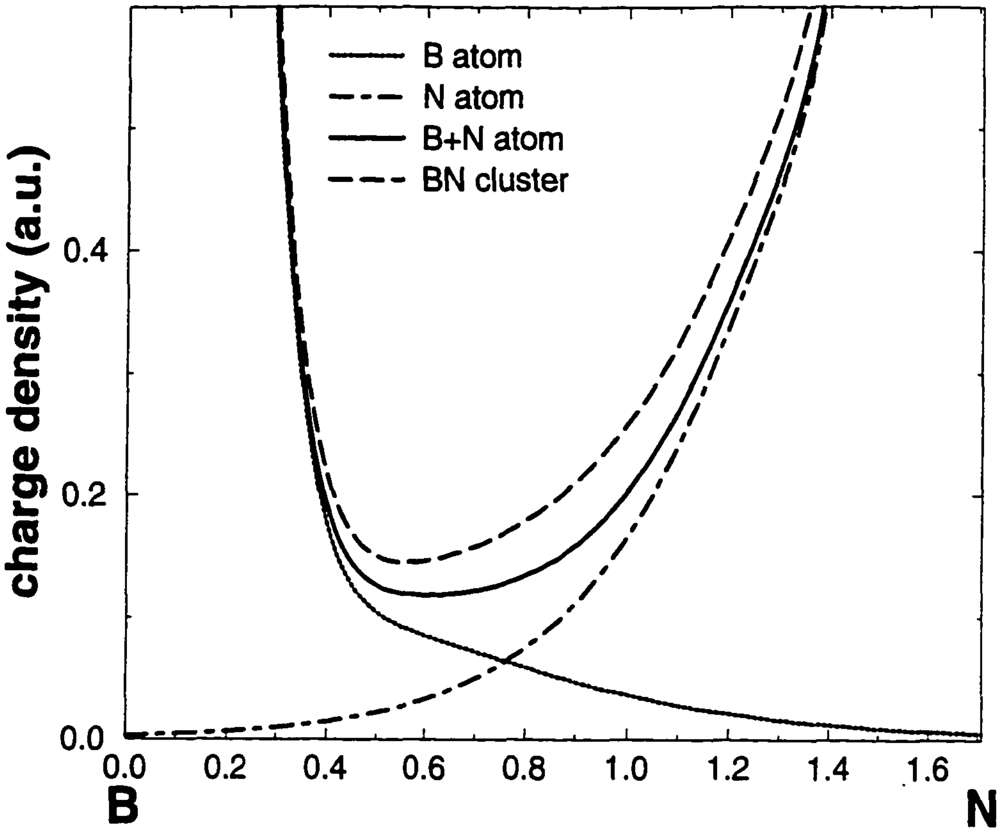

FIG. 12. Electronic charge density along the boron-nitrogen bond as calculated for a 29-atom cluster versus a summation of atomic densities.

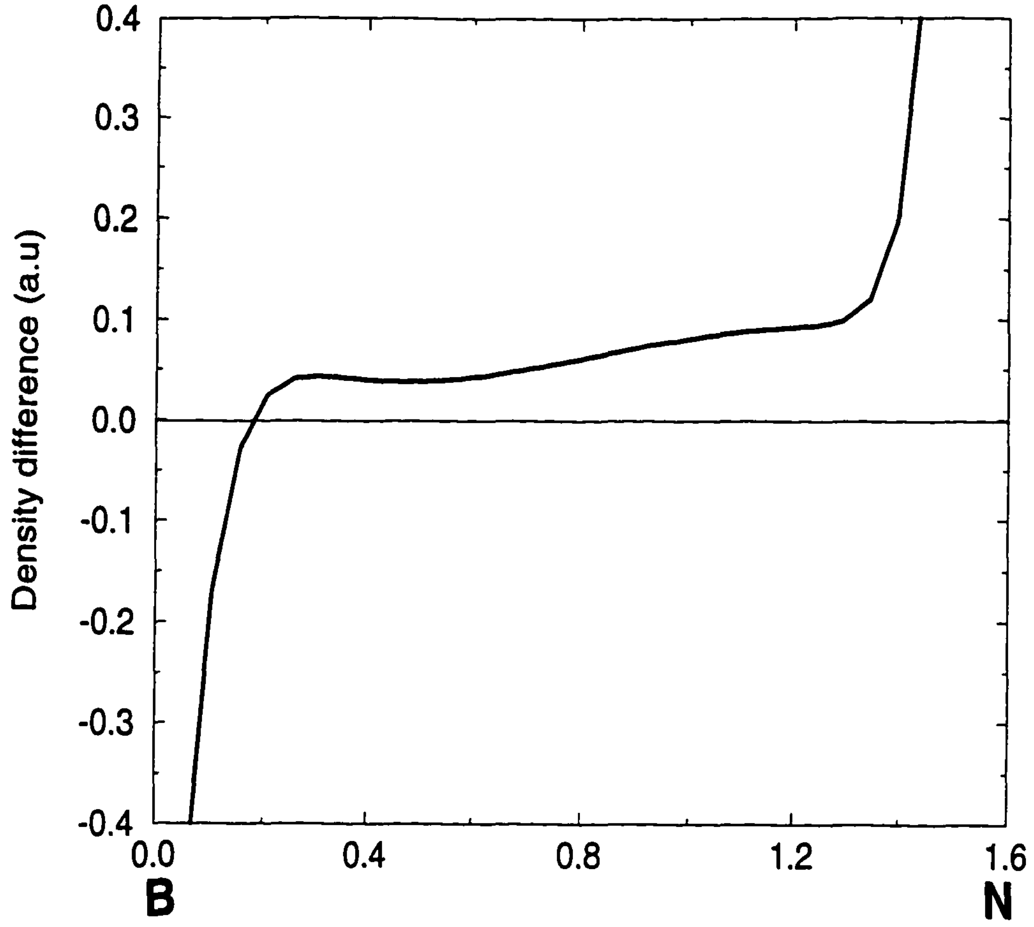

FIG. 13. Charge density difference between the values obtained in the superposition of atomic densities and the cluster density. Positive values indicate larger cluster charge density. Negative values indicate larger atomic charge densities.

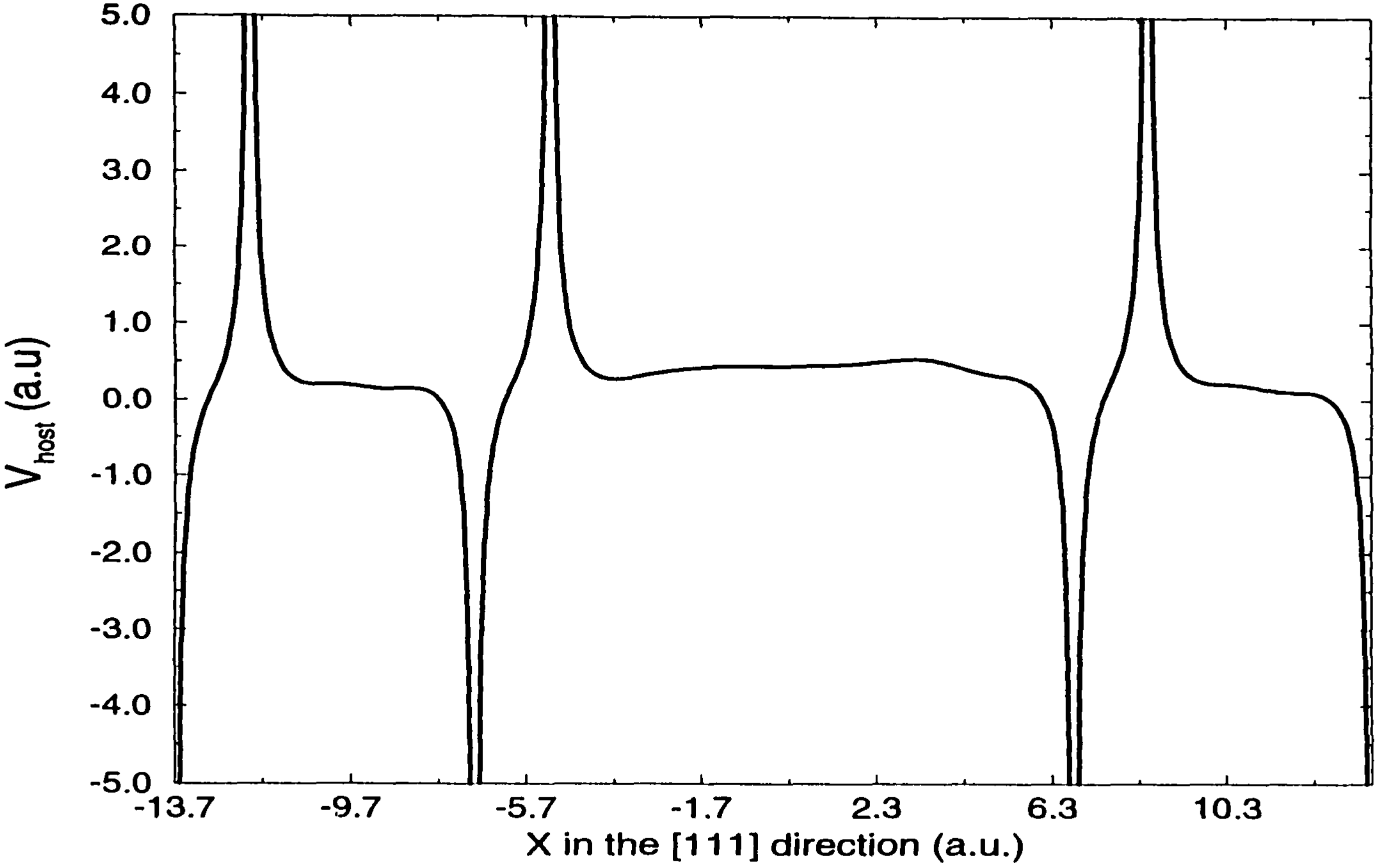

FIG. 14. The embedding potential, V_{host}, for a 35 atom boron centered cluster is shown along the [111] direction. Note that the potential has a non-zero, positive value in the region where the cluster resides (about x=-1.9 to x=+1.9).

TABLE X. Non-spin polarized calculations of the electronic structure of boron and nitrogen atoms and ions. The lowest unoccupied molecular orbital eigenvalue and highest occupied molecular orbital eigenvalue are given (in a.u.) for each system in both the embedded and unembedded case.

system	level	free	embedded
B atom	LUMO	0.144924	0.207032
	HOMO	-0.134531	0.001404
N atom	LUMO	0.295827	-0.142935
	HOMO	-0.260021	-0.434861
B^+ ion	LUMO	0.371043	0.412362
	HOMO	0.136199	0.223435
N^- ion	LUMO	-0.050065	-0.211202
	HOMO	-0.765704	-0.956509

according to the method we use to assure sp^3 bonding. Thus, the boron ion has six electrons and the nitrogen ion also has six electrons. In the LDA band structure results,[64] the top of the valence band is around -12 eV and the bottom of the conduction band lies at about -7 eV. Because the top of the valence band is primarily of nitrogen character, it is clear from the result for the embedded and unembedded nitrogen atom that the embedding potential is pushing the eigenvalue of the highest occupied level to the right vicinity. In the case of the boron atom, the highest occupied level is of 2*p* character and should be elevated by embedding so as to contribute to the conduction band in the crystal. Indeed, the embedded boron atom highest occupied level is substantially pushed up. In contrast to the results of embedding the atoms are the results of embedding the ions. The shifts in eigenvalues are in the same direction as those in the atoms. However, since the systems are now charged, the shifts do not bring the values of the highest occupied and lowest unoccupied levels into close proximity to the crystalline levels. This is true for all of the clusters shown in Table

IX as well. Therefore, embedding the clusters composed of ions with four valence electrons can actually worsen the electronic structure.

Another option is to occupy the clusters with the number of electrons of the atoms and do the embedding. However, this leads to a major problem because the assurance of proper tetrahedral bonding is not preserved. For example, a calculation of $B_{13}N_{16}H_{36}$ with a total of 213 electrons assigned to it leads to the highest occupied level being partially occupied. Therefore, the $B_{13}N_{16}H_{36}$ atomic cluster will distort its geometry to a structure different from that of the bulk. So it is clear that for cubic boron nitride clusters, the electron filling to meet the sp^3 bonding requirement is much more important than embedding. As a consequence we have elected to perform calculations to characterize the electronic structure of clusters of pure cubic boron nitride and clusters of doped cubic boron nitride without embedding.

A. Pure cubic boron nitride

Since we are interested in the electronic structure of *n*- and *p*-type substitutional defects in cubic boron nitride, we will first characterize the electronic structure of the pure cubic boron nitride cluster, $B_{13}N_{16}H_{36}$. Initially, a calculation of the electronic structure was performed at the bulk geometry. The point group symmetry of the bulk geometry of the cluster is T_d. Thus the eigenfunctions transform as one of the allowed irreducible representations a_1, a_2, e, t_1, or t_2. The highest occupied level corresponds to a completely full t_1 representation with an eigenvalue of -0.625202 a.u. The lowest unoccupied value corresponds to a t_1 representation with an eigenvalue of -0.331047 a.u. Subsequently, the cluster was allowed to relax to a geometry of lower total energy while constrained to T_d symmetry in order to see how far it would differ from the bulk geometry. The positions of the symmetry unique atoms are given in Table XI for both the bulk and the relaxed geometries. Note that only the

TABLE XI. Locations of the symmetry unique atoms for the relaxed and unrelaxed $B_{13}N_{16}H_{36}$ cluster. The number of atoms per shell is indicated in parentheses beside the type of atom occupying a shell.

geometry	shell	x (a.u.)	y (a.u)	z (a.u)
unrelaxed	B(1)	0.00000	0.00000	0.00000
	N(4)	1.70784	1.70784	1.70784
	B(12)	3.41568	0.00000	3.41568
	N(12)	1.70784	-1.70784	5.12352
	H(12)	-2.34290	2.34290	5.75860
	H(12)	0.63510	-4.05080	-4.05080
	H(12)	5.76400	1.06700	-1.06700
relaxed	B(1)	0.00000	0.00000	0.00000
	N(4)	1.680906	1.680906	1.680906
	B(12)	3.41568	0.00000	3.41568
	N(12)	1.70784	-1.70784	5.12352
	H(12)	-2.34290	2.34290	5.75860
	H(12)	0.63510	-4.05080	-4.05080
	H(12)	5.76400	1.06700	-1.06700

nearest neighbors to the center atom were allowed to move because all the other shells are bonded to hydrogens. When the cluster is allowed to relax, the nearest neighbors move inward by only about 1.6% of the bulk bond distance (0.7% of the lattice constant for cubic boron nitride). At the relaxed geometry, the highest occupied level is a completely full t_1 representation with an eigenvalue of -0.627265 a.u. The lowest unoccupied is a t_1 state at -0.331135 a.u. Thus, the band-gap of the relaxed cluster is nearly the same as the unrelaxed cluster, 8.05 eV vs. 8.00 eV. Fig. 15 shows the geometry of the relaxed $B_{13}N_{16}H_{36}$ cluster. Fig. 16 shows the density of states for the relaxed and unrelaxed $B_{13}N_{16}H_{36}$ cluster. As can be seen in the figure there is very little change in the electronic structure of the band gap when the cluster is

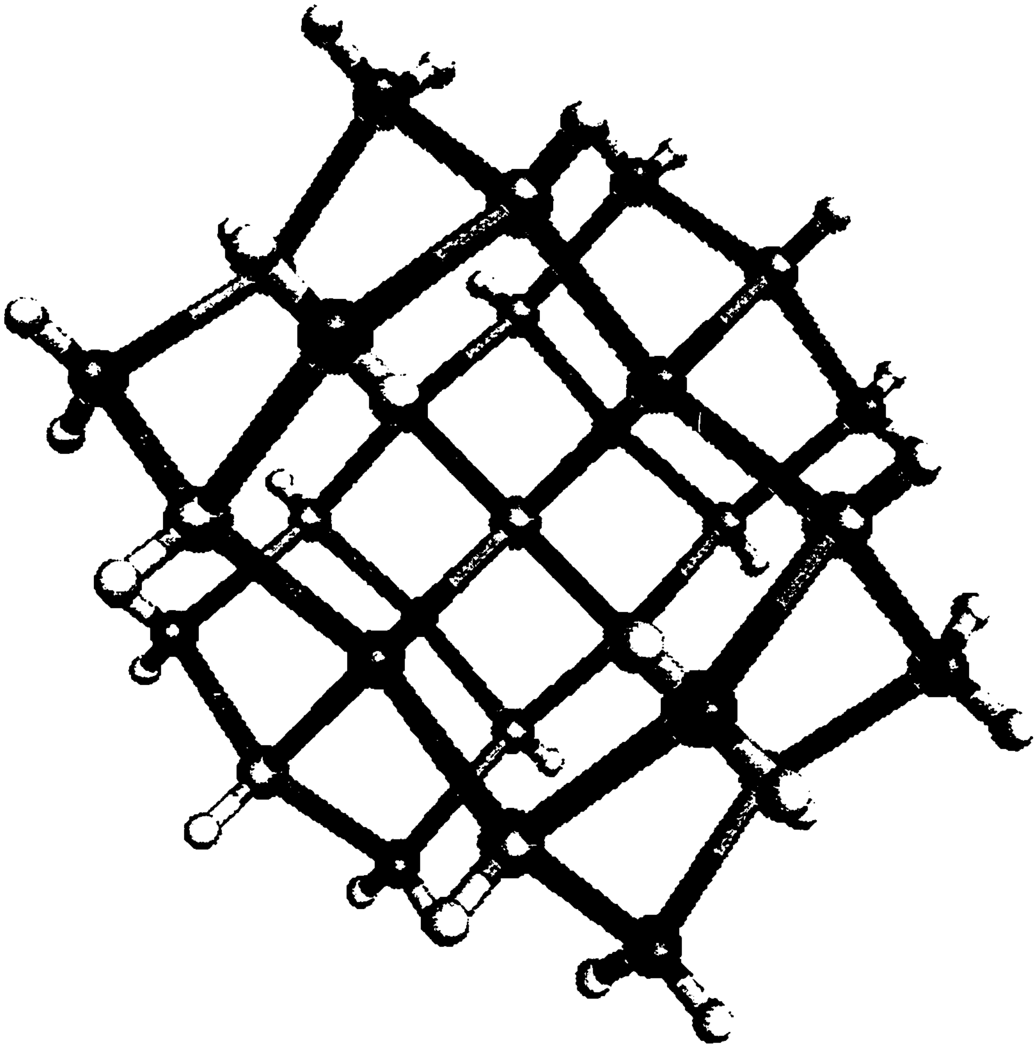

FIG. 15. Geometry of the relaxed $B_{13}N_{16}H_{36}$ cluster. The borons are shown in grey. The nitrogens are dark and the hydrogens are white.

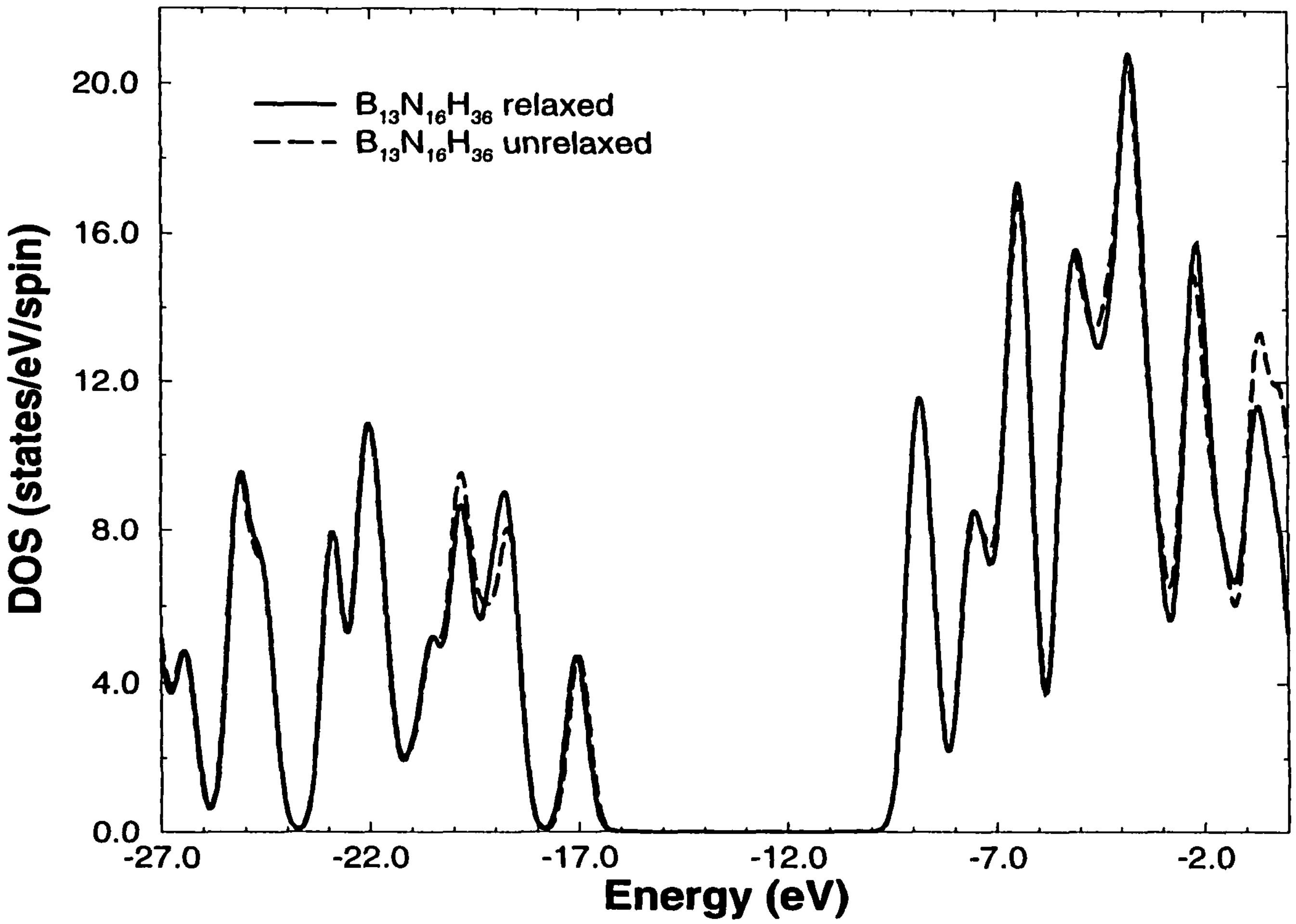

FIG. 16. Density of states of 29-atom pure boron nitride cluster within T_d symmetry.

allowed to relax. Fig. 17 shows total density contours for a plane intersecting the center boron atom and two of its nearest neighbor nitrogens.

B. Beryllium substitutional

To study a prototypical *p*-type dopant in cubic boron nitride, beryllium was substituted for boron at the center of the cluster to form $BeB_{12}N_{16}H_{36}$. Following the pattern used for boron in which six electrons were assigned to it for electron filling, beryllium is assigned five electrons. At the bulk geometry the beryllium produced a partially occupied t_1 acceptor level in the band gap. The spin up t_1 state is fully occupied and has an eigenvalue of -0.599185 a.u. The spin down t_1 state is occupied by two electrons and is at -0.590432 a.u. Thus the partially occupied t_1 spin down state is 0.238 eV from the fully occupied t_1 spin up state. The partially occupied t_1 spin down state is 0.946 eV from the highest occupied level in the pure cluster at the bulk geometry. Next the cluster was allowed to relax while constrained to T_d symmetry. The positions of the symmetry unique atoms are given in Table XII for both the unrelaxed and the relaxed clusters. In the relaxed cluster the nearest-neighbor nitrogen shell relaxed outward from the bulk geometry by 5.2% of the bond distance (2.2% of the lattice constant for cubic boron nitride). The relaxation outward of the nearest neighbors compared to that of the relaxed pure cubic boron nitride cluster is about 6.8% of the bond distance. At the relaxed geometry the beryllium produced a partially occupied t_1 level in the band gap. The spin up t_1 state is fully occupied and has an eigenvalue of -0.591440 a.u. The spin down t_1 state is occupied by two electrons and is at -0.582751 a.u. Thus, the partially occupied t_1 spin down state is 0.236 eV from the fully occupied t_1 spin up state and is 1.211 eV from the highest occupied level in the relaxed pure cubic boron nitride cluster.

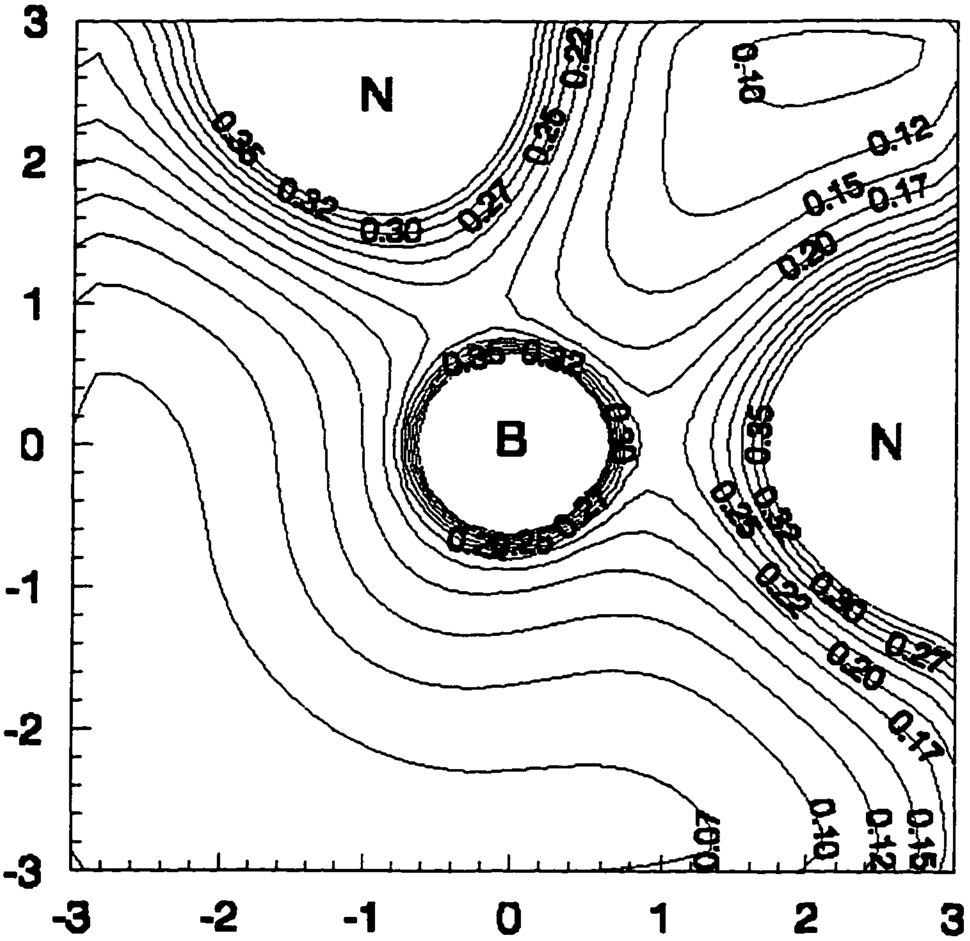

FIG. 17. Total density of $B_{13}N_{16}H_{36}$. The plane shown contains the central boron and two nearest neighbor nitrogens. Contours are in electrons/bohrs^3.

TABLE XII. Locations of the symmetry unique atoms for the unrelaxed and relaxed $BeB_{12}N_{16}H_{36}$ cluster. The number of atoms per shell is indicated in parentheses beside the type of atom occupying a shell.

geometry	shell	x (a.u.)	y (a.u.)	z (a.u.)
unrelaxed	Be(1)	0.00000	0.00000	0.00000
	N(4)	1.70784	1.70784	1.70784
	B(12)	3.41568	0.00000	3.41568
	N(12)	1.70784	-1.70784	5.12352
	H(12)	-2.34290	2.34290	5.75860
	H(12)	0.63510	-4.05080	-4.05080
	H(12)	5.76400	1.06700	-1.06700
relaxed	Be(1)	0.00000	0.00000	0.00000
	N(4)	1.795952	1.795952	1.795952
	B(12)	3.41568	0.00000	3.41568
	N(12)	1.70784	-1.70784	5.12352
	H(12)	-2.34290	2.34290	5.75860
	H(12)	0.63510	-4.05080	-4.05080
	H(12)	5.76400	1.06700	-1.06700

In Fig. 18, the density of states is plotted for the unrelaxed geometry of $BeB_{12}N_{16}H_{36}$. In Fig. 19, the density of states is plotted for the relaxed geometry of $BeB_{12}N_{16}H_{36}$. Overall, there is almost no change in the density of states when allowing the cluster to relax in T_d symmetry. Fig. 20 shows the geometry of the relaxed cluster. Fig. 21 shows total density contours for a plane intersecting the center beryllium atom and two of its nearest neighbor nitrogens.

A system in a degenerate state could lower its energy by distorting so as to split the degeneracy and then occupy the lower state (or states) whose total energy is lower. That such a phenomena would be expected to occur was pointed out by Jahn and Teller.[67] The basic point of the Jahn-Teller theorem is that in any assumed

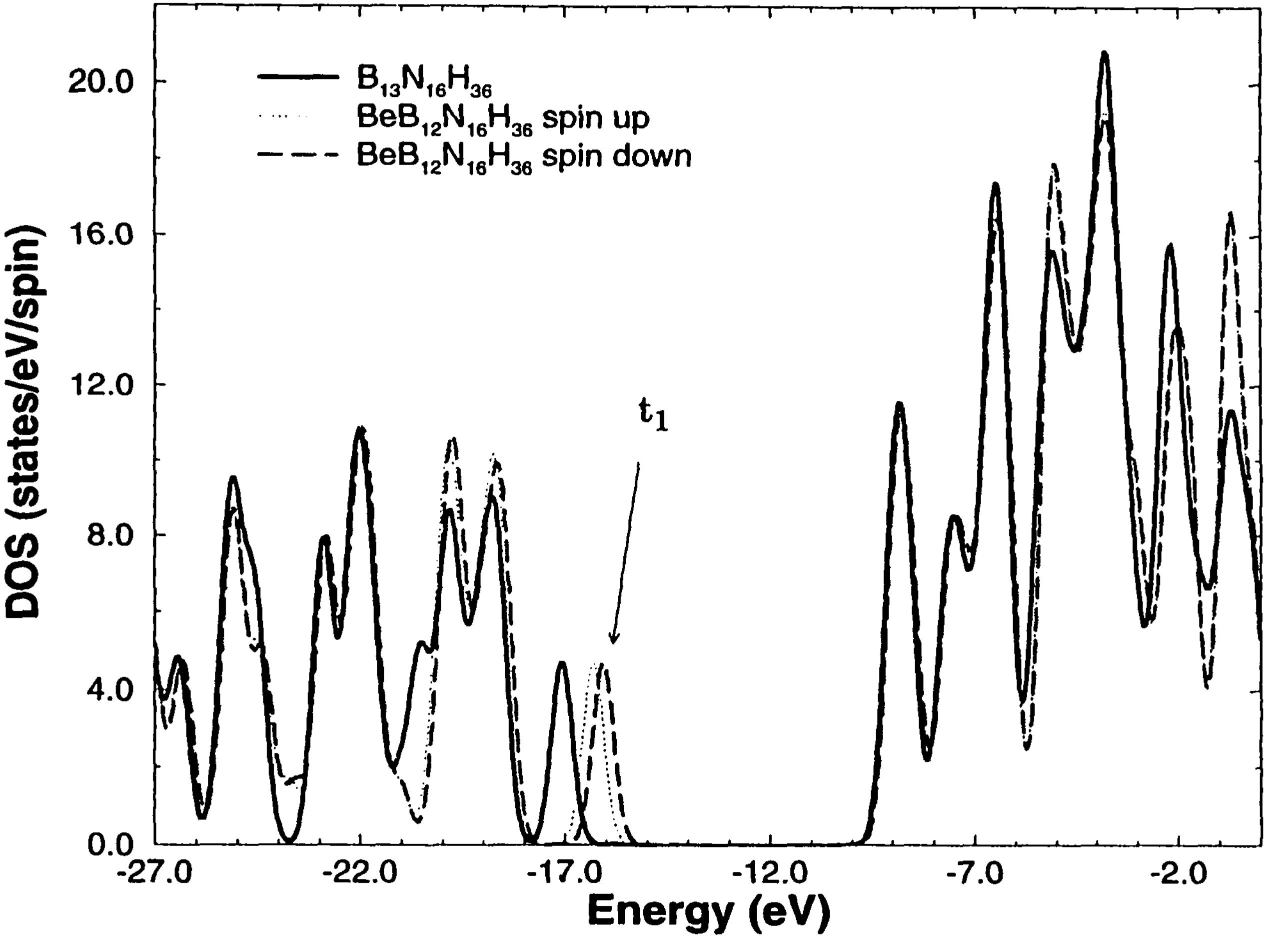

FIG. 18. The density of states for the 29-atom beryllium doped cubic boron nitride cluster within T_d symmetry at the bulk geometry.

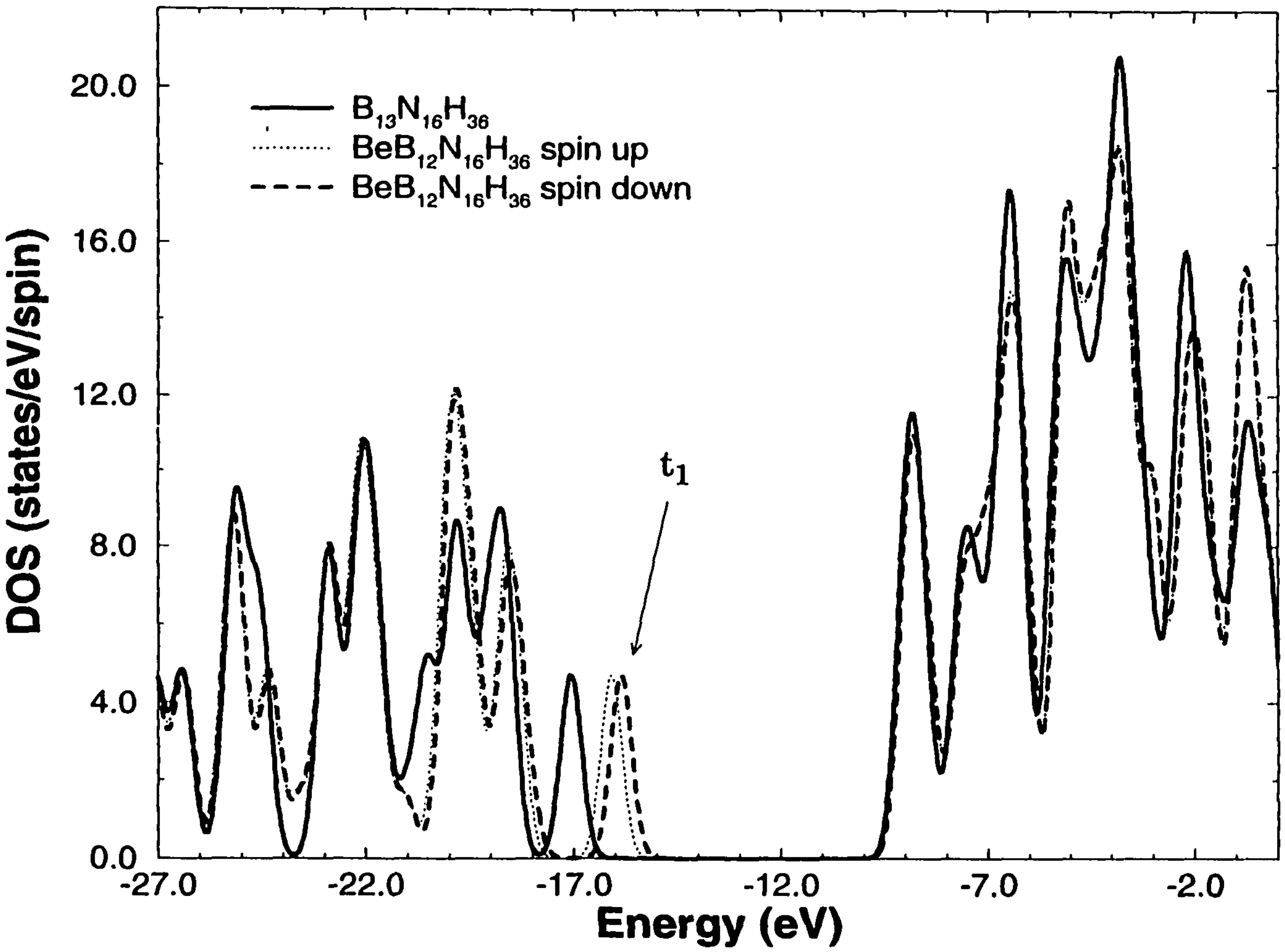

FIG. 19. The density of states for the 29-atom beryllium doped cubic boron nitride cluster within T_d symmetry at the relaxed geometry.

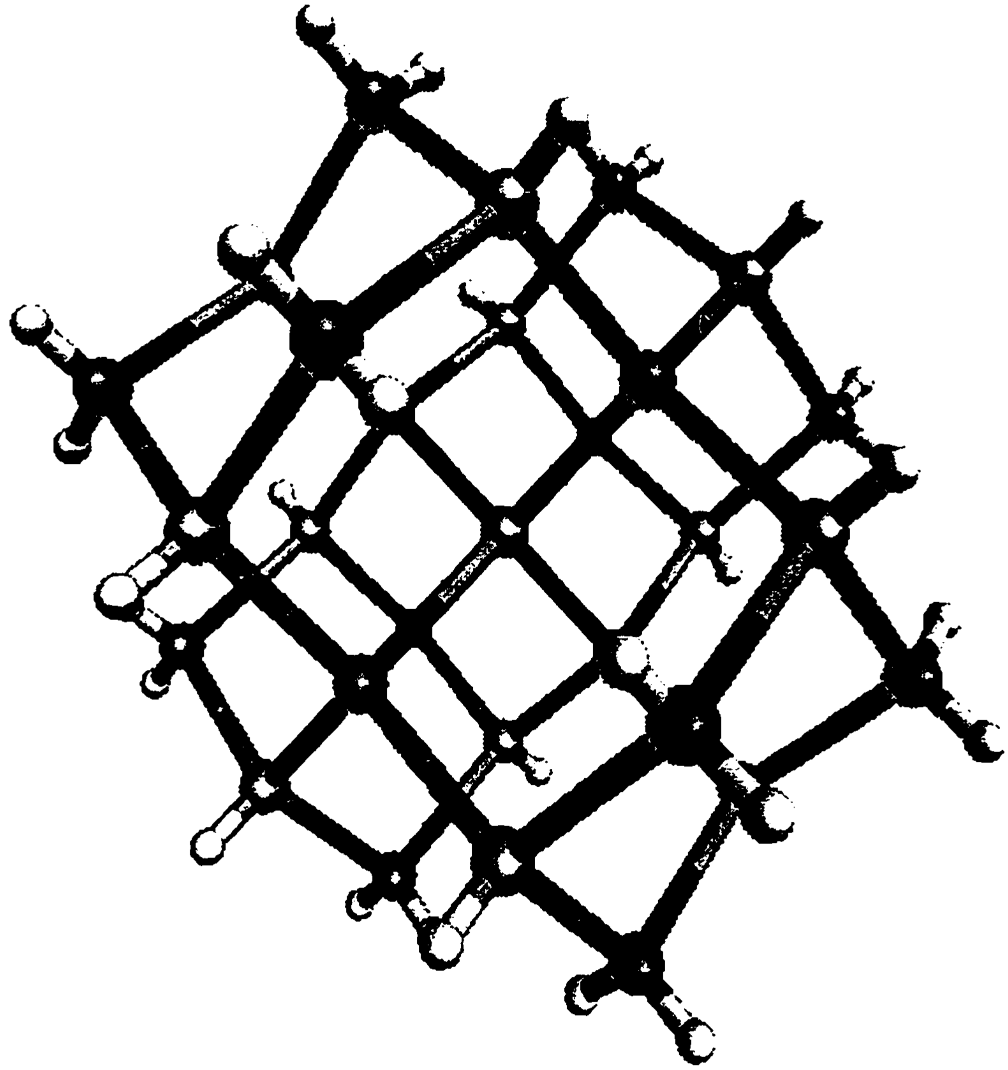

FIG. 20. The geometry of the relaxed $BeB_{12}N_{16}H_{36}$ cluster. The borons are shown in gray. The nitrogens are black and the hydrogens are white. Beryllium is the gray atom at the center of the cluster.

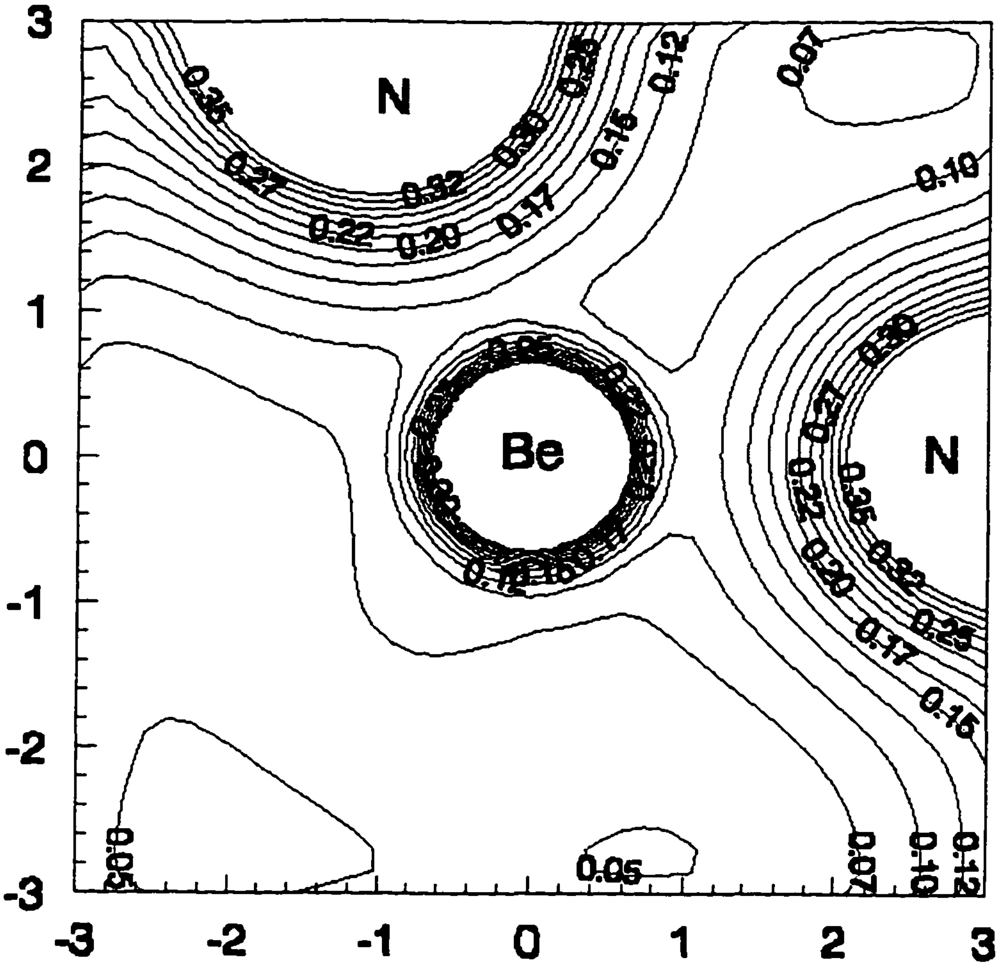

FIG. 21. Total density of Be $B_{12}N_{16}H_{36}$. The plane shown contains the central beryllium and two nearest neighbor nitrogens. Contours units are in electrons/bohrs^3.

equilibrium configuration, the energy will be a minimum with respect to small displacements. If that system is in a degenerate electronic state and the system distorts by a small amount so as to split the degeneracy, and is able to occupy the lower state, the energy will decrease in proportion to the distortion. Since, in T_d symmetry, the highest occupied level of $BeB_{12}N_{16}H_{36}$ is a partially occupied degenerate t_1 spin down state, $BeB_{12}N_{16}H_{36}$ will distort to a geometry of lower symmetry in which the degeneracy is lifted.

C. Silicon substitutional

To study a prototypical *n*-type dopant in cubic boron nitride, silicon was substituted for boron at the center of the cluster to form $SiB_{12}N_{16}H_{36}$. Following the pattern used for boron, silicon should have 15 electrons. At the bulk geometry the silicon produced a partially occupied t_1 donor level in the band gap. The spin up t_1 state is occupied by one electron and has an eigenvalue of -0.348921 a.u. The spin down t_1 state is unoccupied and is at -0.345454 a.u. Thus, the partially occupied t_1 spin up state is 0.094 eV from the unoccupied t_1 state and is 0.486 eV from the lowest unoccupied level in the pure cluster at the bulk geometry. Next the cluster was allowed to relax while constrained to T_d symmetry. The positions of the symmetry unique atoms are given in Table XIII for both the bulk and the relaxed clusters. In the relaxed cluster the nearest neighbor nitrogen shell relaxed outward from the bulk geometry by 7.0% of the bond distance (3.0% of the lattice constant for cubic boron nitride). The relaxation outward of the nearest neighbors compared to that of the relaxed pure cubic boron nitride cluster is about 8.7% of the bond distance. At the relaxed geometry, the silicon produced a partially occupied t_1 level in the band gap. The spin up t_1 state is occupied by one electron and has an eigenvalue of -0.351289 a.u. The spin

TABLE XIII. Locations of the symmetry unique atoms for the unrelaxed and relaxed $SiB_{12}N_{16}H_{36}$ cluster. The number of atoms per shell is indicated in parentheses beside the type of atom occupying a shell.

geometry	shell	x (a.u.)	y (a.u.)	z (a.u.)
unrelaxed	Si(1)	0.00000	0.00000	0.00000
	N(4)	1.70784	1.70784	1.70784
	B(12)	3.41568	0.00000	3.41568
	N(12)	1.70784	-1.70784	5.12352
	H(12)	-2.34290	2.34290	5.75860
	H(12)	0.63510	-4.05080	-4.05080
	H(12)	5.76400	1.06700	-1.06700
relaxed	Si(1)	0.00000	0.00000	0.00000
	N(4)	1.827721	1.827721	1.827721
	B(12)	3.41568	0.00000	3.41568
	N(12)	1.70784	-1.70784	5.12352
	H(12)	-2.34290	2.34290	5.75860
	H(12)	0.63510	-4.05080	-4.05080
	H(12)	5.76400	1.06700	-1.06700

down t_1 state is unoccupied and is at -0.347013 a.u. Thus, the partially occupied triplet t_1 spin up state is 0.116 eV from the unoccupied t_1 spin down state and 0.548 eV from the lowest unoccupied level of the relaxed pure cubic boron nitride cluster.

In Fig. 22, the density of states is plotted for the bulk geometry of $SiB_{12}N_{16}H_{36}$. In Fig. 23, the density of states is plotted for the relaxed geometry of $SiB_{12}N_{16}H_{36}$. As was the case for the beryllium substitutional, silicon also shows almost no change in the density of states when allowing the cluster to relax in T_d symmetry. Fig. 24 shows the geometry of the relaxed cluster. Fig. 25 shows total density contours for a plane intersecting the center silicon atom and two of its nearest neighbor nitrogens.

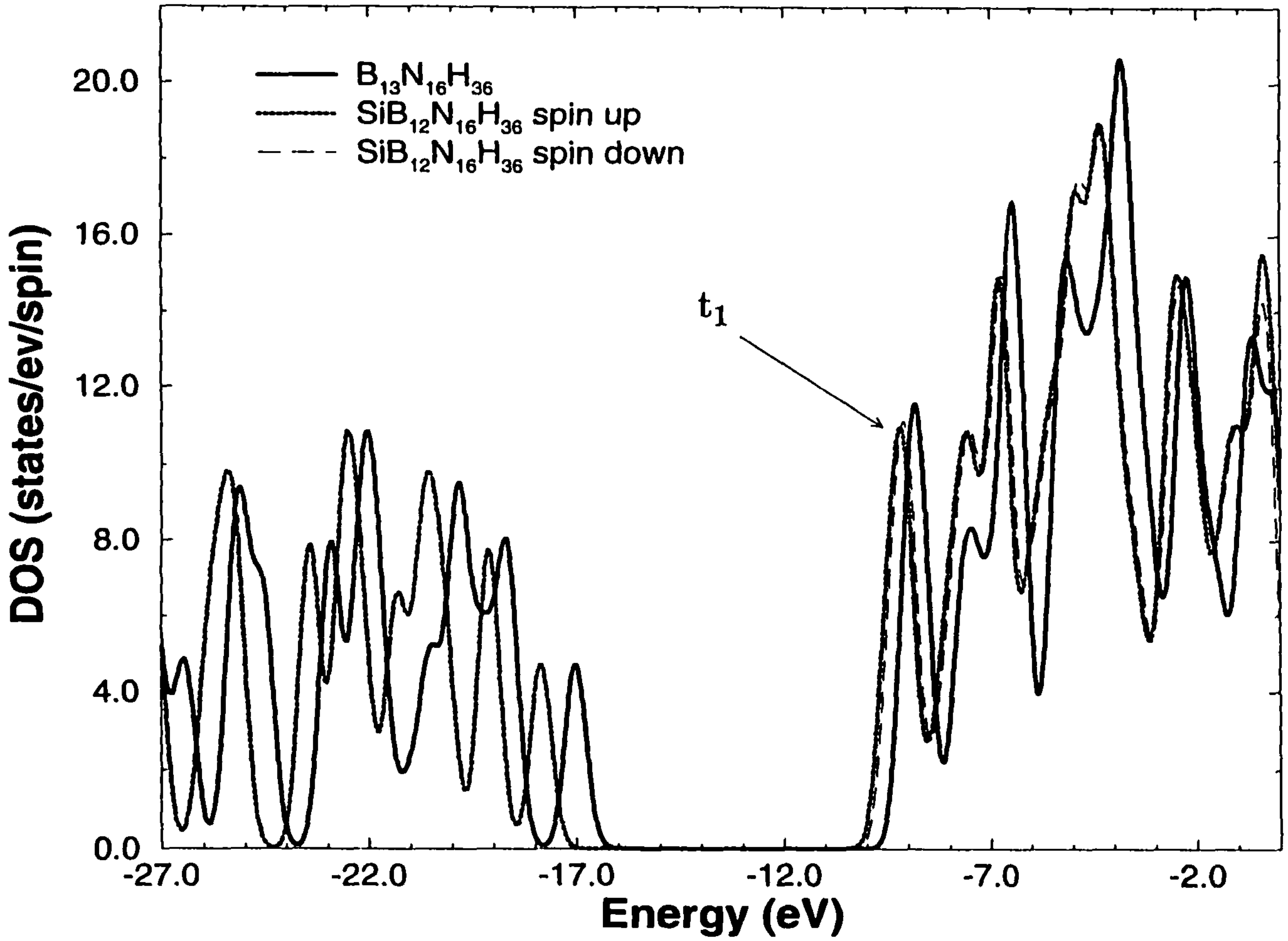

FIG. 22. The density of states for the 29-atom silicon doped cubic boron nitride cluster within T_d symmetry at the bulk geometry.

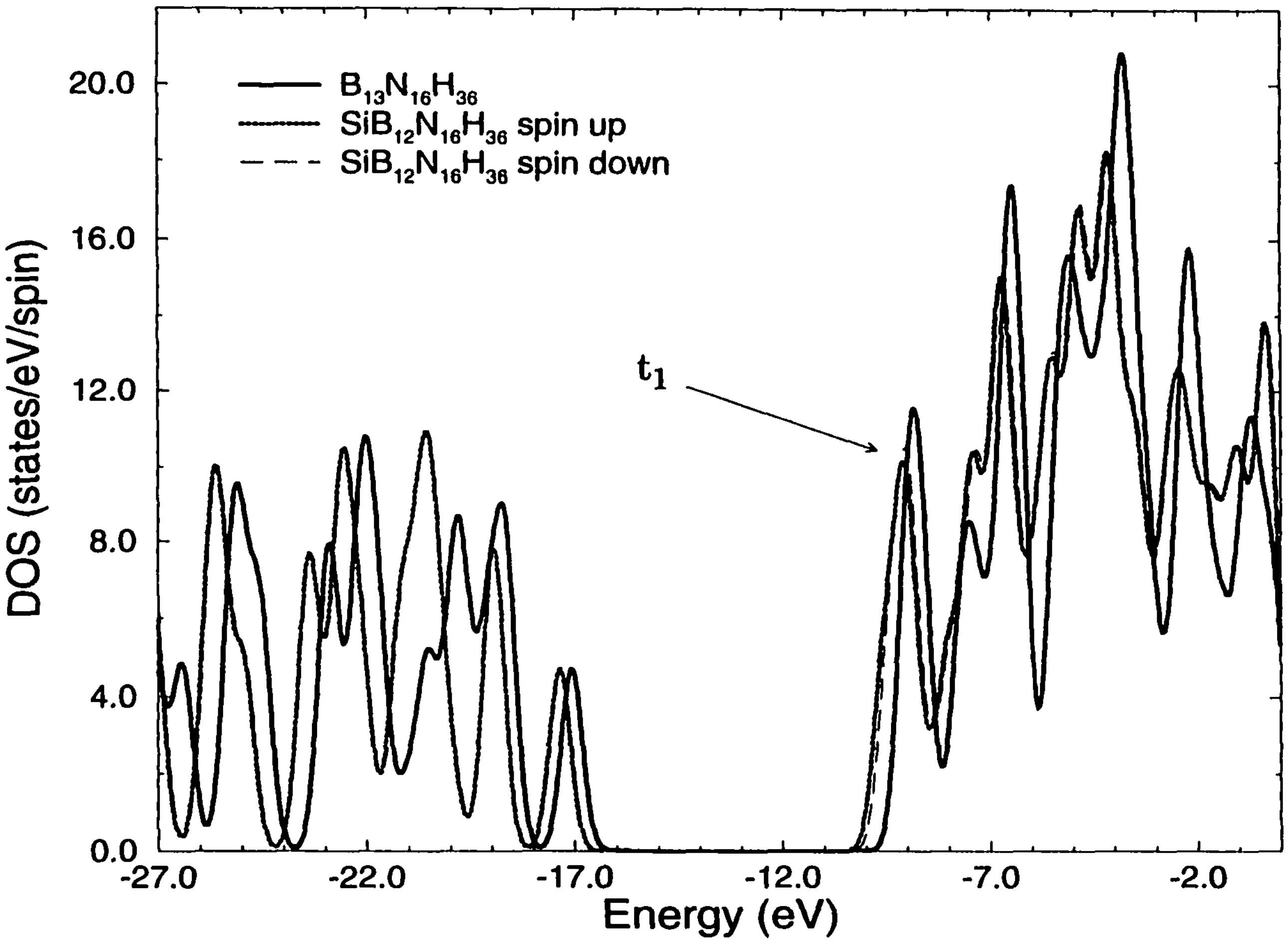

FIG. 23. The density of states for the 29-atom silicon doped cubic boron nitride cluster within T_d symmetry at the relaxed geometry.

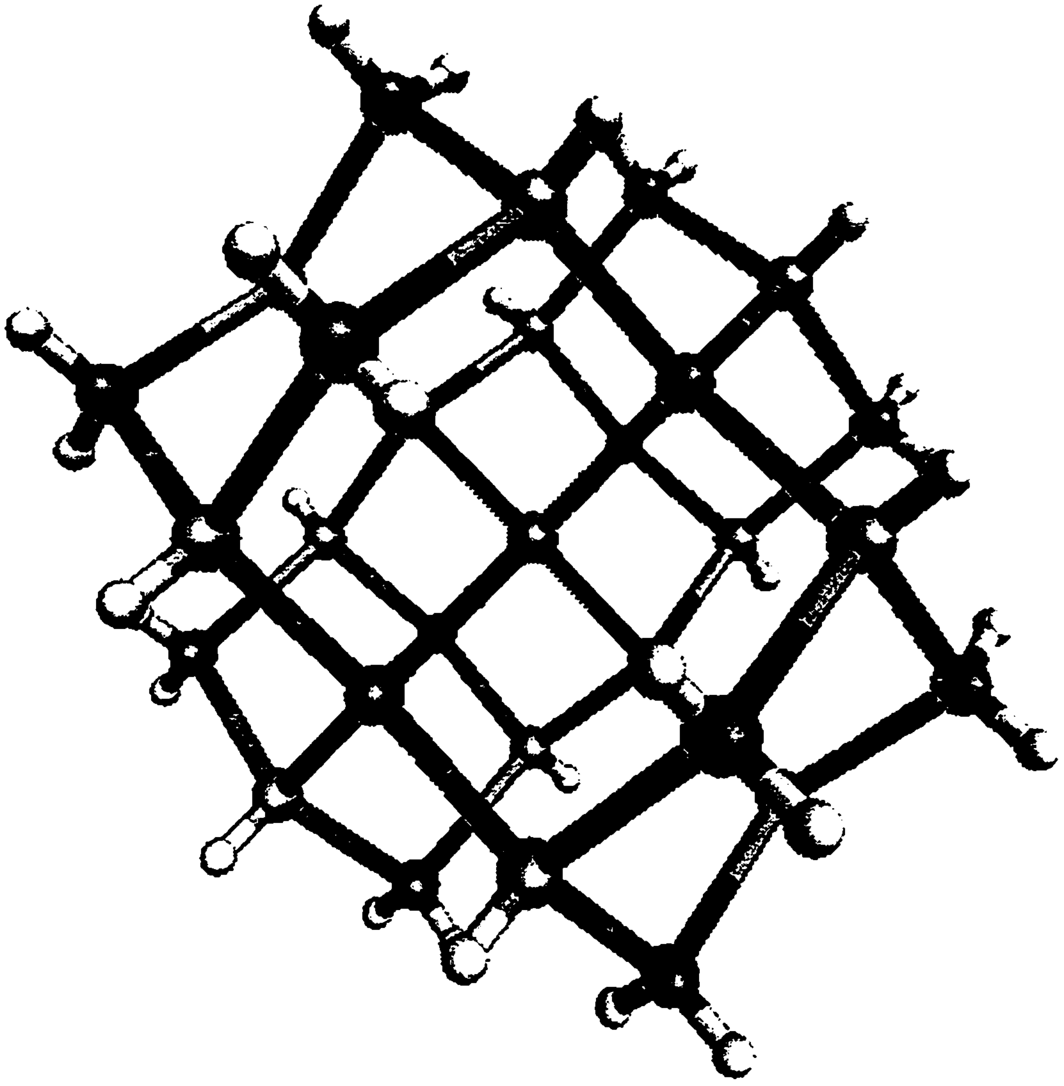

FIG. 24. The geometry of the relaxed $SiB_{12}N_{16}H_{36}$ cluster. The borons are shown in gray. The nitrogens are black and the hydrogens are white. Silicon is the dark gray atom at the center of the cluster.

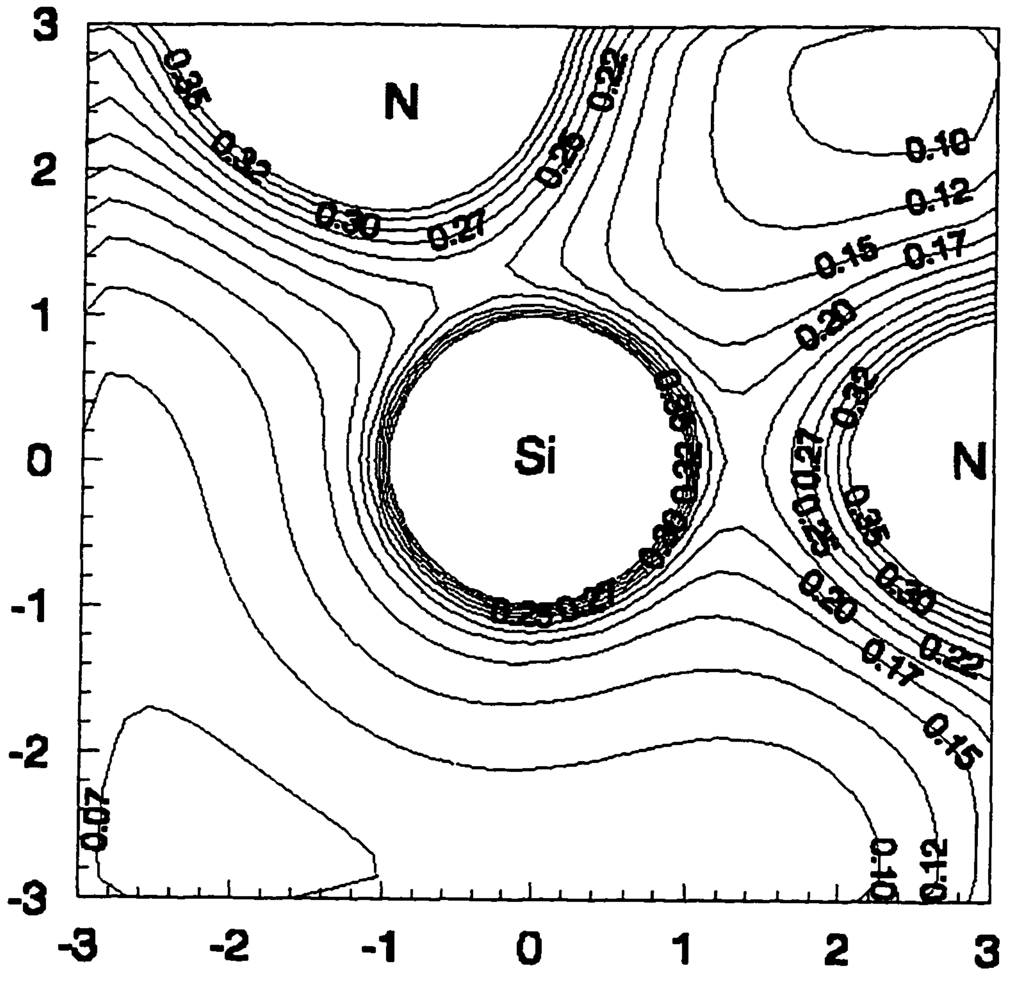

FIG. 25. Total density of Si $B_{12}N_{16}H_{36}$. The plane shown contains the central silicon and two nearest neighbor nitrogens. Contours units are in electrons/bohrs^3.

In T_d symmetry the highest occupied level was a partially occupied degenerate level. Thus, as was the situation with the beryllium substitutional, the silicon substitutional is expected to induced a lattice distortion to a geometry of lower symmetry, which will remove the degeneracy.

CHAPTER V

VIBRATIONAL AND OPTICAL SPECTRA

In this chapter we discuss calculations of properties that can be experimentally investigated. There are a vast number of experiments that can be performed to characterize defects in solids. Very little work has been done on defects in cubic boron nitride. We have chosen to study four properties that may help to correlate our predictions of the electronic structure with experiment. The Fermi contact interaction terms, vibrational spectra, oscillator strengths, and photoemission spectra are considered.

A. Fermi contact terms

In a cluster the ground state density has a nonzero value at the nucleus, and this density is essentially constant throughout the small volume of the nucleus. Hence, the nucleus is in a uniformly magnetized medium with magnetization

$$M = -g_e \beta |\psi(0)|^2 s \ . \tag{5.1}$$

The electronic magnetic dipole moment operator is $\hat{\mu} = -g_e \beta s$. The nuclear magnetic moment operator is $\hat{\mu}_n = g_n \beta_n I$. The energy of a nuclear magnetic dipole in the field resulting from M is given by the Fermi contact interaction term:

$$\mathrm{H} = \frac{-8\pi}{3} M \bullet \hat{\mu}_n = \frac{8\pi}{3} g_e \beta g_n \beta_n |\psi(0)|^2 \mathrm{I} \bullet s \tag{5.2}$$

This Fermi contact term is characterized in cluster calculations as the difference in the majority and minority spin populations at the nucleus, *i.e.* the net magnitization. Thus, in order to produce a large Fermi contact term, there must be an unpaired spin density associated with that particular nucleus. In pure cubic boron nitride, there is no unpaired spin density and so no hyperfine structure is seen in the EPR data.[68]

In cubic boron nitride there is expected to be an unpaired spin density associated with *p*- and *n*-type dopants. Thus, in experimental studies of pure cubic boron nitride systems and doped cubic boron nitride systems, there will be very different spectrums. The difference, in part, will be associated with a Fermi contact term from the dopants. The expression for the Fermi contact term involves individual electronic orbitals and spin angular momenta. Hence, it gives a measure of how delocalized the electronic state is and can be used together with EPR studies to unravel some of the local symmetry of the defect environment. We know of no EPR studies of beryllium or silicon substitutional dopants in cubic boron nitride.

In Table XIV the spin densities at the nuclei are given for the symmetry unique atoms in the unrelaxed and relaxed clusters of $BeB_{12}N_{16}H_{36}$ with T_d symmetry. This leads to the Fermi contact terms listed in Table XV. There is very little dependence on cluster relaxation on the Fermi contact terms when the cluster is constrained to T_d symmetry. Table XVI lists the spin densities at the nuclei for the symmetry unique atoms in the unrelaxed and relaxed clusters of $SiB_{12}N_{16}H_{36}$ with T_d symmetry. This leads to the Fermi contact terms listed in Table XVII. From Table XVI it is apparent that there is significant decrease in the density at the silicon nucleus when the cluster is allowed to relax. Because of a larger decrease in the spin down density the Fermi contact term for the silicon site is enhanced in the relaxed cluster.

TABLE XIV. The spin densities at the nuclei of the symmetry unique atoms for the $BeB_{12}N_{16}H_{36}$ cluster. Majority (spin up), minority (spin down), and total spin densities are given.

cluster	shell	spin up	spin down	total density
unrelaxed	Be(1)	16.66541	16.67584	33.34125
	N(4)	97.34877	97.31780	194.6666
	B(12)	97.83302	97.83272	195.6657
	N(12)	33.91701	33.91496	67.83197
relaxed	Be(1)	16.63170	16.64207	33.27377
	N(4)	97.32101	97.29655	194.6176
	B(12)	97.83321	97.83205	195.6653
	N(12)	33.90973	33.90666	67.81638

TABLE XV. Fermi contact terms for the symmetry unique atoms in the $BeB_{12}N_{16}H_{36}$ cluster. The number of atoms per shell is listed beside the type of atom composing a particular shell.

		Fermi Contact Terms	
cluster	shell	spin/bohrs^3	x 10^{20} spin/cm^3
unrelaxed	Be(1)	0.01043	0.338
	N(4)	0.03097	1.003
	B(12)	0.00040	0.013
	N(12)	0.00205	0.066
relaxed	Be(1)	0.01037	0.336
	N(4)	0.02446	0.793
	B(12)	0.00116	0.038
	N(12)	0.00307	0.099

B. Vibrational spectra

Detailed analysis of vibrational modes in the clusters gives complementary information regarding the defect symmetry and elastic coupling to the host crystal. The interatomic forces of the cluster determine the vibrational spectrum, which may

TABLE XVI. The spin densities at the nuclei of the symmetry unique atoms for the $SiB_{12}N_{16}H_{36}$ cluster. Majority (spin up), minority (spin down), and total spin densities are given.

cluster	shell	spin up	spin down	total density
unrelaxed	Si(1)	845.4542	845.4470	1690.901
	N(4)	97.40365	97.33717	194.7408
	B(12)	97.86950	97.82097	195.6905
	N(12)	33.91136	33.91089	67.82226
relaxed	Si(1)	845.3029	845.2857	1690.589
	N(4)	97.39256	97.31692	194.7095
	B(12)	97.86396	97.81955	195.6835
	N(12)	33.90228	33.90031	67.80259

TABLE XVII. Fermi contact terms for the symmetry unique atoms in the $SiB_{12}N_{16}H_{36}$ cluster. The number of atoms per shell is listed beside the type of atom composing a particular shell.

		Fermi Contact Terms	
cluster	shell	spin/bohrs^3	x 10^{20} spin/cm^3
unrelaxed	Si(1)	0.00720	0.233
	N(4)	0.06648	2.154
	B(12)	0.04853	1.572
	N(12)	0.00047	0.052
relaxed	Si(1)	0.01720	0.557
	N(4)	0.07564	2.451
	B(12)	0.04441	1.439
	N(12)	0.00197	0.064

be probed by infrared, Raman, and other experimental techniques. With a large cluster the coupling between intra- and inter-cluster motions is relatively weak so what is discovered for the cluster should be approximately valid for the crystal for at least some of the modes.

The vibrational frequencies of pure cubic boron nitride have been experimentally measured by Chrenko[69] and by Gielisse *et al.*[70] via infrared absorption studies. Their observed peaks and assignments of the peaks to certain vibrational modes is listed in Table XVIII. Discrepancies in the values were attributed by Chrenko as being a result of the smaller crystals used by Gielisse *et al.* The zone-center TO phonon frequency has been calculated to be at 1063 cm^{-1} by Fahy.[71]

We have calculated the vibrational frequencies of the $B_{13}N_{16}H_{36}$ relaxed cluster with the MOPAC6 package. The calculation was performed with both the MNDO and AM1 parametrization of the Hamiltonian. The calculation was done at the geometry predicted by the LCAO cluster codes. All translational and rotational modes of the cluster are excluded from our results. Both parametrizations produce very similar spectra with the same number of peaks. There is a slight shift of the higher frequency peaks downward in the AM1 calculation. Fig. 26 shows the calculated spectrum of the vibrational density of states. The vibrational density of states is derived by weighting the spectra of vibrational frequencies with the vibrational transition dipole moments. None of the high frequency ($>1500cm^{-1}$) peaks seen in the experimental spectra are reproduced by the calculations. As was suggested by Chrenko, the experimental peaks are probably the result of defects or off-stoichiometry in their crystals. In fact the crystal displaying all of the higher peaks was described as the thick yellow sample. The thin colorless sample studied by Chrenko failed to reproduce most of the high frequency peaks.

When beryllium is substituted for the center boron atom, the cluster relaxes as was discussed in Chapter IV. The vibrational spectrum of $BeB_{12}N_{16}H_{36}$ is shown in Fig. 27. The spectrum for the beryllium doped cluster is quite different from that of

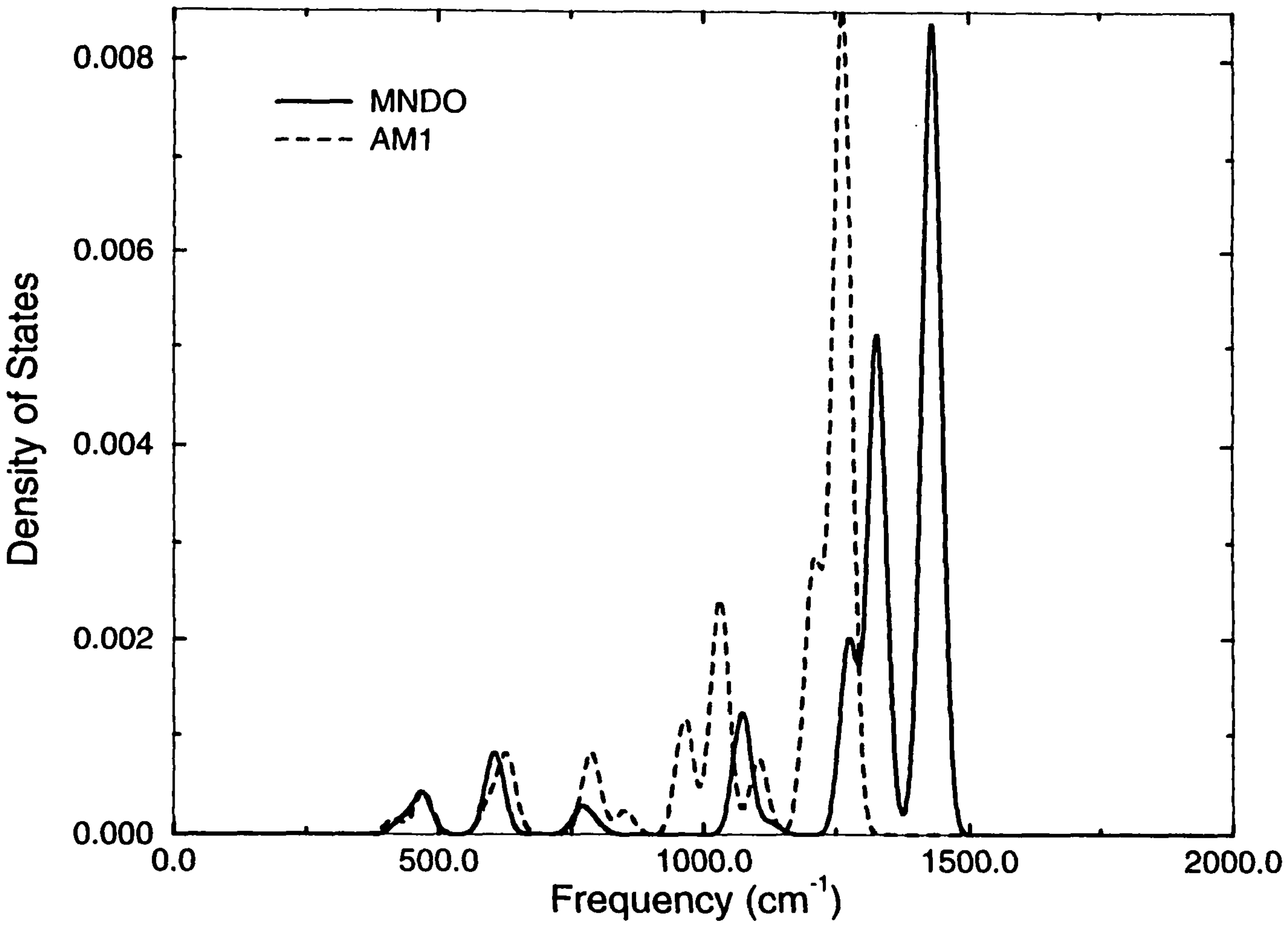

FIG. 26. Vibrational density of states for the $B_{13}N_{16}H_{36}$ cluster. Shown are the values obtained by using the MNDO and the AM1 parameterizations.

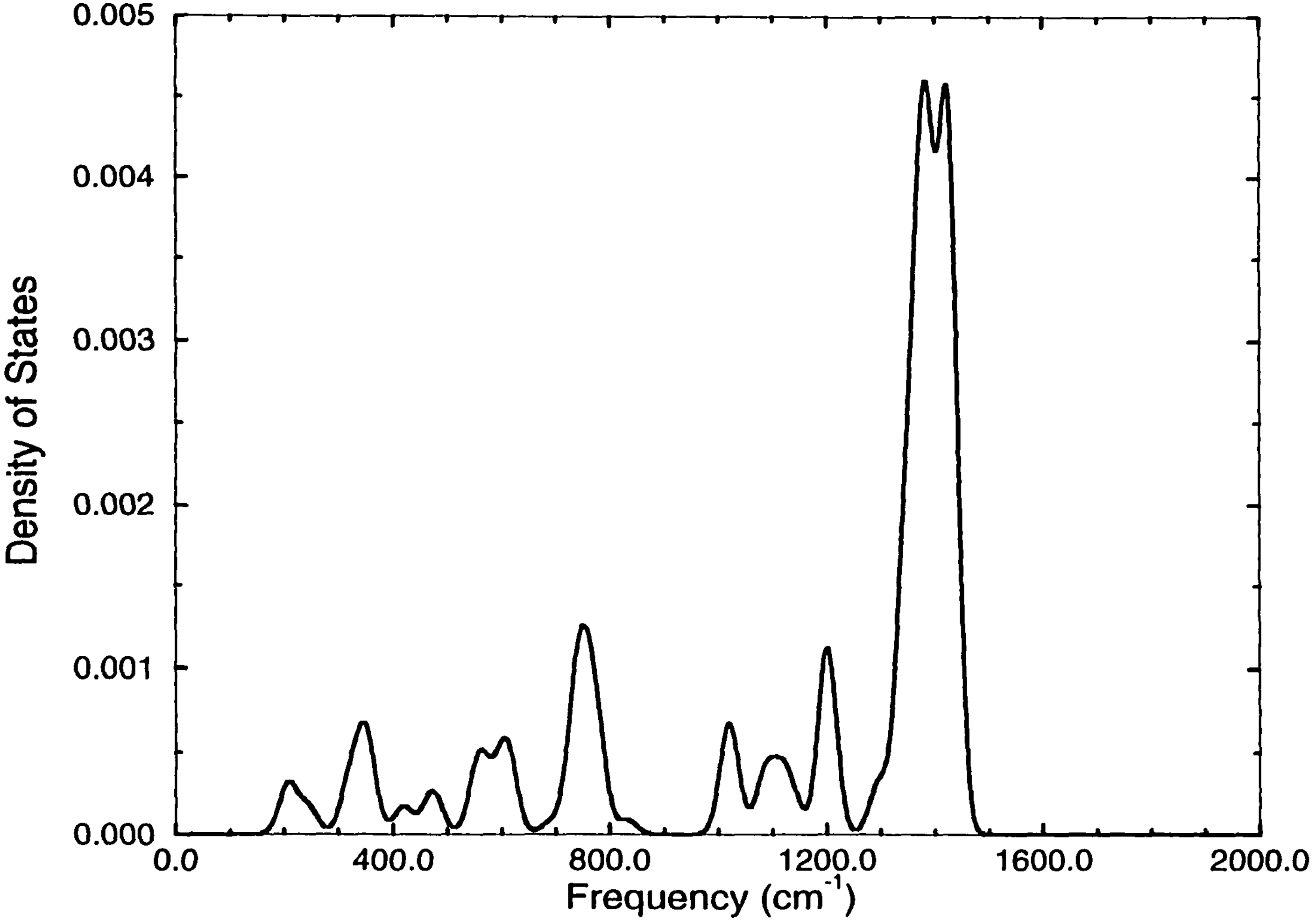

FIG. 27. The vibrational density of states for the $BeB_{12}N_{16}H_{36}$ cluster.

TABLE XVIII. The experimentally observed infrared absorption peaks (v_1 is Chrenko's value and v_2 is Gielisse's value) and their assignments by Gielisse with TO at 1000 cm^{-1} and LO at 1232 cm^{-1}.

$v_1(cm^{-1})$	$v_2(cm^{-1})$	assignment
-	650	TO-TA
-	700	2TA
1000-1300	1000-1260	Reststrahlen
-	1370	2LA
1550	1580	LO+TA
1700	-	-
1785	-	-
1818	1830	-
1840	-	-
1885	-	-
1927	1920	LO+LA
1985	2000	2TO
2140	-	-
-	2230	LO+TO
2330	-	-
-	2465	2LO
2560	-	-
-	2700	2TO+LA
2910	-	-

the pure cluster. In particular, there is a strong peak at about 750 cm^{-1} that was not evident in the pure cluster. (4.3)

When silicon is substituted for the center boron atom, the cluster relaxes as was discussed in Chapter IV. The vibrational spectrum of $SiB_{12}N_{16}H_{36}$ is shown in Fig. 28. The spectrum shown for the silicon doped cluster varies substantially from the spectra of the beryllium dopant and the pure cluster. As was the case with beryllium,

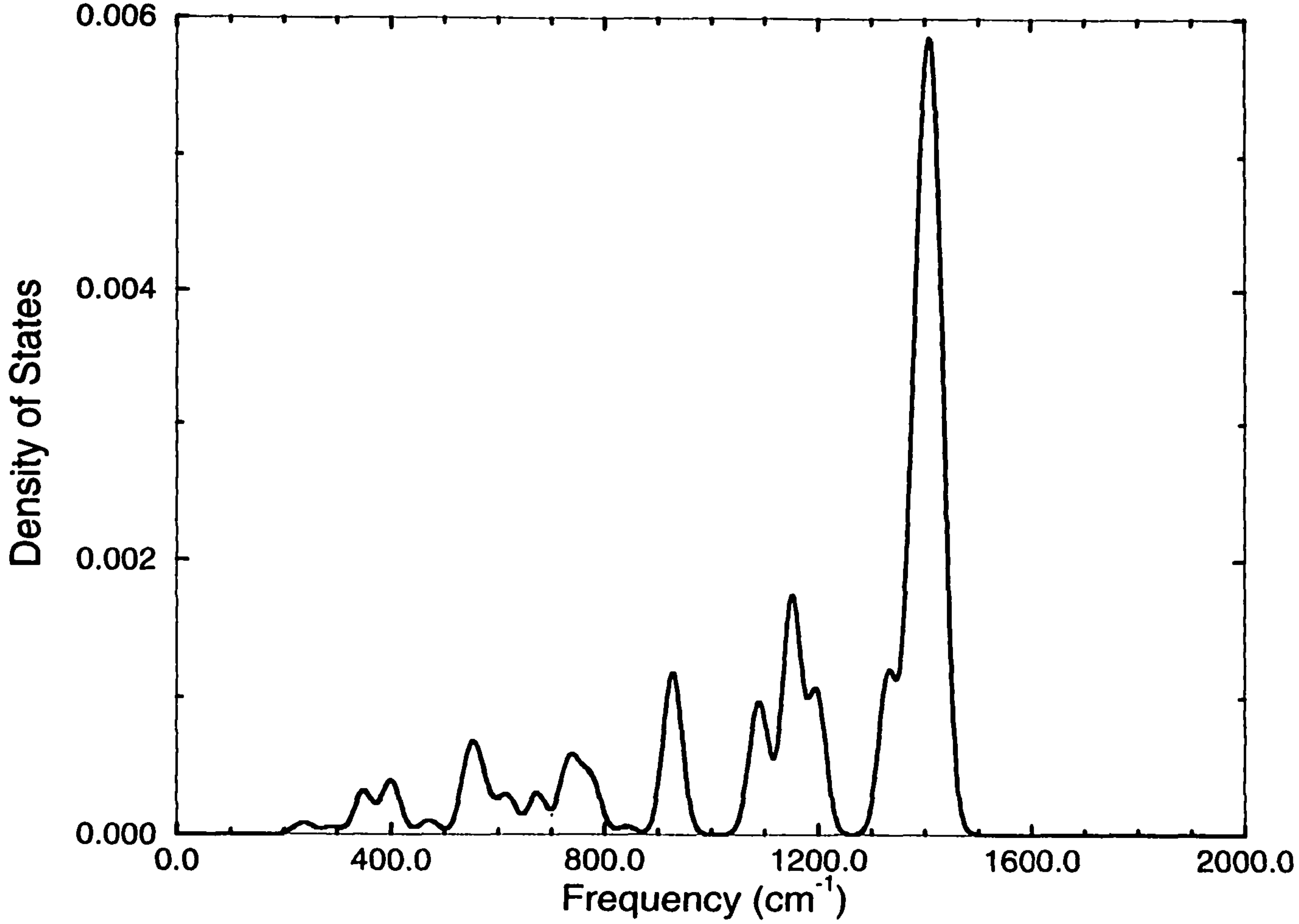

FIG. 28. The vibrational density of states for the $SiB_{12}N_{16}H_{36}$ cluster.

there is a particular peak which is directly related to the presence of the silicon. This peak is at about 910 cm^{-1}.

C. Oscillator strengths

Oscillator strength measurements often require some assumptions regarding the number and charge state of impurity centers. However, if calculations are available, the experimentalist may use the theoretical oscillator strength to deduce the defect densities. Thus, such calculations provide a useful optical characterization of the defect centers.

To predict the optical absorption spectrum seen for a particular material, the interaction of the system with electromagnetic radiation must be considered. A proper quantum-mechanical approach would treat both the atom and the radiation quantum mechanically, but things can be simplified without great loss of accuracy by considering light as an electromagnetic wave of oscillating electric and magnetic fields. The electric component playing the major part, a further simplification is achieved by just considering the electric part. Then the probability of absorption will be proportional to $|\langle\psi_m|\boldsymbol{d}|\psi_n\rangle|^2$ where $\boldsymbol{d}$ is the system's dipole-moment operator. The integral is the transition (dipole) moment d_{mn}. The dipole-moment operator has two forms: a length form where $\boldsymbol{d}=\mathbf{r}$, and a velocity or gradient form where $\boldsymbol{d}=\nabla$. Both the length form and the gradient form of the dipole-moment operator allow the oscillator strength to be characterized by its contributing components in the x, y, and z directions. When $d_{\mathrm{mn}}=0$, the transition between states m and n with absorption or emission of radiation is forbidden. Allowed transitions have $d_{mn}\neq 0$. Because of approximations made in the derivation of the transition probabilities, forbidden transitions may have some small probability of occuring.[72] At the present time there is no simple modification of our codes to explore vibronic effects on absorption levels. For the principal defects in these systems, it is expected that this will not present a serious limitation. The oscillator strength is given by[73]

$$f_{mn} = \frac{4\pi\omega_{mn}}{h}|d_{mn}|^2 \text{ with } \omega_{mn} = 2\pi\frac{E_m - E_n}{h} . \tag{5.4}$$

Since the orbitals given in the above expression for d_{mn} can be broken down in terms of their contributions from different shells, the dipole moment can give a measure of how much a shell is contributing to certain transitions.

$$|\psi_m\rangle = \sum_{\nu} A_{m\nu}\varphi_{\nu} \tag{5.5}$$

where the sum is over n shells with φ_ν being the basis at each shell. Then the oscillator strength can be written in terms of its contribution from different shells in the following manner:

$$f_{mn} = \sum_{\nu}\left[A_{m\nu}\sum_{\nu'}B_{n\nu'}\langle\varphi_\nu|\vec{d}|\varphi_{\nu'}\rangle\right] \equiv \sum_{\nu}(f_{mn})_{\nu} \tag{5.6}$$

This is similar to a Mulliken analysis of the charge density. When ν and ν' in Eq. (5.6) are the same the transitions take place on the same shell and are expected to have an atomic-like character.

For $BeB_{12}N_{16}H_{36}$ and $SiB_{12}N_{16}H_{36}$ we have calculated the oscillator strengths associated with transitions from the defect levels to the first few excited levels. In order to perform the oscillator strength calculations, we have utilized the ICON-EDiT package by Gion Calzaferri, Ruedi Rytz, and Martin Braendle at the Institute for Inorganic and Physical Chemistry in Berne, Switzerland. ICON-EDiT performs extended-Hueckel and oscillator strength calculations based on Slater-type extended -Hueckel wave functions. We have used the relaxed geometries from the LCAO cluster codes as input to ICON-EDiT. Table XIX contains the transition oscillator strengths for several of the smallest transitions in the doped clusters calculated with the length form of the dipole-moment operator. In Table XX, we have included the contributions to the total oscillator strength from on-shell and off-shell contributions

TABLE XIX. The transition oscillator strengths for the beryllium- and silicon-doped cubic boron nitride clusters. Contributions to the total oscillator strength are listed for the x, y, and z components of the dipole-moment operator.

dopant	transition (cm^{-1})	x	y	z	total
Be	7791.2	0.031308	0.031297	0.031288	0.054209
	9995.6	0.072723	0.072731	0.072732	0.125970
	15584.9	0.283069	0.283000	0.282992	0.490206
	18147.5	0.076067	0.076046	0.076063	0.131737
	18563.0	0.026314	0.026319	0.026334	0.045592
	19804.1	0.008251	0.008250	0.008263	0.014298
	20573.4	0.004433	0.004432	0.004430	0.007676
Si	4445.3	0.024993	0.024992	0.024993	0.043289
	6892.9	0.029686	0.029684	0.029690	0.051419
	15036.5	0.127612	0.127627	0.127632	0.221051
	-24469.0	0.206146	0.206131	0.206149	0.357048

as detailed in Eq. (5.6). There is a particularly large oscillator strength associated with the 15584.9 cm^{-1} transition in the beryllium-doped cluster. The major contribution to this level is from the on-shell part. Thus this strong oscillator strength is due to an atomic-like transition taking place at the beryllium site.

D. Photoemission spectra

X-ray (XPS) and ultraviolet (UPS) photelectron spectroscopy provide powerful experimental probes of the valence spectra of solids. Construction of theoretical XPS and UPS line shapes requires accurate ground state eigenvalues and the photoelectron cross sections. We perform the calculation of the spectra according to the formalism discussed by Mintmire *et al.* First-order, time-dependent perturbation theory and a semiclassical description of the radiation-matter interaction is utilized. The differential cross section for bound to free transitions from an initial state, u_i, to a final

TABLE XX. The transition oscillator strengths for the beryllium- and silicon-doped cubic boron nitride clusters. Contributions to the total oscillator strength are listed for the on-shell and off-shell components of the dipole-moment operator.

Dopant	Transition (cm^{-1})	On-Shell	Off-Shell	Total
Be	7791.2	0.053604	0.000605	0.054209
	9995.6	0.130011	-0.004041	0.125970
	15584.9	0.460607	0.029599	0.490206
	18147.5	0.135200	-0.003469	0.131737
	18563.0	0.032194	0.013398	0.045592
	19804.1	0.010736	0.003562	0.014298
	20573.4	0.005201	0.002475	0.007676
Si	4445.3	0.136296	-0.093007	0.043289
	6892.9	0.170836	-0.119417	0.051419
	15036.5	0.730050	-0.508999	0.221051
	24469.0	1.219463	-0.862415	0.357048

state, $u_f(r) = e^{-ik_f \bullet r}$, induced by incident radiation of energy ω and averaged over polarization and direction of incidence is

$$\frac{d}{d\Omega}\sigma_i(\omega) = F\frac{k_f}{\omega}(P_{if})^2 \qquad (5.7)$$

where F is an unspecified constant that can be taken as unity because only the line shape of the photoemission spectrum is of interest. The bound initial electronic state is simply the occupied Kohn-Sham orbital with energy ε_i. Note that the momentum of the outgoing plane wave is determined by total energy conservation. P_{if} is the transition matrix defined as

$$P_{if} = \int u_i(r)\,\nabla u_f(r)\,dr. \qquad (5.8)$$

The non-angular-resolved photoemission spectra is then obtained by integrating over the solid angles of dΩ to obtain the contribution to the total cross section from the i'th state,

$$\sigma_i(\omega) = \frac{k_f}{\omega}\int (P_{if})^2 d\Omega. \tag{5.9}$$

The solid angle integration is performed numerically using 14 quadrature points. The matrix elements P_{if} involve Fourier transformations of Gaussian functions and are calculated analytically. The measured photoemission spectra is a summation over all the contributing initial states,

$$\sigma_{tot}(E) = \frac{1}{\Delta\sqrt{\pi}}\sum_i \exp\left[-\left[\frac{E-\omega-\varepsilon_i}{\Delta}\right]^2\right]\sigma_i(\omega) \tag{5.10}$$

where Gaussian broadening has been used as in the plots of the electronic density of states.

Although XPS^{22} of pure cubic boron nitride thin films have been experimentally measured, there has been no photoemission spectra taken for substitutional defects in cubic boron nitride. The theoretical calculation of the photoemission spectra for substitutional dopants in cubic boron nitride has not been previously done. We have calculated the photoemission spectra for a range of incident photon energies ranging from 10 eV to 90 eV (ultraviolet). In Fig. 29, the photoemission spectra of the pure cubic boron nitride cluster is shown for incident photon energies of 60 eV, 65 eV, and 70 eV as a function of *E* from Eq. (5.10). In Fig. 30, the photoemission spectra is shown for the beryllium doped cluster for incident photon energies of 60 eV, 65 eV and 70 eV. Fig. 31 shows the photoemission spectrum for the silicon doped cluster for these same incident photon energies. For each of the three clusters, the spectra changes with respect to incident photon energy. Recall from Chapter IV that the highest occupied level in the pure cluster was at -17.01 eV. Thus, no peaks are evident until the value of *E* is below about -20 eV. The same basic peaks are observable at the different incident photon energies; however, the relative intensity of the peaks to each other can change substantially based on the incident photon energy. In addition, there is a general trend for the peaks to move to lower values of E with higher

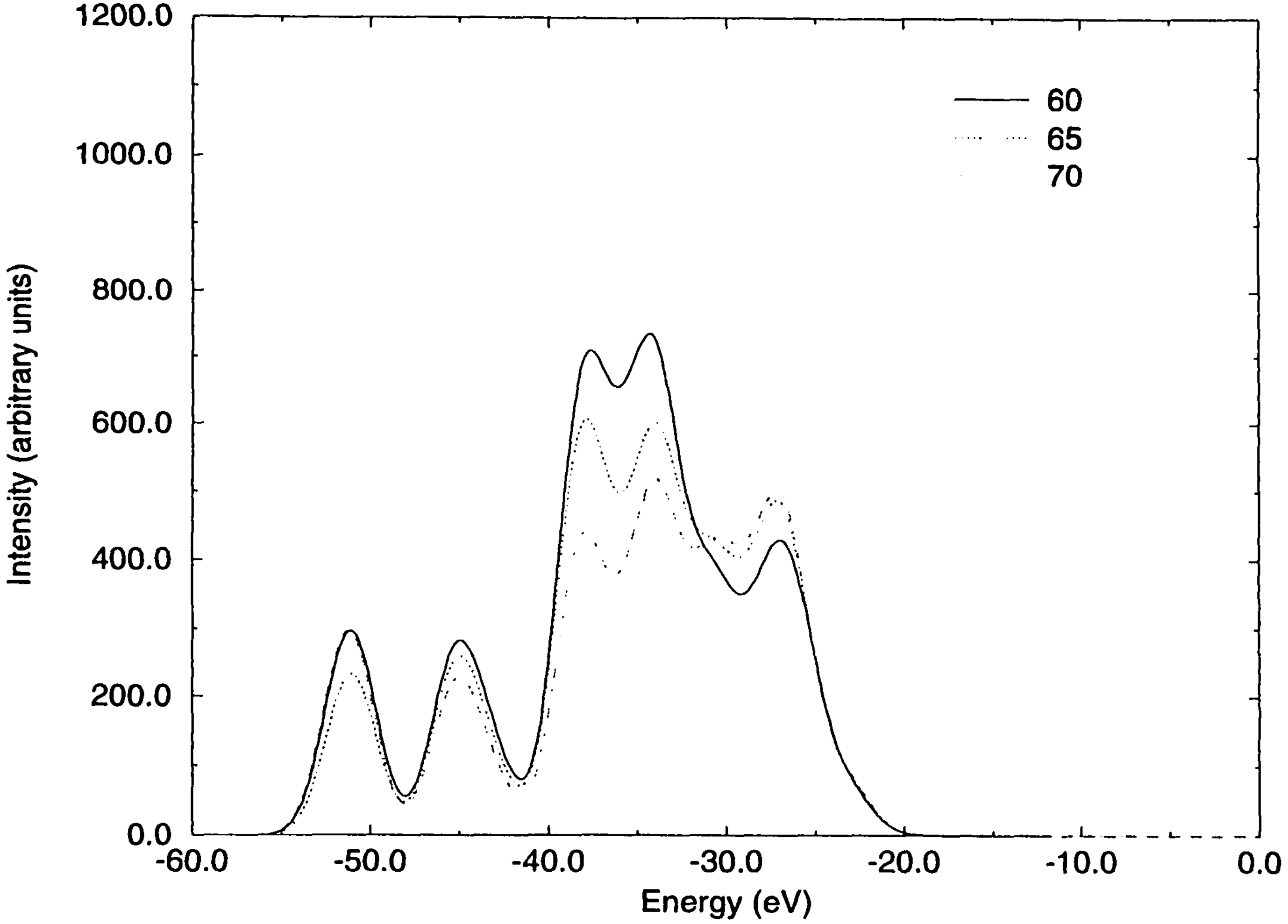

FIG. 29. The photoemission lineshapes for the $B_{13}N_{16}H_{36}$ cluster at selected values of incident photon energies.

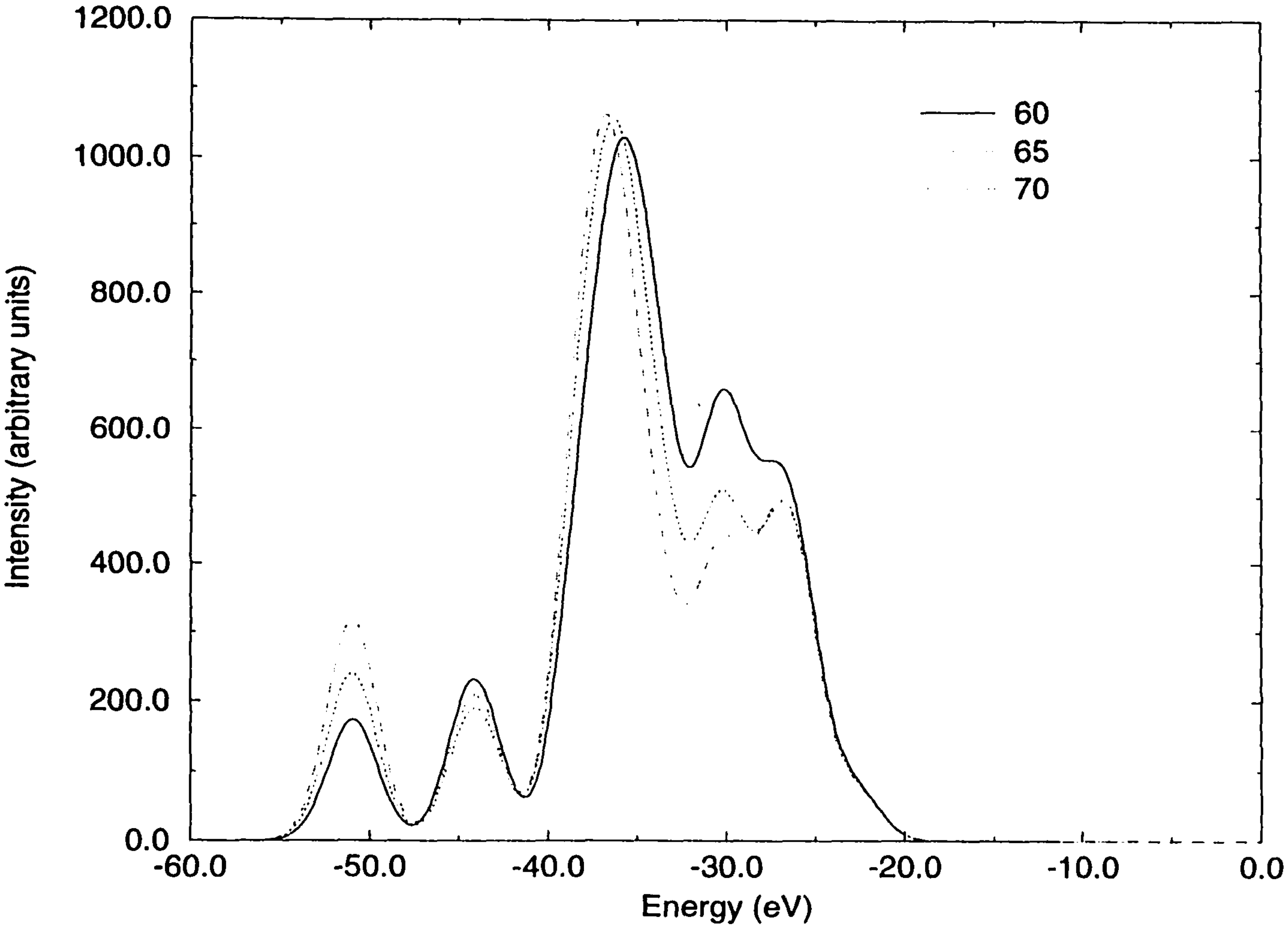

FIG. 30. The photoemission lineshapes for the $BeB_{12}N_{16}H_{36}$ cluster at selected values of incident photon energies.

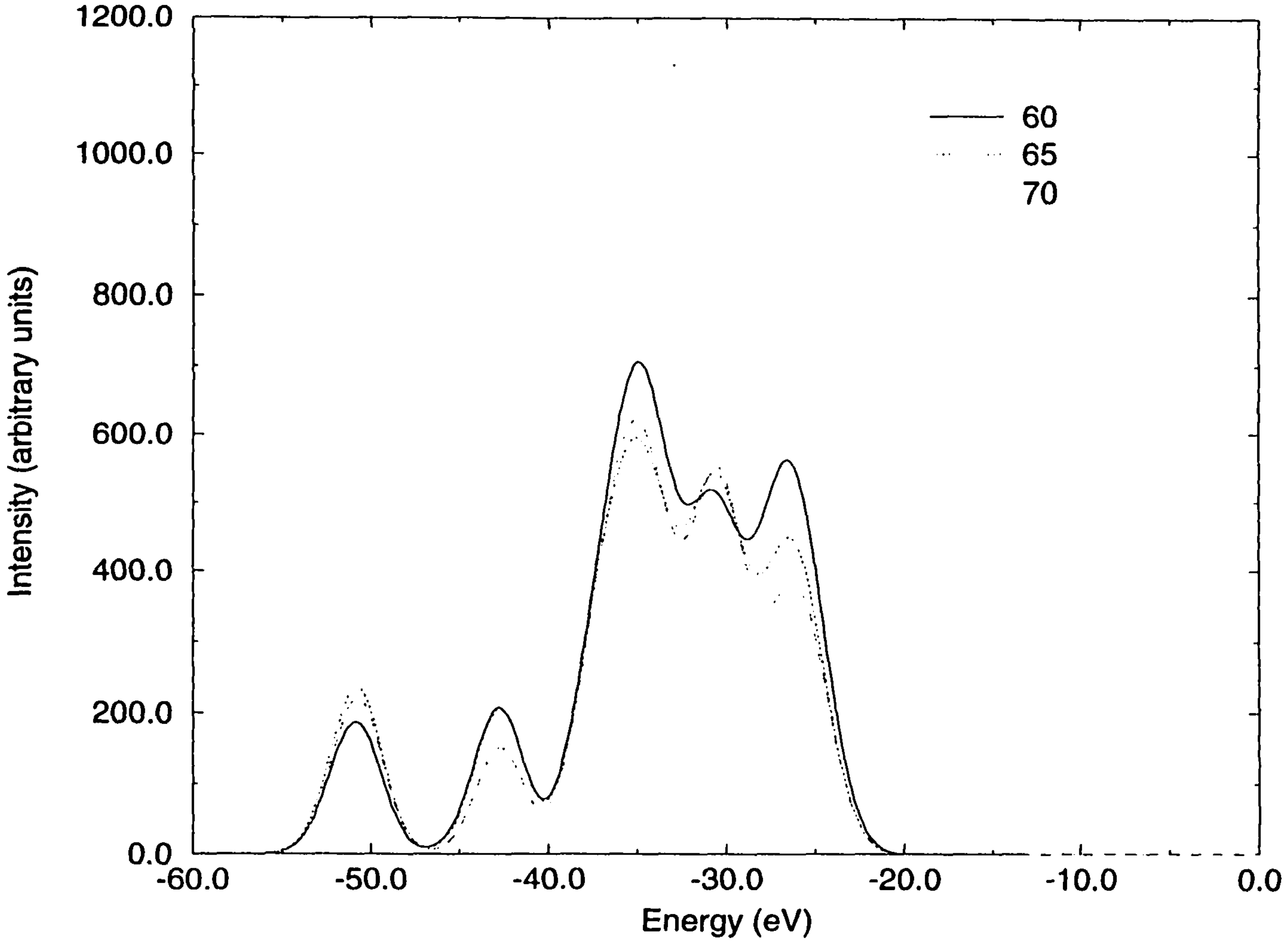

FIG. 31. The photoemission lineshapes for the $SiB_{12}N_{16}H_{36}$ cluster at selected values of incident photon energies.

photon incident energies. The photoemission spectra are shown for the pure and beryllium doped clusters in Fig. 32 for an incident photon energy of 60 eV. The photoemission spectra are shown for the pure and silicon doped clusters in Fig. 33 for an incident photon energy of 60 eV. The presence of the dopants makes a large change in the lineshape of the spectra at this energy. This seems to be particularly prominent in the region between -20 eV and -40 eV. This reflects the changes in the electronic structure in the band gap when the dopants are introduced. The dopant levels in the band-gap are creating photoelectron cross sections that differ from those of the valence band of the pure cubic boron nitride.

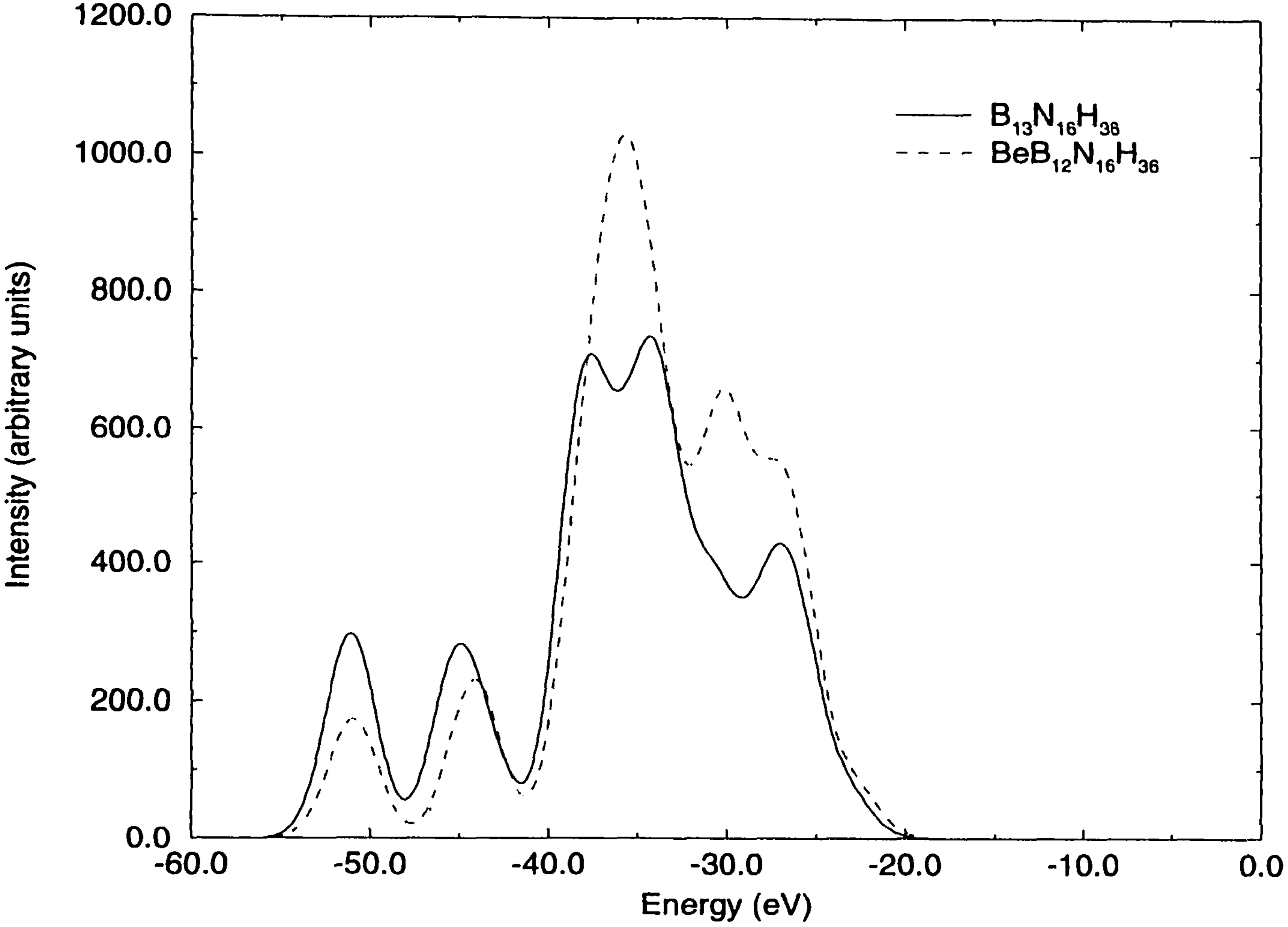

FIG. 32. The photoemission lineshapes for the pure and beryllium-doped clusters at an incident photon energy of 60 eV.

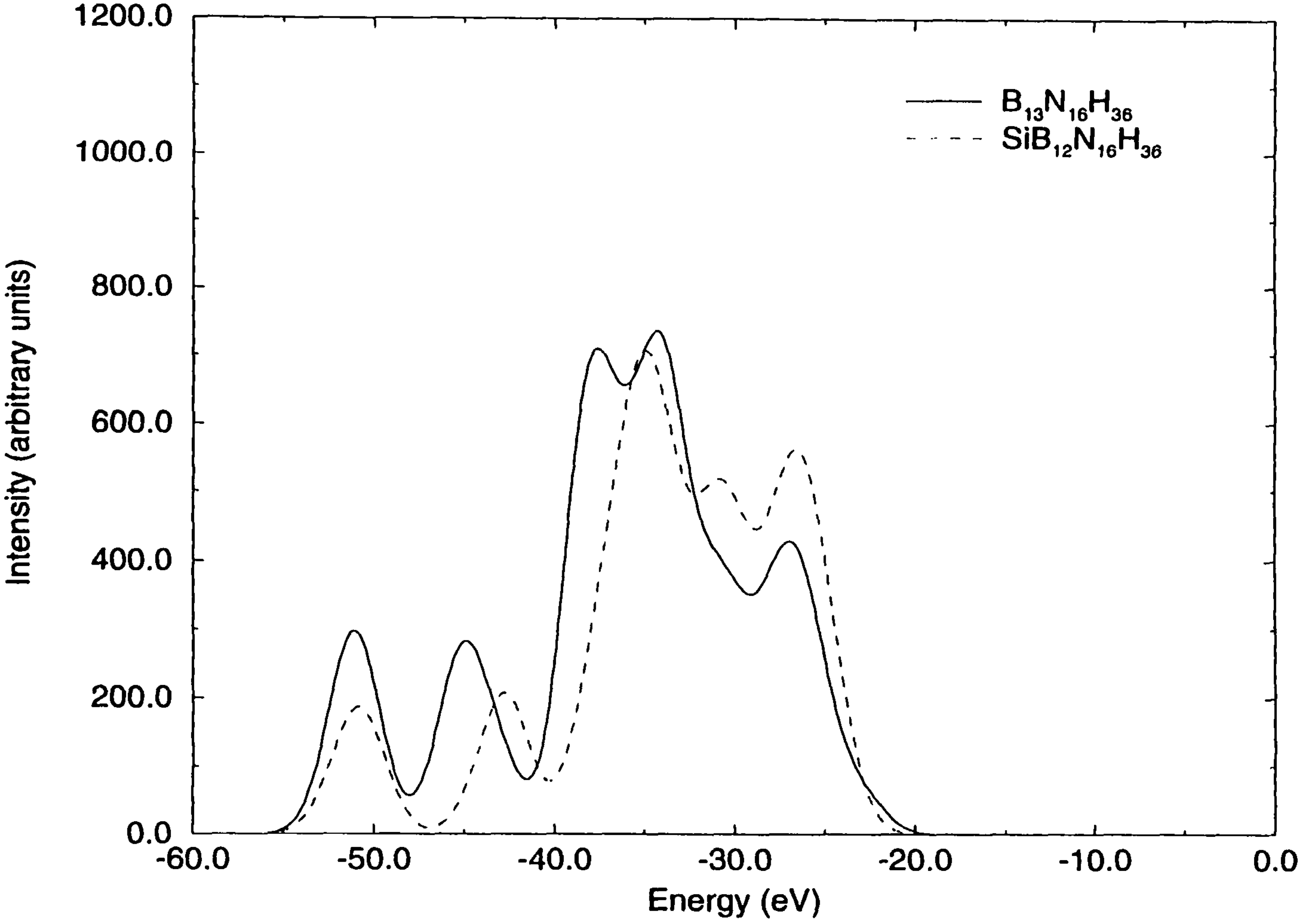

FIG. 33. The photoemission lineshapes for the pure and silicon-doped clusters at an incident photon energy of 60 eV.

CHAPTER VI

CONCLUSIONS

In this work, we have carried out a computational characterization of prospective n- and p-type dopants in cubic boron nitride. We have studied beryllium substitutional for boron as a p-type dopant and silicon substitutional for boron as a n-type dopant. We have calculated selected properties of the dopants with the locally available computational packages. Fermi contact terms, vibrational modes, oscillator strengths, and photoemission spectra were investigated. These properties were chosen based on their measurability by experimental techniques.

The electronic structures of pure cubic boron nitride, beryllium-doped cubic boron nitride, and silicon-doped cubic boron nitride were calculated with our LCAO cluster codes. As noted in Chapter II, the LCAO cluster codes allow full incorporation of the crystal field effects via an embedding potential and allow the determination of defect-induced lattice distortion within a given symmetry. A computationally efficient method for calculation of the embedding potential for the zincblende structure based on Hund's relations was discussed and compared to other methods in Chapter III. The applicability of using cluster codes to simulate the environment of the crystal was discussed, and two important points were made. First, the concern of how to tie-off dangling bonds on the cluster surface was satisfactorily resolved by saturating them with hydrogen atoms. Second, the issue of how many electrons should be assigned to a cluster was addressed. It was found that in order to recreate the bonding environment of the crystal, the boron and nitrogen atoms must be assigned six electrons. This method of electron filling was found to reproduce the sp^3 bonds present in the tetrahedral bonding environment of crystalline cubic boron nitride.

The importance of embedding clusters of cubic boron nitride was discussed in Chapter IV. It was found that the embedding potential places the cluster in an essentially uniform potential well. This causes a shift in the eigenvalues. Because the clusters were populated with quantities of electrons necessary to achieve the proper sp^3 bonding, embedding actually worsened the electronic structure. Therefore, the electronic structure was studied without embedding. We chose to study boron-centered clusters of 29 atoms based on their ability to reproduce the crystalline environment and on the fact that their size made them computationally feasible.

Our LCAO cluster calculations indicated that when beryllium is substituted for a boron, an acceptor level is created above the valence band. The level is a t_1 spin down state containing two electrons. When the nearest neighbor nitrogens were allowed to relax, they were found to move outward by 5.2% of the bond distance of the bulk geometry. At the relaxed geometry, the acceptor level is still a two-thirds full t_1 spin down level and resides at 0.236 eV above the fully occupied t_1 spin up level. This compares quite favorably with the estimated activation energy of 0.23 ±0.02 eV reported by Mishima *et al.*[23] for their *p*-type crystals. In Chapter V, calculated results of selected properties were presented for the $BeB_{12}N_{16}H_{36}$ cluster. Spin densities at the nuclei and the resultant Fermi contact terms were calculated for the first four shells with the LCAO cluster codes. A small decrease in the spin densities at the beryllium nuclei and nearest neighbor nitrogens was observed when the cluster was allowed to relax.

When silicon is substituted for boron, a donor level is created below the conduction band. The level is a t_1 spin up state containing one electron. When the nearest neighbor nitrogens were allowed to relax, they were found to move outward by 7.0% of the bond distance of the bulk geometry. At the relaxed geometry, the donor level is still a one-third full t_1 spin up level and resides at 0.116 eV below the unoccupied t_1 spin down level. This compares well with the estimated activation energy of 0.24 ±0.03 eV reported by Mishima *et al.*[23] for their *n*-type crystals. In addition, calculated results of selected properties were presented for the relaxed $SiB_{12}N_{16}H_{36}$ cluster. Spin densities at the nuclei and the resultant Fermi contact terms were calculated for the first four shells with the LCAO cluster codes. A decrease in the spin densities at the silicon nuclei and nearest neighbor nitrogens was observed when the cluster was allowed to relax. There was also an increase in the Fermi contact term at the silicon nuclei.

The MOPAC6 package was used in the calculation of the vibrational spectrum of the beryllium- and silicon-doped cubic boron nitride cluster. The spectrum calculated is quite different from that of the pure cubic boron nitride cluster and may offer some insight into the symmetry of these *p*- and *n*-type dopants once experimental data are available. The oscillator strengths of beryllium- and silicon-doped cubic boron nitride were calculated with the ICON-EDiT program, and the photoemission spectra were calculated using the eigenfunctions output from the ab-initio GAMESS package. It is hoped that these results will provide some insight for any future experimental measurements. The oscillator strengths, especially for the transition at 15584.9 cm^{-1} in the beryllium cluster, may be of particular import when determining dopant concentrations. The large difference in the photoemission spectra results for the silicon-doped cluster vs. the beryllium-doped cluster is particularly notable and should be an interesting item for experimental study.

Our identification of the highest occupied levels in both $BeB_{12}N_{16}H_{36}$ and $SiB_{12}N_{16}H_{36}$ as being partially-filled T_1 levels, suggests a possible Jahn-Teller distortion associated with the substitutional dopants. The resolution of what the lowest total-energy geometry is for a distortion to a geometry of lower symmetry presents a demanding problem for future study. The study of larger clusters with faster codes may ultimately be required to correctly predict low-symmetry relaxations in doped cubic boron nitride clusters.

In addition to the interesting question of defect-induced lowering of symmetry in the beryllium- and silicon-doped cubic boron nitride clusters, there are many other directions for future work. One possible direction is the study of other substitutional dopants and defects in cubic boron nitride. Vacancies, silicon and sulfur substitutional for nitrogen (as *p*- and *n*-type dopants, respectively), carbon substitutional for both boron and nitrogen, and antisite defects are some of the systems that present prospective problems. Another direction that will lead to more accurate calculation of most of the properties studied in this work is to be able to extract the eigenfunctions from the LCAO cluster codes. This would allow them to be used in the calculation of the oscillator strengths and the photemission spectra. It also would facilitate plotting of orbital densities. Currently the eigenfunctions are composed of symmetry-adapted linear combinations (SALC's)[74] of atomic orbitals. Thus, either the eigenfunctions must be extracted in a nonsymmetrized form or the codes for the oscillator strengths and photoemission spectra must be written so as to utilize symmetry. In the case of the photoemission spectra, simple analytic expressions for the transition matrix can be derived with the SALC's. Improvement in the quality of the eigenfunctions will then become more critical because of the sensitivity of calculated optical properties to eigenfunction accuracy. Nonlocal corrections to the local density approximation utilized in our LCAO cluster codes, such as the generalized gradient approximation,[75,76] may lead to improved eigenfunctions.

REFERENCES

[1]J. H. Edgar, J. Mater. Res. **7**, 235 (1992).

[2]J. P. Dismukes, M. W. Yim, J. J. Tietjen and R. E. Novak, RCA Rev. **31**, 680 (1970).

[3]G. Mandel, F. F. Morehead and P. R. Wagner, Phys. Rev. A **136**, 826 (1964).

[4]V. A. Gubanov, Z. W. Lu, B. M. Klein and C. Y. Fong, Phys. Rev. B 53, **1** (1996).

[5]R. Riedel, Adv. Mater. **6**, 549 (1994).

[6]P. Lin, C. Deshpandey, H. J. Doerr, R. F. Bunshah, K. L. Chorpa and V. Vankar, Thin Solid Films **153**, 487 (1987).

[7]B. Rother and C. Weissmantel, Phys. Status Solidi A **87**, K119 (1985).

[8]R. H. Wentorf, J. Chem. Phys. **26**, 956 (1957).

[9]N. E. Christensen, S. Satpathy and Z. Pawlowska, Phys. Rev. B **36**, 1032 (1987).

[10]H. Saitoh, T. Hirose, H. Matsui, Y. Hirotsu and Y. Ichinose, Surf. Coat. Technol. **39**, 265 (1989).

[11]T. Andoh, S. Nishiyama, H. Kirimura, T. Mikami, K. Ogata and F. Fujumoto, Nucl. Instrum. Methods B **56**, 276 (1991).

[12]D. J. Kester and R. Messier, J. Appl. Phys. **72**, 504 (1992).

[13]M. Murakawa and S. Watanabe, Surf. Coat. Technol. **43**, 128 (1990).

[14]A. Bath, O. Baehr, M. Barrada, B. Lepley, P. J. van der Put and J. Schoonman, Thin Solid Films **241**, 278 (1994).

[15]A. Chayahara, H. Yokoyama, T. Imura and Y. Osaka, Jpn. J. Appl. Phys. **26**, L1435 (1987).

[16]H. Saitoh and W. A. Yarbrough, Appl. Phys. Lett. **58**, 2482 (1991).

[17]G. L. Doll, J. A. Sell, C. A. Taylor II and R. Clarke, Phys. Rev. B **43**, 6816 (1991).

[18]M. Mieno and T. Yoshida, Jpn. J. Appl. Sci. **29**, L1175 (1990).

[19]A. L. Ballal, L. Slamanca Riba, G. L. Doll, C. A. Taylor II and R. Clarke, J. Mater. Res. **7**, 1618 (1992).

[20]O. Burat, D. Boucher, V. Stambouli and G. Gautherin, J. Appl. Phys. **68**, 2780 (1990).

[21]M. Lu, A. Bosetta, R. Sukach, A. Bensaoula, K. Walters, K. Eipers-Smith and A. Schultz, Appl. Phys. Lett. **64**, 1514 (1994).

[22]N. Tanabe and M. Iwaki, Nucl. Instrum. Methods **80**, 1349 (1993).

[23]O. Mishima, J. Tanaka, S. Yamaoka and O. Fukunaga, Science **238**, 181 (1987).

[24]R. H. Wentorf, J. Chem. Phys. **34**, 809 (1961).

[25]R. H. Wentorf, J. Chem. Phys. **36**, 1990 (1962).

[26]H. Bethe, Ann. Physik **3**, 133 (1929).

[27]T. A. Kaplan and S. D. Mahanti, *Electronic Properties of Solids Using Cluster Methods* (Plenum Press, NY, 1995).

[28]D. Tomanek and M. A. Schluter, Phys. Rev. Lett. **25**, 1055 (1986).

[29]G. G. De Leo, W. B. Fowler and G. D. Watkins, Phys. Rev. B **29**, 3193 (1984).

[30]F. P. Larkins, J. Phys. C: Solid State Phys. **4**, 3065 (1971).

[31]F. P. Larkins, J. Phys. C: Solid State Phys. **4**, 3077 (1971).

[32]A. Mainwood, F. P. Larkins and A. M. Stoneham, Solid State Electron. **21**, 1431 (1978).

[33]R. P. Messmer and G. D. Watkins, Phys. Rev. Lett. **25**, 656 (1970).

[34]E. G. Moore and C. M. Carlson, Phys. Rev. B **4**, 2063 (1971).

[35]A. Zur, T. C. McGill and W. A. Goddard, *Proc. 13th Int. Conf. Defects in Semiconductors* (Metall. Soc. AIME, Warrendale, PA, 1984), p. 253..

[36]K. A. Jackson, M. R. Pederson and J. G. Harrison, Phys. Rev. B **41**, 12641 (1990).

[37]R. Jones and S. Oberg, Phys. Rev. B **44**, 3407 (1991).

[38]K. W. Whitten, K. D. Gailey and R. E. Davis, *General Chemistry with Qualitative Analysis* (Saunders, NY, 1988).

[39]J. E. Simmons, C. C. Lin, D. F. Fouquet, E. E. Lafon and R. C. Chaney, J. Phys. C: Solid State Phys. **8**, 1549 (1975).

[40]M. R. Pederson and K. A. Jackson, Phys. Rev. B **41**, 7453 (1990).

[41]F. W. Averill and G. S. Painter, Phys. Rev. B **34**, 2088 (1986).

[42]K. A. Jackson and M. R. Pederson, Phys. Rev. B **42**, 3276 (1990).

[43]O Axelsson, *Iterative Solution Methods* (Cambridge University Press, NY, 1994), p. 449.

[44]M. W. Schmidt, K. K. Baldridge, J. A. Boatz, S. T. Elbert, M. S. Gordon, J. H. Jensen, S. Koseki, N. Matsunaga, K. A. Nguyen, S. J. Su, T. L. Windus, M. Dupuis and J. A. Montgomery, J. Comput. Chem. **14**, 1347 (1993).

[45]M. J. S. Dewar, G. P. Ford, M. McKee, H. S. Rzepa and Y. Yamaguchi, J. Mol. Struct. **43**, 135 (1978).

[46]R. E. Watson, Phys. Rev. **111**, 1108 (1958).

[47]A. Fazzio, J. R. Leite, A. C. Pavao and M. L. De Siqueira, J. Phys. C: Solid State Phys. **11**, L175 (1978).

[48]C. Kittel, *Introduction to Solid State Physics* (John Wiley and Sons, NY, 1953), p. 66.

[49]E. Madelung, Physik. Z. **19**, 524 (1918).

[50]M. P. Tosi, Solid State Phys. **16**, 1 (1964).

[51]H. M. Evjen, Phys. Rev. **39**, 675 (1932).

[52]F. C. Frank, Phil. Mag. **41**, 1287 (1950).

[53]S. C. Ke, D. C. Patton, J. G. Harrison and H. T. Tohver, J. Phys. Condens. Matter **7**, 9625 (1995).

[54]M. Born and K. Huang, *Dynamical Theory of Crystal Lattices* (Oxford University Press, London, 1954).

[55]G. Leibfried, *Handbuch der Physik* (Springer, Berlin, 1995), p. 132.

[56]P. P. Ewald, Ann. Physik **64**, 253 (1921).

[57]J. D. Jackson, *Classical Electrodynamics* (John Wiley & Sons, NY, 1962).

[58]M. von Laue, *Materiewellen und ihre Interferenzen* (Leipzig, 1948), p. 255.

[59]L. J. Comrie, *Mathematical Tables* (A. Van Nostrand, Princeton, 1949).

[60] F. W. De Wette and B. R. A. Nijboer, Physica **24**, 1105 (1958).

[61] B. R. A. Nijboer and F. W. De Wette, Physica **23**, 309 (1957).

[62] B. R. A. Nijboer and F. W. De Wette, Physica **24**, 422 (1958).

[63] F. Hund, Z. Physik **94**, 11 (1935).

[64] A. Zunger and A. J. Freeman, Phys. Rev. B **17**, 2030 (1978).

[65] R. Dovesi, C. Pisani, C. Roetti and P. Dellarole, Phys. Rev. B **24**, 4170 (1981).

[66] R. M. Wentzcovich, K. J. Chang and M. L. Cohen, Phys. Rev. B **34**, 1071 (1986).

[67] H. A. Jahn and E. Teller, Proc. Roy. Soc. A **161**, 220 (1937).

[68] M. Fanciulli and T. D. Moustakas, Physica B **185**, 228 (1993).

[69] R. M. Chrenko, Solid State Commun. **14**, 511 (1974).

[70] P. J. Gielisse, S. S. Mitra, J. N. Plendl, R. D. Griffis, L. C. Mansur, R. Marshall and E. A. Pascoe, Phys. Rev. **155**, 1039 (1967).

[71] S. Fahy, Phys. Rev. B **51**, 12873 (1995).

[72] I. N. Levine, *Quantum Chemistry* (Prentice Hall, Englewood Cliffs, NJ, 1991), p. 252.

[73] H. A. Bethe and R. Jackiw, *Intermediate Quantum Mechanics* (Benjamin/ Cummings, NY, 1986), p.218.

[74] F. A. Cotton, *Chemical Applications of Group Theory* (John Wiley & Sons, NY, 1990).

[75] R. M. Dreizler and E. K. U. Gross, *Density Functional Theory* (Springer-Verlag, NY, 1990).

[76] J. P. Perdew, J. A. Chevary, S. H. Vosko, K. A. Jackson, M. R. Pederson, D. J. Singh and C. Fiolhais, Phys. Rev. B **46**, 6671 (1992).

[77] P. Hohenberg and W. Kohn, Phys. Rev. B **6**, 13864 (1964).

[78] R. G. Parr and W. Yang, *Density Functional Theory of Atoms and Molecules* (Oxford University Press, NY, 1989).

[79] W. Kohn and L. J. Sham, Phys. Rev. A **140**, 1133 (1965).

[80] D. M. Ceperley and B. L. Alder, Phys. Rev. Lett. **45**, 566 (1980).

[81] S. H. Vosko, L. Wilk and M. Nusair, Can. J. Phys. **58**, 1200 (1980).

[82] J. P. Perdew and A. Zunger, Phys. Rev. B **23**, 5048 (1981).

[83] M. Gell-Mann and K. A. Brueckner, Phys. Rev. **106**, 364 (1957).

[84] L. Hedin, Phys. Rev. **139**, A 796 (1965).

[85] S. Misawa, Phys. Rev. A **140**, 1645 (1965).

[86] U. von Barth and L. Hedin, J. Phys. C **5**, 1629 (1972).

[87] A. Geist, A. Beguelin, J. Dongarra, W. Jiang, R. Mancheck and V. Sunderam, *PVM: Parallel Virtual Machine* (MIT Press, NY, 1993).

APPENDIX A

DENSITY FUNCTIONAL THEORY

The primary theory, which is the foundation of our calculations, is density functional theory.[75,77,78] It allows one to replace the complicated N-electron wave function $\Psi(x_1, x_2, \ldots, x_N)$ and the associated Schrodinger equation by the much simpler electron density $\rho(\mathbf{r})$ and its associated calculational scheme.

Density functional theory is based on two theorems :

1) The external potential $\upsilon(\mathbf{r})$ *is determined, within a trivial additive constant, by the electron density* $\rho(\mathbf{r})$.

2) For a trial density $\tilde{\rho}(\mathbf{r})$, *such that* $\tilde{\rho}(\mathbf{r}) \geq 0$ *and* $\int \tilde{\rho}(\mathbf{r})\,d\mathbf{r} = N$, $E_0 \leq E[\tilde{\rho}]$ *where* E_0 *is the ground state energy.*

Since ρ determines the number of electrons, it also determines the ground state, Ψ_0, and all other electronic properties of the system including the kinetic energy, the potential energy, and the total energy. Hence,

$$E[\rho] = T[\rho] + V_{ne}[\rho] + V_{ee}[\rho] = \int \rho(\mathbf{r})\,\upsilon(\mathbf{r})\,d\mathbf{r} + F_{HK}[\rho] \tag{A.1}$$

where $F_{HK}[\rho] = T[\rho] + V_{ee}[\rho]$ and $V_{ee}[\rho] = U_c[\rho] + E_{xc}[\rho]$.

$$U_c[\rho] = \frac{1}{2}\iint \frac{\rho(\mathbf{r}_1)\,\rho(\mathbf{r}_2)}{r_{12}}\,d\mathbf{r}_1 d\mathbf{r}_2 \tag{A.2}$$

is the classic Coulomb energy. The nonclassical term $E_{xc}[\rho]$ is the major part of the exchange-correlation energy.

The variational principle[78]

$$\delta\{E[\rho] - \mu[\int \rho(\mathbf{r})\,d\mathbf{r} - N]\} = 0 \tag{A.3}$$

gives the Euler-Lagrange equation where the chemical potential

$$\mu = \frac{\delta E[\rho]}{\delta \rho(\mathbf{r})} = \upsilon(\mathbf{r}) + \frac{\delta F_{HK}[\rho]}{\delta \rho(\mathbf{r})}. \tag{A.4}$$

Note that if $F_{HK}[\rho]$ were exactly known, then the variational principle above would be an exact equation for the ground state electron density. The unfortunate fact is that exact form of the functional $F_{HK}[\rho]$ is not known.

The ground state density can be determined by the Kohn-Sham method.[79] The kinetic energy of a noninteracting electron system that exists with the same $\rho(\mathbf{r})$ as the interacting system is written as

$$T_0[\rho] = \sum_{i=1}^{N} \langle \psi_i(r) | \left(-\frac{1}{2}\nabla^2\right) | \psi_i(r) \rangle \tag{A.5}$$

where the $\psi_i(\mathbf{r})$ are the Kohn-Sham orbitals, such that

$$F_{HK}[\rho] = T_0[\rho] + U_c[\rho] + E_{xc}[\rho] . \tag{A.6}$$

The exchange-correlation energy in Eq. (A.6) is not the same as that in Eq. (A.2) because it now contains the difference between the kinetic energies of an interacting and a noninteracting electron system. Thus, the exchange-correlation energy functional can be expressed as

$$E_{xc}[\rho] = T[\rho] - T_0[\rho] + V_{ee}[\rho] - U_c[\rho] . \tag{A.7}$$

The Euler equation then becomes

$$\mu = \frac{\delta T_0}{\delta \rho} + \frac{\delta U_c}{\delta \rho} + \frac{\delta E_{xc}}{\delta \rho} + \upsilon(\mathbf{r}) = \frac{\delta T_0[\rho]}{\delta \rho(\mathbf{r})} + V_{eff}(\mathbf{r}) \tag{A.8}$$

where

$$V_{eff}(\mathbf{r}) = \upsilon(\mathbf{r}) + \frac{\delta U_c}{\delta \rho} + \frac{\delta E_{xc}}{\delta \rho}$$

$$= \upsilon(\mathbf{r}) + \frac{\delta U_c}{\delta \rho} + \upsilon_{xc}(r) \tag{A.9}$$

with $\upsilon_{xc}(r) = \frac{\delta E_{xc}}{\delta \rho}$ being the exchange-correlation potential. The density $\rho(\mathbf{r})$ can be obtained after solving the Kohn-Sham equations:

$$\left[-\frac{1}{2}\nabla^2 + V_{eff}(\mathbf{r})\right]\psi_i(\mathbf{r}) = \varepsilon_i \psi_i(\mathbf{r}) \tag{A.10}$$

with

$$\rho(r) = \sum_{i=1}^{N} |\psi_i(r)|^2 . \tag{A.11}$$

Equations (A.9), (A.10), and (A.11) are the one-electron Kohn-Sham equations and are solved self-consistently to get the density.

The Kohn-Sham equations still leave the exact form of the exchange-correlation functional unknown. One of the most successful forms is derived in the local density approximation (LDA). In the LDA,

$$E_{xc}^{LDA}[\rho] = \int \rho(\mathbf{r})\,\varepsilon_{xc}[\rho]\,d\mathbf{r} \tag{A.12}$$

where ε_{xc} is the exchange and correlation energy per particle of a uniform electron gas. The corresponding form of the exchange-correlation potential is

$$\upsilon_{xc}^{LDA}(r) = \frac{\delta E_{xc}^{LDA}}{\delta\rho} = \varepsilon_{xc}[\rho(r)] + \rho(r)\frac{\delta\varepsilon_{xc}[\rho]}{\delta\rho}. \tag{A.13}$$

The functional $\varepsilon_{xc}[\rho]$ can be separated into the exchange and correlation contributions

$$\varepsilon_{xc}[\rho] = \varepsilon_x[\rho] + \varepsilon_c[\rho]. \tag{A.14}$$

The exchange energy for the homogeneous electron gas is already known and is given by the Dirac exchange-energy functional[78]

$$\varepsilon_x[\rho] = -C_x[\rho(r)]^{\frac{1}{3}} \tag{A.15}$$

where $C_x = \frac{3}{4}\left(\frac{3}{\pi}\right)^{\frac{1}{3}}$.

To allow for more accurate calculation, the local spin density approximation (LSD) is used:

$$E_{xc}^{LSD}[\rho] = \int \varepsilon_{xc}[\rho_\alpha, \rho_\beta]\,\rho(\mathbf{r})\,d\mathbf{r} \tag{A.16}$$

where α and β indicate spin up and spin down respectively and

$$\rho(\mathbf{r}) = \rho_\alpha(\mathbf{r}) + \rho_\beta(\mathbf{r}) \tag{A.17}$$

$$\rho_\sigma(r) = \sum_{i=1}^{occupied} |\psi_{i\sigma}(r)|^2 \qquad \sigma = \alpha, \beta \tag{A.18}$$

and the LSDA Kohn-Sham SCF one electron equation becomes:

$$\hat{H}_\sigma\psi_{i\sigma}(\mathbf{r}) = \varepsilon_{i\sigma}\psi_{i\sigma}(\mathbf{r}) \tag{A.19}$$

$$\hat{H}_\sigma = -\frac{1}{2}\nabla^2 + \upsilon(\mathbf{r}) + \frac{\delta U_c[\rho]}{\delta\rho(\mathbf{r})} + \frac{\delta E_{xc}^{LSD}[\rho]}{\delta\rho(\mathbf{r})}. \tag{A.20}$$

Again, the exchange-correlation energy may be written in terms of its contributions from the exchange and correlation parts

$$E_{xc}^{LSD}[\rho_\alpha, \rho_\beta] = E_x^{LSD}[\rho_\alpha, \rho_\beta] + E_c^{LSD}[\rho_\alpha, \rho_\beta] . \qquad \text{(A.21)}$$

The LSD exchange energy functional becomes

$$E_x^{LSD}[\rho_\alpha, \rho_\beta] = -\frac{3}{4}\left(\frac{6}{\pi}\right)^{1/3}\int\left[(\rho_\alpha)^{\frac{4}{3}} + (\rho_\beta)^{\frac{4}{3}}\right]dr . \qquad \text{(A.22)}$$

The local density form of the correlation energy functional can be written as:

$$E_c^{LSD} = \int \varepsilon_c[\rho_\alpha, \rho_\beta]\,\rho(r)\,dr \qquad \text{(A.23)}$$

where ε_c denotes the correlation energy per electron for an electron gas with uniform spin densities. This system has been simulated by Ceperley and Alder[80] and parametrized by Vosko *et al.*[81] and Perdew and Zunger.[82]

In Perdew and Zunger's parametrization, the correlation energy ε_c and the corresponding potential υ_c can be classified into the high and the low limits of the density after using the following derivatives at the point r_s=1,

$$\upsilon_c(\rho, \zeta = 0, 1) = \left\{1 - \frac{r_s}{3}\frac{d}{dr_s}\right\}\varepsilon_c(\rho, \zeta = 0, 1) \qquad \text{(A.24)}$$

where the Wigner-Seitz radius is $r_s = (3/4\pi)^{1/3}\rho^{-1/3}$ in atomic units. For the low density $r_s \geq 1$, the correlation energy and the corresponding potential are written as the following:

$$\varepsilon_c(\zeta) = \frac{\gamma(\zeta)}{\left(1 + \beta_1(\zeta)\sqrt{r_s} + \beta_2(\zeta)\,r_s\right)} \qquad \text{(A.25)}$$

$$\upsilon_c(\zeta) = \left(1 + \frac{7}{6}\beta_1(\zeta)\sqrt{r_s} + \frac{4}{3}\beta_2(\zeta)\,r_s\right)\frac{\varepsilon_c^2(\zeta)}{\gamma(\zeta)} \qquad \text{(A.26)}$$

where $\beta_1(\zeta)$, $\beta_2(\zeta)$, and $\gamma(\zeta)$ are fit-parameters, the index ζ is for the polarized $(\zeta = 1)$ or the unpolarized $(\zeta = 0)$ case. The parameters used to represent the Ceperley and Alder results are $\beta_1(0)$=1.0529, $\beta_1(1)$=1.3981, $\beta_2(0)$=0.3334, $\beta_2(1)$=0.2611, $\gamma(0)$=-0.1423, and $\gamma(1)$=-0.0843.

For high density $(0 \leq r_s \leq 1)$, the leading behavior of the high density expansion is tied smoothly to the low density form with the following expression:

$$\varepsilon_c(\zeta) = A(\zeta)\,ln r_s + B(\zeta) + C(\zeta)\,r_s ln r_s + D(\zeta)\,r_s \qquad \text{(A.27)}$$

$$\upsilon_c = A(\zeta)\,ln r_s + \{B(\zeta) - \tfrac{1}{3}A(\zeta)\} + \tfrac{2}{3}C(\zeta)\,r_s ln r_s + \tfrac{1}{3}\{2D(\zeta) - C(\zeta)\}\,r_s. \quad \text{(A.28)}$$

Perdew and Zunger parameterized this form by taking the values $A(0) = 0.0311$ and $B(0) = -0.048$ from the calculation of Gell-Mann and Brueckner,[83] fixing the values $A(1) = 0.01555$ and $B(1) = -0.0269$ from the random phase scaling relation by Hedin[84] and Misawa[85] and determining the values $C(0)=0.0020$, $C(1)=0.0007$, $D(0)=-0.0116$, $D(1)=-0.0048$ by matching the low density and high density forms and their derivatives at $r_s = 1$.

For intermediate values of ζ, the von Barth-Hedin interpolation[86] can be adopted. For the spin densities $\rho\uparrow(\boldsymbol{r})$ and $\rho\downarrow(\boldsymbol{r})$, the density is denoted as $\rho(\boldsymbol{r}) = \rho\uparrow(\boldsymbol{r}) + \rho\downarrow(\boldsymbol{r})$ and the polarization factor can be written

$$\zeta(\boldsymbol{r}) = \frac{1}{\rho(\boldsymbol{r})}\,[\rho\uparrow(\boldsymbol{r}) - \rho\downarrow(\boldsymbol{r})]. \quad \text{(A.29)}$$

The interpolation between the unpolarized paramagnetic ($\zeta = 0$) and the fully polarized ferromagnetic ($\zeta = \pm 1$) limits can be written by

$$\varepsilon_i(\zeta) = \varepsilon_i(\zeta = 0) + [\varepsilon_i(\zeta = 1) - \varepsilon_i(\zeta = 0)]\,f(\zeta(\boldsymbol{r})) \quad \text{(A.30)}$$

for the exchange ($i = x$) and correlation ($i = c$) contributions to the energy per particle. The interpolation function

$$f(\zeta(\boldsymbol{r})) = \frac{(1+\zeta(\boldsymbol{r}))^{4/3} + (1-\zeta(\boldsymbol{r}))^{4/3} - 2}{2\left(2^{1/3} - 1\right)} \quad \text{(A.31)}$$

is chosen to reproduce the ζ-dependence of the exchange and the correlation energies. In the para- and ferro-magnetic limits, the exchange term has the form

$$\varepsilon_x(\zeta = 0) = -\frac{3}{4}\left(\frac{3\rho}{\pi}\right)^{1/3} = -\frac{3}{4}\left(\frac{9\pi}{4}\right)^{1/3} r_s^{-1} \quad \text{(A.32)}$$

$$\varepsilon_x(\zeta = 1) = 2^{1/3}\varepsilon_x(\zeta = 0) \quad \text{(A.33)}$$

and from the random phase scaling relation

$$\varepsilon_c(r_s, \zeta = 1) = \frac{1}{2}\varepsilon_c\left(r_s 2^{-4/3}, \zeta = 0\right). \quad \text{(A.34)}$$

APPENDIX B

PARALLELIZATION TECHNIQUES

In the calculation of the electronic structure of an embedded cluster, there are three computationally costly steps that the LCAO cluster codes perform. The first is the calculation of the embedding potential. The second is the calculation of the Coulomb potential via Poisson's equation. The third is the calculation of the forces on each atom. All three of these steps involve some calculation of a value at points in the numerical integration mesh described by Pederson and Jackson.[40] It is the calculation of this value that is computationally costly. Even more important is that the calculations at different mesh points are completely independent of one another. So when doing one of the steps detailed above, each calculation at a mesh point could run separately from one another.

With the advent of massively parallel computers, parallelization of codes has become both feasible and necessary. The computational steps discussed above are all good candidates for parallelization by the master/slave model. In the master/slave model, a master process is begun on one node (CPU) of a computer and a large number of slave processes are started on other nodes. Each process in the master/slave model is running separately on its own node. The master process then sends a unique set of data to each slave process. The slaves receive their unique data set and begin to process it independently of the other slaves. After distributing all the data, the master process may continue working or it may wait for the processed answers to return from the slaves. The slaves compute the required answers for their unique data set and then send the data back to the master process. Load balancing can be provided by the way in which the data set is divided and distributed by the master process. Given n slaves and m data points, the master can then send m/n data points to each slave. However, if one of the slaves is slower than the others, the master will have to wait for this slowest slave to finish before continuing. A more effective use of the parallel machine would be for the master to break the data up into smaller quantities than *m/n*. Then the master can send each slave this smaller number of data points. The first slave to return an answer to the master would then receive another number of data points. This process would continue until all the data set was distributed and all the answers are returned.

We have implemented the master/slave model with the use of the Parallel Virtual Machine (PVM).[87] PVM is basically a combination of a daemon program and message passing libraries to allow Fortran, C, and C++ programs to interact with the daemon. Through PVM, processes on separate nodes are able to communicate with one another. PVM nodes may be any combination of CPU's on a parallel supercomputer, a CPU on a serial supercomputer, workstations, and even PC's. Below is an example of the Fortran code used in a master process with PVM:

```
    program master1
    include '../include/fpvm3.h'
c -----------------------------------------------------
c Example fortran program illustrating the use of PVM 3
c -----------------------------------------------------
    integer i, info, nproc, nhost, msgtype
    integer mytid, iptid, dtid, tids(0:32)
    integer who, speed
    double precision result(32), data(100)
    character*18 nodename, host
    character*8 arch

c ----------- Starting up all the tasks --------------------------

c    Enroll this program in PVM
    call pvmfmytid( mytid )

c    Set number of slaves to spawn.
c    Can't do standard input if master started with spawn so
c    just set nproc = number of hosts in this case. Else ask for nproc.

    call pvmfparent( iptid )
    if( iptid .gt. 1 ) then
      call pvmfconfig( nhost, narch, dtid, host, arch, speed, info )
      nproc = nhost
      if( nproc .gt. 32 ) nproc = 32
```

```
      else
        print *,'How many slave programs (1-32)?'
        read *, nproc
      endif
c
c     Initiate nproc instances of slave1 program
c     If arch is set to '*' then ANY configured machine is acceptable
      nodename = 'fslave1'
      arch = '*'
      call pvmfspawn( nodename, PVMDEFAULT, arch, nproc, tids, numt )

c     Print out task IDs of spawned tasks and check for problems
      do 100 i=0, nproc-1
        print *,'tid',i,tids(i)
100   continue
      if( numt .lt. nproc ) then
        print *, 'trouble spawning ',nodename
        print *, ' Check tids for error code'
        call shutdown( numt, tids )
      endif

c ------- Begin user program --------

      n = 10
c     Initiate data array
      do 20 i=1,n
        data(i) = 1
 20   continue

c     broadcast data to all node programs
      call pvmfinitsend( PVMDEFAULT, info )
      call pvmfpack( INTEGER4, nproc, 1, 1, info )
      call pvmfpack( INTEGER4, tids, nproc, 1, info )
      call pvmfpack( INTEGER4, n, 1, 1, info )
      call pvmfpack( REAL8,    data, n, 1, info )
      msgtype  = 1
      call pvmfmcast( nproc, tids, msgtype, info )

c     wait for results from nodes
      msgtype  = 2
      do 30 i=1,nproc
        call pvmfrecv( -1, msgtype, info )
        call pvmfunpack( INTEGER4, who, 1, 1, info )
        call pvmfunpack( REAL8, result(who+1), 1, 1, info )
        print *, 'I got',result(who+1), '  from', who
30    continue

c --------- End user program --------

c     program finished leave PVM before exiting
```

```
      call pvmfexit(info)
      stop
      end

      subroutine shutdown( nproc, tids )
      integer nproc, tids(*)
c
c     Kill all tasks I spawned and then myself
c
      do 10 i=0, nproc
         call pvmfkill( tids(i), info )
   10 continue
      call pvmfexit( info )
      return
      end
```

The Fortran code for the accompanying slave process follows:

```
      program slave1
      include '../include/fpvm3.h'
c ---------------------------------------------------
c Example fortran program illustrating use of PVM 3
c ---------------------------------------------------
      integer  info, mytid, mtid, msgtype, me
      integer  tids(0:32)
      double precision result, data(100)
      double precision work

c  Enroll this program in PVM
      call pvmfmytid( mytid )
c  Get the master's task id
      call pvmfparent( mtid )

c ------- Begin user program --------

c     Receive data from host
      msgtype  = 1
      call pvmfrecv( mtid, msgtype, info )
      call pvmfunpack( INTEGER4, nproc, 1, 1, info )
      call pvmfunpack( INTEGER4, tids, nproc, 1, info )
      call pvmfunpack( INTEGER4, n, 1, 1, info )
      call pvmfunpack( REAL8,    data, n, 1, info )

c     Determine which slave I am (0 -- nproc-1)
      do 5 i=0, nproc
         if( tids(i) .eq. mytid ) me = i
    5 continue

c     Do calculations with data
      result = work( me, n, data, tids, nproc )
```

```
c    Send result to host
     call pvmfinitsend( PVMDEFAULT, info )
     call pvmfpack( INTEGER4, me, 1, 1, info )
     call pvmfpack( REAL8,    result, 1, 1, info )
     msgtype  = 2
     call pvmfsend( mtid, msgtype, info )

c --------- End user program --------

c    Program finished. Leave PVM before exiting
     call pvmfexit(info)
     stop
     end

     double precision function work( me, n, data, tids, nproc )
     include '../include/fpvm3.h'
c    -----------------------------------
c    Just a simple routine for illustration
c    -----------------------------------
     double precision data(*), sum, psum
     integer i, n, me, inum
     integer tids(0:*)

     sum = 0.0
     do 10 i=1,n
       sum = sum + me * data(i)
10   continue
c    ------------------------------------
c    Pass partial result to neighboring node
c    to illustrate node-to-node communication
c    ------------------------------------
     call pvmfinitsend( PVMDEFAULT, info )
     call pvmfpack( REAL8, sum, 1, 1, info)
     inum = me+1
     if( inum .eq. nproc ) inum = 0
     call pvmfsend( tids(inum), 77, info )
     call pvmfrecv(  -1, 77, info )
     call pvmfunpack( REAL8, psum, 1, 1, info)

     work = sum + psum
     return
     end
```

In our codes we change the master1 program and slave1 programs given above to do the types of calculations we need. This involves altering the "**user program**" sections in the master1 and slave1 codes.

As an example of how these parallelization techniques are used in our LCAO cluster codes, consider the calculation of the embedding potential discussed in Chapter III. Given a mesh of 10,000 points, we need to evaluate $\varphi_{ZnS}(x, y, z)$, Eq. (3.22), for each point x, y, z. Since the value of $\varphi_{ZnS}(x, y, z)$ at each point is completely independent of the value at all other points, we can easily parallelize its calculation. Suppose our parallel machine has 100 nodes available, which are of equal power. If we start up a slave process on each node, then we send slave1 mesh points 1-100, slave2 mesh points 101-200, etc. Each slave could then evaluate $\varphi_{ZnS}(x, y, z)$ for the 100 mesh points it was assigned and then send the values back to the master. Perfect parallel performance would give a speed up of 100 times that of serial performance in the computation of $\varphi_{ZnS}(x, y, z)$ for all the mesh points. In reality, the parallel performance is always below perfection because of the time required to send and receive data.

In our LCAO cluster codes similar techniques are applied to the calculation of the Coulomb energy, Eq. (A.2), and the Hellman-Feynman-Pulay forces. These parallelization techniques have played an important role in the study of cubic boron nitride in that they have decreased the time required to perform calculations (making the calculation of larger clusters feasible) and they have allowed us access to state-of-the-art parallel supercomputers.

GRADUATE SCHOOL
UNIVERSITY OF ALABAMA AT BIRMINGHAM
DISSERTATION APPROVAL FORM

Name of Candidate David Clay Patton

Major Subject Physics

Title of Dissertation Computational Characterization of Prospective n- and p-type Dopants in Cubic Boron Nitride

Dissertation Committee:

, Chairman

Kumar Wahi

Tracy Hamilton

Director of Graduate Program

Dean, UAB Graduate School

Date 7/12/96